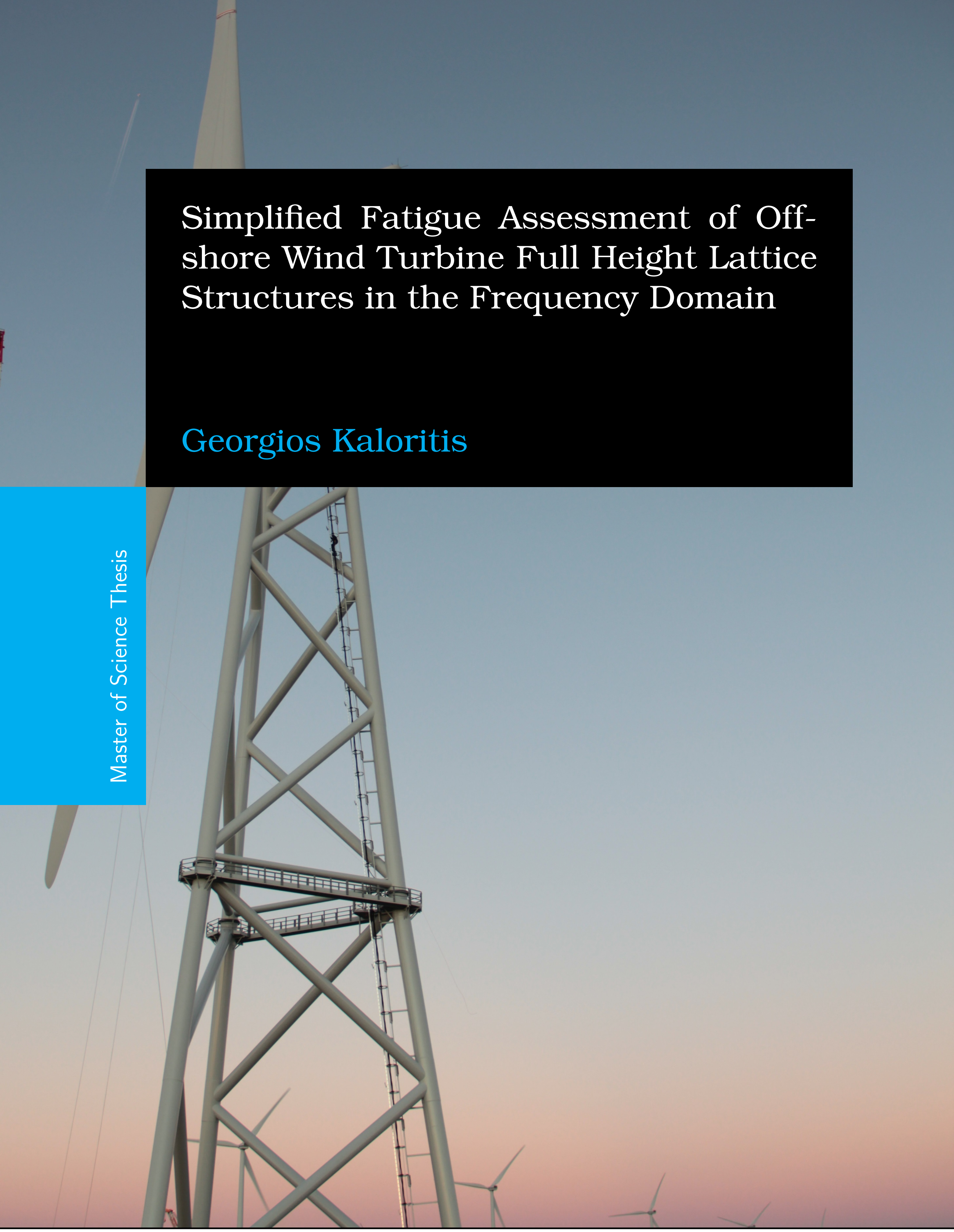

# Simplified Fatigue Assessment of Offshore Wind Turbine Full Height Lattice Structures in the Frequency Domain

Georgios Kaloritis

Master of Science Thesis

Delft University of Technology

2BENERGY

# Simplified Fatigue Assessment of Offshore Wind Turbine Full Height Lattice Structures in the Frequency Domain

Master of Science Thesis

For the degree of Master of Science in Sustainable Energy Technology at Delft University of Technology

Georgios Kaloritis
4390911

October 5, 2016

Faculty of Aerospace Engineerging (AE) and Electrical Engineering, Mathematics and Computer Science (EEMCS)

The work of this thesis was supported by 2-B Energy BV. Their cooperation is hereby gratefully acknowledged.

Delft University of Technology
Department of
Wind Energy, Aerospace Engineering (TU Delft)

The following academic staff certifies that it has read and recommends to the Faculty of Aerospace Engineerging (AE) and Electrical Engineering, Mathematics and Computer Science (EEMCS) for acceptance a thesis entitled

Simplified Fatigue Assessment of Offshore Wind Turbine Full Height Lattice Structures in the Frequency Domain

by

Georgios Kaloritis

in partial fulfillment of the requirements for the degree of

Master of Science Sustainable Energy Technology

Dated: October 5, 2016

Supervisor(s):

Dr. Ir. M. Zaaijer

Reader(s):

Prof. G. van Bussel

Dr. Ir. M. Zaaijer

Dr. Ir. E.M. Lourens

Ir. Jan Beerens

# Abstract

New concepts for support structures of offshore wind turbines have gained interest in the industry and are examined for intermediate and deep water depths. One of the main proposals that has already been commercialized is the three or four leg full height lattice structure. The fatigue assessment of such structures is of primary significance, since it is one of the main design drivers. A Frequency Domain (FD) framework is developed in this study with the ability of analysing several topologies of lattice structures for dynamic and fatigue assessment. The concept of the model relies on the natural frequencies and modeshapes estimation with the employment of the Finite Element Analysis (FEA) and the fatigue damage prediction due to wind and wave loading with the utilization of a Transfer Function (TRF) that relates the input spectrum to output stress spectrum for a member of the structure. Furthermore, the method of mode superposition is adopted for the calculation of the response of the structure. The benchmarking of the model for the dynamic analysis with ANSYS for a reference structure and turbine yields sufficient results with errors around 5% for the two first natural frequencies and even smaller for the higher modes. The Developed Model (DM) produces erroneous and sensitive results for the calculation of the torsional natural frequency. A case study of the structure developed by the Dutch company 2-B Energy is performed and the fatigue damage values as well as the stress spectra as computed by the DM are compared with the equivalent results calculated by the Time Domain (TD) software package GH Bladed for three different members. The DM produces satisfactory results for all the members for cases with low or medium environmental loading and less accurate results, which are pointing in the right direction, for the cases with high environmental loading. With the utilization of the DM for a preliminary analysis of a structure a significant amount of time (several hours) can be saved.

# Acknowledgements

I would like to express my gratitude to some people that have helped me throughout this thesis and their assistance has been essential for the realization of this work.

First of all, I would like to thank my supervisor Dr.Ir. Michiel Zaaijer for his support, attention and guidance. His constant availability and willingness of elaborating on all of my doubts and questions as well as his very targeted remarks have been proven to be crucial for the fulfilment of this thesis.

Furthermore, I would like to thank Jan Beerens, Alexander Jakubowski and Anish John Paul from 2-B Energy for supporting my efforts and contributing with their feedback on my work. I would also like to thank the Loads & Control Department of 2-B Energy for providing me access to GH Bladed without any restriction and for creating a pleasant atmosphere during all the times that I was there.

I would also like to thank Dr.Ir. Eliz-Mari Lourens for assisting me with parts of my thesis. Apart from that, my motivation and enthusiasm of getting involved with the offshore wind support structures topic, grew stronger because of her teaching on the corresponding courses.

Finally, I could not forget my friends and especially my family that have unconditionally supported me and have made it possible for me to achieve my dreams.

Georgios Kaloritis
Delft University of Technology
October 5, 2016

# Nomenclature

| | |
|---|---|
| $\alpha$ | Power Law Exponent |
| $log(\alpha)$ | Intercept of $logN$ axis by S-N curve |
| $\alpha_J$ | Parameter in the JONSWAP Equation |
| $\gamma$ | Enhancement Peak Factor |
| $\zeta$ | Wave Amplitude |
| $\theta$ | Rotation |
| $\lambda$ | Wavelength |
| $\xi$ | Damping Ratio |
| $\xi_n$ | Modal Damping Ratio |
| $\rho_s$ | Density of Steel |
| $\rho_{water}$ | Density of Water |
| $\sigma_i$ | Stress of the Element i |
| $\sigma_u$ | Standard Deviation |
| $\varphi$ | Normalized mode shapes of the structural system |
| $\psi$ | Mode Shapes of the Structural System |
| $\omega$ | Natural Frequencies |
| $a$ | Coefficient for Rayleigh damping |
| $b$ | Coefficient for Rayleigh damping |
| $C_T$ | Thrust Coefficient |
| $c_D$ | Drag Coefficient |
| $c_M$ | Inertia Coefficient |
| CSD | Cross-Spectral Density |
| d | Water Depth |
| D | Diameter |
| $D_{fat}$ | Fatigue Damage |
| DM | Developed Model |
| DOF | Degrees Of Freedom |
| f | Frequency |
| $f_M$ | Total Hydrodynamic Force |
| $f_D$ | Drag Hydrodynamic Force |
| $f_I$ | Inertia Hydrodynamic Force |
| F | Vector of Force Amplitude |
| FD | Frequency Domain |

| | |
|---|---|
| FEA | Finite Element Analysis |
| FEM | Finite Element Model |
| FFT | Fast Fourier Transformation |
| G | Shear Modulus |
| $H_s$ | Significant Wave Height |
| H | Transfer Function |
| i | Imaginery Unit |
| $L_v$ | Integral Length Scale |
| k | Wavenumber |
| KC | Keulegan-Carpenter number |
| m | Slope of S-N curve |
| MDOF | Multi Degrees Of Freedom |
| MSL | Mean Sea Level |
| N | Number of DOF of a System |
| $N_i$ | Shape Function ($i = 1, 2..$) |
| OWE | Offshore Wind Energy |
| OWPP | Offshore Wind Power Plant |
| OWT | Offshore Wind Turbine |
| PSD | Power-Spectral Density |
| $q_{i,n}$ | Generalized Coordinates of Element i for mode n |
| RNA | Rotor Nacelle Assembly |
| SCF | Stress Concentration Factor |
| SDOF | Single Degrees Of Freedom |
| $S_J$ | JONSWAP Spectral Density |
| $S_{FF}$ | Force Spectrum |
| $S_{FF,waves}$ | Total Wave Spectral Density |
| $S_{FF,I,waves}$ | Wave Spectral Density due to Drag Component |
| $S_{FF,D,waves}$ | Wave Spectral Density due to Inertia Component |
| $S_{ss}$ | Stress Spectrum |
| TD | Time Domain |
| TRF | Transfer Function |
| $T_p$ | Spectral Peak Period |
| $T_z$ | Zero Mean Crossing Period |
| $TI$ | Turbulence Intensity |
| u | Displacement |
| $u(x,z,t)$ | Water Particle Velocity |
| $\dot{u}(x,z,t)$ | Water Particle Acceleration |
| $U_w$ | Wind Speed at a Specific Height |
| $U_{w,r}$ | Wind Speed at a Reference Height |
| {x} | Geometric Coordinate Vector |
| $X$ | Vector of Displacement Amplitude |
| {Y} | Modal Coordinates |
| $z$ | A height above MSL |
| $z_r$ | A reference height above MSL |

# Table of Contents

# List of Figures

# List of Tables

# Chapter 1

# Introduction

This chapter familiarizes the reader with the topic treated in this thesis and provides background information that are essential for the conception of the current state-of-the-art technology and the main challenges that the Offshore Wind Energy industry faces. Next, the problem analysis follows with a description and clarification of the problem, and the approach to be implemented in this work is given. Finally, the ultimate target of this project, which results in the research question, is formulated and the structure of the thesis is provided in the last section of this chapter.

## 1-1 Background Information

In the last three decades Offshore Wind Energy (OWE) has been constantly under technological and economical development as a large-scale, clean energy technology and has found substantial ground for implementation in Europe and a continuously growing interest in the rest of the world. Within these years OWE has experienced three main stages, namely the initial research stage (1980-1990), the experimental testing stage (1990-2000) and the commercialization stage (2001-present) [45]. Despite the significant efforts for cost reduction especially in the last phase of the above mentioned era, there is still a lot of progress to be accomplished in order to render OWE financially more reliable.

This target becomes even more crucial as the OWE industry explores the possibilities of deeper water depths and gets involved with the construction of bigger wind farms where the design of an offshore wind power plant becomes more challenging. Taking into consideration the prospect of moving towards deep water applications, the supporting structure of the turbine becomes of crucial importance both from a technical and economic point of view. The support structure accounts for 10% up to 20% of the capital expenditure of an offshore wind power plant [21], depending on environmental and design characteristics and as it becomes apparent, seeking for an optimum support structure is of high priority. Among the potential existing support structure choices for an offshore wind turbine, the monopile is currently the most commonly used in the majority of the existing projects and projects under-development, as it is also depicted in Figure 1-1.

However, one important limitation connected with the utilization of monopiles is the respective water depth where the turbines can be installed. As the depth of the water becomes deeper, the height of the tower increases and the thickness of the tubular sections becomes very large. This results in a significant increment of the manufacturing costs and it generates great challenges associated with the transportation and installation of those heavy, steel structures in the field. For this reason and along with the emerging necessity of the exploitation of new potential markets with deeper water (Atlantic, Mediterranean, etc.) - as the report of EWEA (2013) [19] concludes - alternative types of support structure need to be employed and are already used. The importance of the support structure in the overall design and in the cost-efficiency of an offshore wind power plant is also highlighted in the European UpWind project [17], where a number of existing and concept designs are considered, such as tripods, jackets, gravity based foundations, etc.

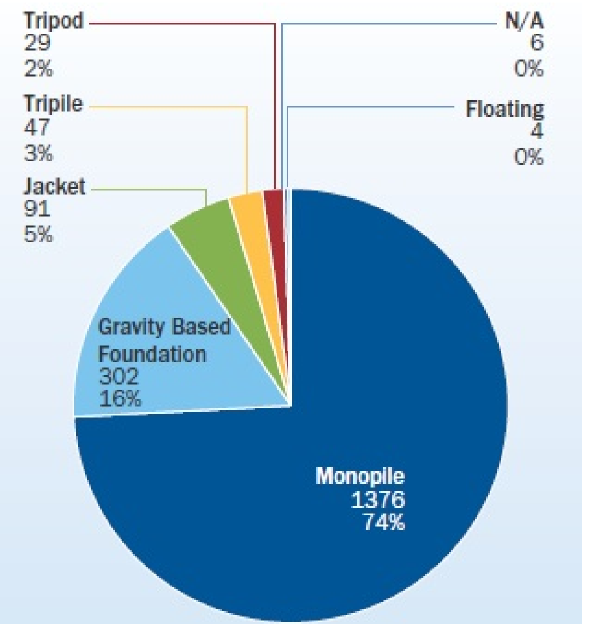


**Figure 1-1:** Share of installed support structure types by the end of 2012 (units). [19]

Among those conceptual designs, one promising alternative for intermediate water depths (30-70 m) is acknowledged to be the full height three or four legged lattice structure. This concept does not make use of the conventional tubular tower of the wind turbine and the lattice continues up to the Rotor Nacelle Assembly (RNA), in contrast with all the other support structure potentials. Lattice structures are considered to be an alternative design of the commonly used jacket in the oil & gas industry and it is not a new and innovative design for wind turbines, since in the early phases of the development of onshore wind energy it was the predominant support structure. However, it was slowly superseded by the tubular tower for various reasons that can be found in greater detail in [35]. Currently, this type of structure has become again the object of research and commercialization for offshore-oriented projects mainly from the Norwegian University of Science and Technology (NTNU) [36] and the Dutch company 2-B Energy [1], respectively.

According to Muskulus, Long and Moe, who researched the lattice structure for OWE applications, but also from several other researchers who have studied the dynamics and the reliability of bottom fixed structures (mainly jackets) for the oil & gas industry, such as Vughts and Kinra, Barltrop and Adams, Wirsching, Bishop and several others, it is suggested that fatigue becomes the design governing factor and multiple theories and frameworks have been formulated in order to accurately predict the real-life fatigue damage. Numerous algorithms have been developed both in the frequency domain in the early phases of the oil & gas industry prosperity and in the time domain later and in parallel with the increasing computer capabilities. However, the latter algorithms are time-intensive and even today require computers with advanced characteristics.

On the other hand the frequency domain methodologies in the oil & gas industry were developed with the given fact of low computer capacities (in comparison with the current state) and their main objective was the creation of simplified but efficient algorithms. Later on and especially in the beginning of the $21^{st}$ century similar frameworks were deployed for the offshore wind industry and aimed mainly at monopile structures and at the preliminary design phase, where the highly iterative nature of the design process with different potential solutions for mass minimization needs to be examined and time efficiency becomes essential. Some of the most notable examples are the works conducted by Kühn in 2001 [27] and van der Tempel in 2006 [47].

## 1-2 Problem Analysis

When considering the preliminary design phase of support structure selection and optimization it becomes evident to the engineer that an efficient framework able to perform rapid calculations for parametric variation and optimization of the geometry as well as the ability of accurate estimation of the dynamic behaviour of the structure is more than essential. While initially this goal seems to be feasible, due to the increased existing computational power and the continuous development of sophisticated time-domain simulation programs, it does not entirely represent the reality.

Time-domain software packages require a detailed description of the geometry of the structure as well as other relevant information that might not be fully defined in the preliminary design phase of a project. Evidently, the characterization of a structure on such a detailed level might be a time consuming process and it prohibits in some cases the investigation of alternative designs. This argument gains momentum, when in the early stages of the formulation of the project, a fatigue analysis needs to be included, since for the bottom fixed type structures it is a governing design characteristic (as mentioned in the previous section). Thus, it becomes apparent that also a sufficient accuracy of fatigue damage estimation is of high importance, which adds up an extensive amount of computational time.

However, and without considering for the moment the parameter of time efficiency, Time Domain (TD) calculations can sometimes be cumbersome to perform, because of the complete and complex models that are required for the aerodynamics, control, drive train, etc., which are not available (at least not with great details) at the early design phase. Furthermore, as van der Tempel argues [47] the situation where the support structure contractor might lack of definite information about the wind turbine model to be used up until the advanced stages of the design, it is not so infrequent.

All of the above arguments show that although TD simulations are and should be the prevailing framework for detailed and accurate results, there is also a high necessity for the existence of an alternative scheme aiming at the preliminary design phase with main focus on time efficiency and not fully dependent on the complete and detailed description of all the components of an Offshore Wind Power Plant (OWPP). This framework can be developed within the Frequency-Domain (FD) and could give the opportunity for site specific support structure design, parametric variation and optimization of complex structures, such as the full height lattice structure.

Although there is already present an extensive experience in the FD framework from the oil & gas industry and proven methodologies developed for dynamic analysis and fatigue calculation of offshore platforms, the conditions certainly differ when one considers an OWPP. Several challenges arise when offshore wind turbine support structures are examined in the FD, such as the derivation of a fully linear model for the wind turbine and integration in the calculations of the wind effects present on the system that are usually neglected in the oil & gas industry [5].

However, and as it has been proven from similar algorithms developed for the offshore wind energy industry in the FD, there are ways to overcome those barriers by appropriate assumptions and approximations that can be regarded sufficient for the early design stage. Sorensen [43] states that the rapid execution of an FD algorithm is eminently suited for parametric studies aiming at investigating the effect of changing structural and aerodynamic parameters. As it becomes clear, a methodology developed in the FD for fatigue analysis of complex offshore wind support structures might be the solution that an engineer seeks to the problem, as it was described in the beginning of this paragraph.

The next section provides the requirements of such a framework developed for a full lattice structure and the objectives of this thesis are defined.

## 1-3 Research Objectives

The two previous sections identify the necessity of the market for the employment of new types of support structures more applicable for deeper water depths than those that a monopile can be used for and present the challenges connected with dynamic analysis and fatigue damage estimation for more complex offshore wind support structures, such as the full height lattice structure. They also introduce the requirement for the development of a methodology able to assess lattice structures with main characteristics the time efficiency and a sufficient level of accuracy.

Furthermore, from the short introduction of the above paragraphs it can easily be understood that the FD is or at least should be the preferred option for a fatigue analysis in the early design phases of a support structure and indeed there is a sufficient theoretical basis and a number of existing algorithms that can with high accuracy perform this task especially for monopiles. However, when it comes to a different type of structure then the following questions arise:

1. How can the existing methodologies of the oil & gas industry and the algorithms developed for monopile structures, be modified and integrated into a new algorithm with the ability of assessing full height lattice structures?
2. What is the level of accuracy on dynamic analysis and fatigue damage estimation of such an algorithm and how credible could it be for structural variation and design optimization?
3. In which aspects can such a framework be advantageous when compared to sophisticated TD software packages?

It is evident that since the offshore wind energy industry explores new possibilities in the frequency domain, the above concerns need to be clarified by taking into account the different dynamic characteristics of each type of structure. It has been presented above that the full height lattice structure is a promising concept for future projects and has gained attention from both the research and the industry sectors.

Therefore, the research objective of this project is identified in the questions posed above and in this report effort will be paid in trying to answer them through the development of a model in the FD, able to assess full height lattice structures. A subsequent target is the exploration of the dynamic characteristics of such structures for offshore wind turbines applications.

## 1-4 Thesis Outline

The present thesis consists of 7 main chapters. Chapter 1 provides an introduction of the topic treated and some relevant information that present the background scope, which leads to the development of the algorithm examined in this report. Next, in Chapter 2 the requirements of the algorithm are given and is presented how the existing methodologies and frameworks from the oil & gas and the offshore wind energy industry can be combined to formulate an algorithm for dynamic and fatigue analysis of full height lattice structures.

The following three chapters deal with a detailed explanation and breakdown of the main stages of the algorithm under investigation and show the methodologies employed at each different step and how they have been integrated in the developed model. More specifically, Chapter 3 treats the dynamic analysis of the structure that has a significant role on the correct estimation of the dynamic response and on the fatigue damage approximation. It presents how a structure can be described in the developed model and how with the use of the finite element analysis, the dynamic behaviour of such a structure can be assessed. Chapter 4 deals with the methodologies used to model the random input loading, cause by wind and waves and then Chapter 5 presents the derivation of appropriate transfer functions that can translate the above mentioned random loading into a dynamic behaviour of the structure and as a result into a fatigue damage estimation of members of the structure.

Finally, Chapter 6 is a case study for the structure developed by the Dutch offshore wind energy company 2-B Energy that has commercialized a full height lattice structure. This case study acts also as a verification of the developed model, since the results extracted from the model in the FD are compared with the TD software GH Bladed. Finally, Chapter 7 provides the conclusions of the work conducted in this thesis and presents some suggestions for future implementation.

## Chapter 2

# Methodology Overview

The current Chapter deals with the framework obtained in this Thesis for the development of a model with the ability of fatigue estimation for full height lattice structures for offshore wind energy applications.

## 2-1 Introduction

The algorithm applied in this project follows established methodologies, evolved in the early phases of development of the offshore structures mainly for applications in the oil & gas industry for fatigue damage estimation in the frequency domain with prominent examples of work being [6], [52], [50] and [5]. However and as it can be understood, an offshore wind turbine system differs (mainly from a dynamics perspective) from an offshore structure designed for other purposes. For this reason and along with the necessity that emerged from the growth of the offshore wind energy, specifically designed frameworks for fatigue prediction on offshore wind energy structures were developed in the beginning of the $21^{st}$ century.

Nevertheless, those algorithms were created mainly for the state of the art support structure of offshore wind turbine systems, which is the monopile. In this report effort will be put in integrating those algorithms on a different type of support structure, which is the full height lattice structure. The methodology followed has many similarities with those employed by van der Tempel [47] and Kühn [27], but there are also certain steps, where a different approach was preferred. Those steps will be pointed out and explained in a greater detail.

In the sections that follow, the proposed methodology is provided and in the subsequent chapters it is shown how this methodology can be integrated in the model for fatigue damage estimation on lattice structures.

## 2-2 Key Requirements of the Algorithm

It has been pointed out several times in the introduction that one of the major preconditions of a framework for fatigue analysis of framed structures is time efficiency. Of course the preciseness of the results is at no point overshadowed here, but at a preliminary design stage the main objective is to come up with a high-level design that meets the initial requirements and the level of accuracy of the outcome can usually facilitate a sufficient margin of deviation from the real value. In this sense, it can be interpreted for the present algorithm that the computational performance is considered more important than precise prediction of the absolute value (without meaning that less interest is paid at the outcome).

The amount of emphasis given at the time efficiency is also connected with the second requirement of the algorithm, which is the ability of optimization of the structural design and parametric variation of the structural components. Time domain fatigue analysis is certainly not an optimal framework especially for lattice type towers including a large amount of members and joints for optimizing the design or investigating the effect of a structural change [29]. However, the structural optimization will not be included in the current examined scheme. This is because primarily is considered of greatest significance to investigate in depth each step of the introduced methodology and on a later phase to get involved with an optimization procedure. This argument will be further discussed in Chapter 7.

A third and final condition of the developed methodology is connected with the complexity of the scheme. The algorithm should with a minimum amount of input be able to perform the necessary calculations and arrive at a final damage value.

## 2-3 Selection of the Frequency Domain

Although it was shortly explained in the introductory chapter of this report, the advantages of the FD over the TD and the reasons why a framework in the FD was adopted in the present model are once again stressed in this section.

In principal the driving dynamic excitations for fatigue, i.e. wind and waves, should be considered in a completely integrated non-linear time domain simulation, where the loading from the wind and the waves is generated simultaneously in order to account for the coupling between aerodynamic and hydrodynamic responses [27]. However, this approach requires an extensive computational effort, that even for computers equipped with current technology can be proven to be a major drawback in the early design phases or during an optimization procedure of the support structure of an offshore wind turbine system.

Thus, it becomes evident that a different simplified approach that will be time-efficient and still obtain reliable results for fatigue analysis is of crucial importance and has been the target of many researchers of the last two decades. However, this research effort has resulted in mainly two methods of particular interest that combine the high computational efficiency with the generation of results that are in good agreement with TD simulations and those are the FD algorithms developed by Kühn and van der Tempel [2].

Consequently, it can be understood that an algorithm derived in the FD for the fatigue prediction in the model is in complete accordance with the key requirements as they were described in Section 2-2.

## 2-4 Principal Assumptions

The algorithm adopted in this thesis and presented in the following section has as starting point the methods derived by van der Tempel and Kühn (that can be found in the literature [47] & [27] for more detail) including some necessary adaptations in order to be applicable for lattice type structures. As a consequence, it incorporates all of the assumptions connected with those methodologies, which for clarification reasons are also introduced here:

- Wind and wave loadings can be regarded as independent and stationary processes[1] on a short time scale (ten minutes for wind and three hours for waves).
- Geometric non-linearities do not play a significant role for fatigue response.
- The magnitude of the stress in the soil due to wind and/or wave fatigue loading is small compared to the ultimate strength. Thus, the soil behaviour can be assumed to be linear.

The significance of the first assumption can be realised when one considers that the complete separation of the wind and wave responses provides the ability of calculating the total stress response by just adding the independent responses. This simplification to the approach is in accordance with the requirements set in Section 2-2, while maintaining an excellent agreement with experimental data recorded in offshore sites [2].

## 2-5 Fatigue Calculation Method in the Frequency Domain

The starting point of any fatigue analysis is the response of the structure or a component due to an input excitation [22]. As Kühn states there are four steps included for a fatigue calculation in the FD and are namely a) Stochastic environmental modelling, b) Calculation of the structural response, c) Establishment of the stress range distribution and d) Damage accumulation. Those four steps can be also identified in Figure 2-1. However, in the scope of this report a slightly different subdivision of the above described steps will be used, which matches better with the modelling activities performed for the implementation of the method. Those 4 stages can be regarded as follows:

1. Structural model derivation.
2. Modelling of the load inputs (green circles).
3. Transfer function derivation.
4. Fatigue damage calculation.

It should be pointed out here that stage 3, namely the Transfer Function (TRF) derivation, refers to a TRF, which connects an input load spectrum to a stress spectrum for a member

[1]Strictly speaking those processes are not completely stationary but can be visualised in such a way.

of the structure. For the time being, this process can be visualised as a "black box", but its characteristic attributes require further analysis that will follow in the coming chapters.

In the subsequent chapters, each stage presented in Fig. 2-1 will be individually and thoroughly examined. Whenever it is considered necessary some background information theory will be provided with the purpose to help the reader understand the scheme in greater detail. The developed model has been built in Matlab and employs the algorithm of Fig. 2-1.

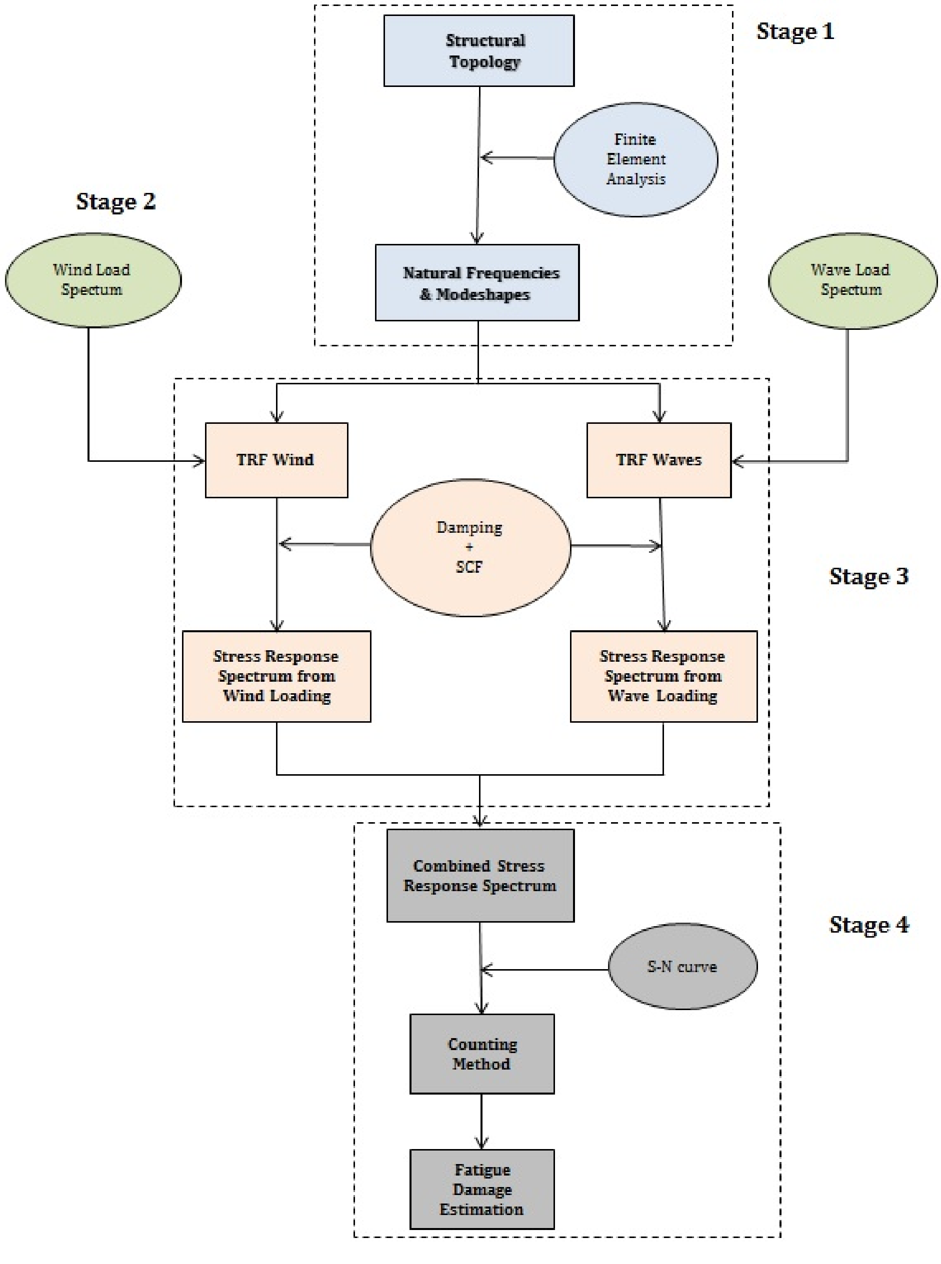


**Figure 2-1:** Principal algorithm for fatigue damage estimation in the frequency domain.

# Chapter 3

# Structural Model

Key requirements of the model are its ability of representing different structural topologies and yield sufficient results with respect to fatigue damage estimation, while taking into account location specific characteristics, such as water depth, soil properties, etc. As presented in the methodology flowchart, starting point of the assessment is the correct representation of the real structure with its own characteristics and attributes. It will be understood by the end of this Chapter that the Finite Element Analysis (FEA) is a powerful framework for this purpose and has a substantial importance for the correct evaluation of the dynamic behaviour of the structure and as a result for the fatigue damage calculation.

## 3-1 Basic Theory of Finite Element Analysis

As stated above and leaving aside for the moment the representation of the structural geometry of a full height lattice structure, the finite element analysis is considered to be one of the major steps of the methodology presented in Fig. 2-1. This is due to the fact that the correct computation of the natural frequencies and the mode shapes of the structure plays a significant role in the accurate representation of the dynamic behaviour of the structure and -as it will be shown later- the derivation of the response of it to a random loading, which will result in the calculation of the fatigue damage.

The finite element method involves the modelling of the structure using small interconnected elements called finite elements. Every interconnected element is linked to every other element by using common interfaces or nodes. By using known properties for the material making up the structure, one can determine the behaviour of a given node in terms of the properties of every element in the structure [28]. According to Logan [28] there are seven steps included for an appropriate representation of a structure and those are namely:

1. Discretize the domain and select the element type.
2. Select a displacement function.

3. Define the strain/displacement and stress/strain relationships.
4. Derive the element stiffness matrix and equations.
5. Assemble the element equations to obtain the global equations and introduce boundary conditions.
6. Solve for the unknown Degrees Of Freedom (DOF).
7. Solve for the element strains and stresses.

A more detailed explanation of the above steps as well as following precisely this methodology in the derivations that are presented below is not in the scope of this current report and the reader can refer to the substantial amount of literature that exists for the finite element analysis method. The connection between a physical system (structure) and its idealized with finite elements model is depicted in Fig. 3-1.

At this point and before moving on to the next sections, it is necessary to make an essential distinction in terminology in order to enhance communication and understanding between the physical model of the structure and the finite element representation of it. For the remaining of this report, the terms *nodes* and *elements* will refer to the finite element model and the terms *joints* and *members* will refer to the physical model and the real connections between the different components (viz. a connection between a brace and a leg).

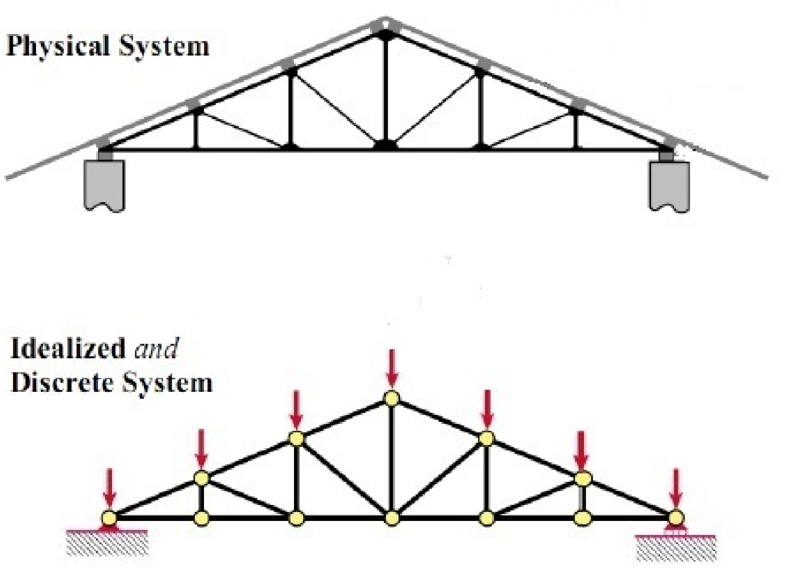


**Figure 3-1:** Top: Physical model of a structure. Bottom: Idealisation of the physical model with finite elements [7]

### 3-1-1 Stiffness, Mass and Damping Matrices

Before presenting the properties such as the stiffness, mass and damping matrices of the elements that will constitute the structure, the type of element should first be considered. In the majority of framed structures such as a lattice structure, the beam element is regarded to represent the behaviour of the real model in the most realistic way [6]. The best known models for beams are the so called *Euler-Bernoulli* and the *Timoshenko* beams. Their differences can be found in the literature; the main characteristic of the Euler-Bernoulli beam is that it neglects the transverse shear deformations, whereas the Timoshenko beams do not. However, within the frame of this thesis the Euler-Bernoulli beam is considered to yield sufficient results, since for beams with a relation between length and thickness large enough, the error between both model is considered to be small. For this reason the Euler-Bernoulli beam is selected for the FE model.

Each beam element is examined in the three dimensional space and has two nodes with six degrees of freedom. The DOF represent displacements and rotations around the three axes as it is shown in Fig. 3-2. All of the elements have characteristic mechanical properties such as stiffness, mass and damping properties that when assembled together for all of the elements of a Multi Degree of Freedom (MDOF) structural system, they can formulate the equation of motion of the whole system that can be described by Eq. 3-1:

$$[M]\{\ddot{x}\} + [C]\{\dot{x}\} + [K]\{x\} = \{F\} \tag{3-1}$$

where [M], [C] and [K] are the system mass, damping and stiffness matrices respectively, that as already stated are created by properly adding the element mass, damping and stiffness matrices. The stiffness and mass matrices of a 3-D Euler-Bernoulli beam element can be found in Appendix A. The $\{x\}$ and $\{F\}$ vectors represent the displacement and the force vector and are associated with each DOF of the system. The $\{\ddot{x}\}$ and $\{\dot{x}\}$ are the vectors for acceleration and velocity of each DOF respectively.

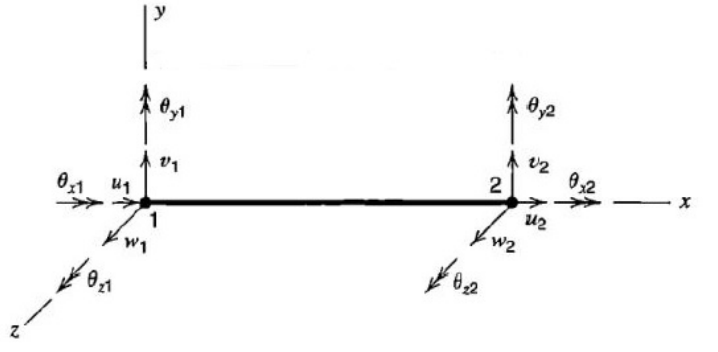


**Figure 3-2:** Beam element with 2 nodes and 6 DOF per node in the local coordinate system (x-axis parallel to the length of the beam). [16]

**Damping**
According to Cook [16] damping is the process of energy dissipation that causes a free vibration to decay with time and limits the amplitude of vibration produced by a loading whose frequency is in the region of a natural frequency of the system. In practice the damping characteristics are not well known and the overall structural damping is usually estimated with developed models according to the application. Main categories of damping that influence structural dynamics are briefly (for a more detailed analysis the reader can refer to [16]):

- Viscous damping also known as Rayleigh damping.
- Hysteresis or soil damping.
- Coulomb damping.
- Radiation damping.

From the above mentioned physical kinds of damping only viscous damping is easy to represent in dynamic equations. Due to the fact that in structural applications damping is usually small, regardless the actual source, its effect on the structural response can be modelled well enough by considering it as viscous [16]. Rayleigh damping or else viscous or proportional damping, defines the global matrix $[C]$ as a linear combination of the global mass and stiffness matrices, as shown in Eq. 3-2:

$$[C] = a[M] + b[K] \tag{3-2}$$

This equation makes damping frequency dependent and for a Single Degree of Freedom (SDOF) system, the values $a$ and $b$ can be easily found as a fraction of the critical damping. However, for systems with many DOFs it becomes more difficult to derive meaningful values for the Rayleigh damping coefficients. In order to do so and to account for lower and higher modes of the structure that have a different result and contribution on the response of the model, the method derived and described by Chowdhury [13] is applied in this thesis. This method makes use of both lower and higher modes of the system and as a consequence to each mode of the structure corresponds a value for the damping ratio arriving in such way to a more realistic picture for the behaviour of the structure under random loading. The $a[M]$ contribution damps lower modes most heavily, whereas the $b[K]$ has a greater contribution to the damping of higher modes.

An important property of proportional damping is that vibration modes are orthogonal with respect to $[C]$. This means that a structure with N DOFs can be reduced to N uncoupled equations. The significance of this attribute will be better understood when the transfer function derivation for the environmental loading will be discussed in the subsequent chapters.

### 3-1-2 Local and Global Coordinate Systems

The local and global coordinate systems are connected with the $4^{th}$ and $5^{th}$ step as presented in Section 3-1. The elements have a local coordinate system (x, y, z), with the x-axis directed along the length of the beam, as shown in Fig. 3-2. Proper selection of the three dimensional global coordinate system (X, Y, Z) can be chosen according to the application and in this case the preferred system is the one depicted in Fig. 3-3. The z-axis is pointing upwards, with positive values above the Mean Sea Level (MSL) and the x-axis is parallel to the wind and wave propagation.

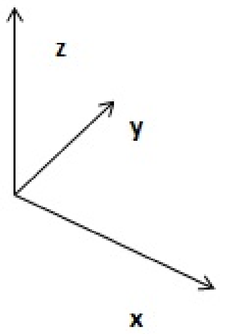


**Figure 3-3:** Global coordinate system used in the developed model. The z axis is pointing upwards.

### 3-1-3 Modal Analysis

As it was stated above, the modal analysis (natural frequencies and mode shapes) is one of the most important steps of the algorithm presented in Fig. 2-1 not only because it gives a good insight of the dynamic behaviour of the structure, but also due to the fact that for the estimation of the fatigue damage, the mode shapes are an indispensable part of the methodology (as it will also be presented in Chapter 5).

The natural frequencies and the mode shapes of the system can be calculated from an eigenvalue analysis of the undamped free vibration system as shown in Eq. 3-3:

$$[M]\{\ddot{x}\} + [K]\{x\} = 0 \tag{3-3}$$

Eq. 3-3 can be expressed as an eigenvalue problem of the matrix in the square brackets in Eq. 3-4, which is called dynamic stiffness matrix:

$$[K - \omega^2 M]\{x\} = 0 \tag{3-4}$$

where $\omega^2$ is a vector containing the $N$ eigenvalues $\{{\omega_1}^2, {\omega_2}^2, ..., {\omega_n}^2\}$ of the system. The roots of the eigenvalues represent the natural frequencies of the $N$ degrees of a system. The mode having the lowest frequency is the first mode, the next higher is the second mode, etc. The matrix of eigenvectors related with Eq. 3-4 represents the relative amplitude of every DOF at each of the natural frequencies, which is the deflected shape of the system called the mode shape [5]. Each column of the matrix shown in Eq. 3-5 serves as the mode shape of the system, when this is excited at a certain natural frequency. A physical interpretation of Eq. 3-4 can be realized when it is expressed in the form $K\{x\} = \omega^2 M\{x\}$, where it could be stated that a vibration mode is a configuration in which elastic resistances are in balance with inertia loads [16].

$$\boldsymbol{\psi} = \begin{bmatrix} \boldsymbol{\psi_1} & \boldsymbol{\psi_2} & \dots & \boldsymbol{\psi_n} \end{bmatrix} = \begin{bmatrix} \psi_{11} & \psi_{12} & \dots & \psi_{1n} \\ \psi_{21} & \psi_{22} & \dots & \psi_{2n} \\ \vdots & \vdots & \ddots & \vdots \\ \psi_{n1} & \psi_{n2} & \dots & \psi_{nn} \end{bmatrix} \tag{3-5}$$

It is common to normalize the mode shapes when the modal model is going to be used for structural modification or for structural response estimation. There are several methods of performing this calculation and in this report the mode shapes are normalized according to the methodology presented in [31] that is known as mass normalization and is preferred for computer calculations. By normalizing the mode shapes there are some conditions that have to be satisfied, namely the orthogonality conditions, and these are provided in the equations that follow:

$$\begin{aligned} \phi_m M \phi_n &= 0 \\ \phi_m K \phi_n &= 0 \\ \phi_m C \phi_n &= 0 \end{aligned} \tag{3-6}$$

Where m and n represent different modes and $\phi$ are the normalised mode shapes. However, more important here for the determination of the structural response are the equations as presented in Eq. 3-7:

$$\begin{aligned} \phi_n^T M \phi_n &= I \\ \phi_n^T K \phi_n &= diag(\omega_n^2) \\ \phi_n^T C \phi_n &= 2\xi_n \omega_n M_n \end{aligned} \tag{3-7}$$

Where $I$ is the identity matrix and $\xi$ is the damping ratio of each mode. Emerging from the properties of the Rayleigh damping, as it was presented in Sec. 3-1-1, here can be noticed that the orthogonality attributes of the proportional damping have already a significant contribution in satisfying the orthogonality conditions of the system.

After this small introduction to the FEA theory, the remaining of this Chapter deals extensively with the analysis of the block of stage 1 of the employed algorithm as presented in Fig. 2-1, while making use of the properties presented above and demonstrates how the model created within the context of this thesis creates the idealised finite element model of a real lattice structure.

## 3-2 Topology and Lattice Tower Design

As shortly mentioned in Chapter 2, one of the model requirements is that it should have the capability of analysing structures with different topologies, so that the user will be able to have an indication of the type of lattice tower that best suits a certain location and a certain turbine. Some possible configurations that can be investigated are structures with 3 or 4 legs, "X" or "Z" (see Fig. 3-4) bracing patterns and sections separated with horizontal braces. Some of the feasible topologies are depicted in Fig. 3-5.

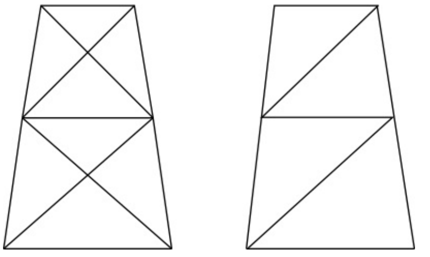

**Figure 3-4:** "X" and "Z" bracing patterns.

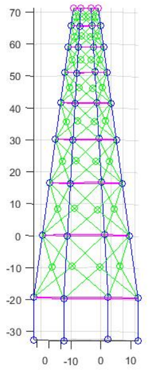


**(a)** Lattice tower with 4 legs and "X" braces.

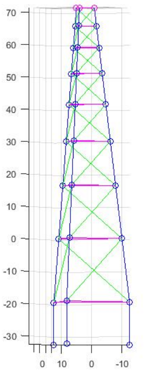


**(b)** Lattice tower with 3 legs and "Z" braces.

**Figure 3-5:** Example of possible structural topologies.

For the representation of the structure, only the real joints and members of the tower are depicted. This means, that the nodes appearing in Fig. 3-5 illustrate the real welding between parts of the physical model, such as the connection between a brace and a leg. Nonetheless, for the sake of simplicity those members are attached on the same node, which is not entirely correct for the real structure. Normally, there is a gap as seen in Fig. 3-6, which is the distance along the chord between the weld toes of the braces. By ignoring this gap the local joint flexibility is affected and might produce erroneous results with respect to the distribution of bending moments at nodes and the distribution of axial forces in the legs of the structure. However, as Barltrop [5] and Long and Moe [29] also suggest, the local joint flexibility effect is quite complicated and is generally neglected.

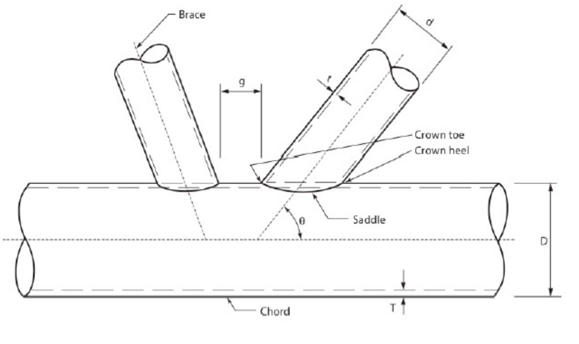


**Figure 3-6:** Joint characteristics (g denotes the gap).

## 3-3 Reference Structure and Turbine

In order to investigate the adequacy of the model and to benchmark the results with commercial software a reference structure must be used. The design of the lattice tower was chosen to be similar to common jackets combined with tubular towers used in offshore wind turbine industry. The characteristics and dimensions of the structure are presented in Table 3-1 and those values were taken from the "UpWind Reference jacket" report [49] and [55]. The structure has 4 legs, 12 sections and the bottom distance between two legs is 25 m. The batter angle of the structure is constant along the height and equal to $5^o$ and each bay section has a brace angle of $38^o$. Those values per bay along with addition of some turbine characteristics, such as Rotor Nacelle Assembly (RNA) mass, inertia, etc. are the required input values that need to be defined from the user. In Fig. 3-7 some of the above terminology for jacket structures is visually explained.

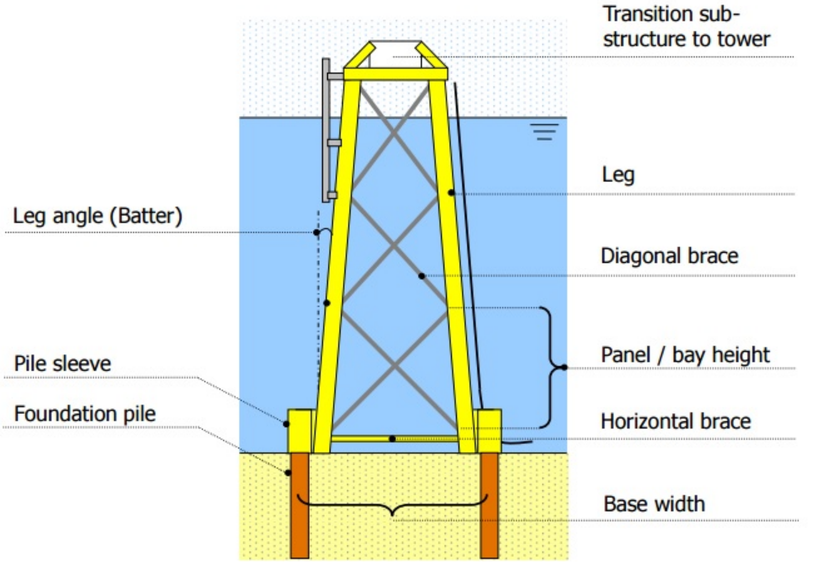


**Figure 3-7:** Structural characteristics of a jacket structure [32].

**Table 3-1:** Property sets of reference lattice tower.

| Component | Outer Diameter [m] | Thickness [mm] |
|---|---|---|
| Leg | 1.2 | 40 |
| Horizontal | 0.6 | 20 |
| Diagonal | 0.6 | 20 |
| Pile | 2.082 | 60 |

The material considered is structural steel (S355) with density $\rho_s = 7850 kg/m^3$ and Young's modulus E $= 210GPa$. However, since the model does not take into account for the mass calculation the secondary steel present in the tower, such as boat landing tubes, pipes or even an access ladder along the whole length of a leg (which is a common practice for accessing the turbines in these structures), the density of the steel is increased by 1 % in order to compensate for this omission. The representation of the physical model of the reference structure is displayed in Fig. 3-8 and is placed on a site with water depth 35 m (in the figure is visible that the structure extends more than 35 m, but this is due to the foundation model used, as it will be explained in the upcoming sections).

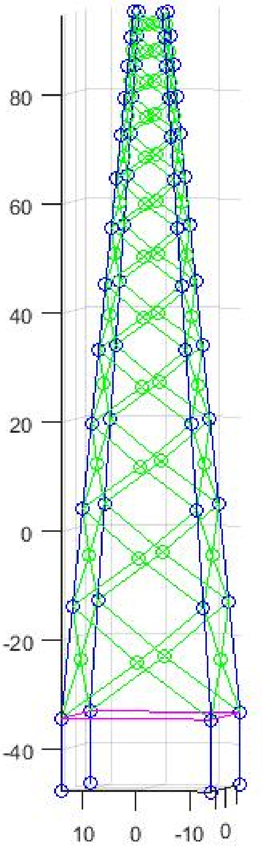


**Figure 3-8:** Representation of the physical model of the reference lattice structure used for the development of the model.

As already stated above, the model requires some characteristic input values for the turbine and the transition piece, such as the mass, the inertia and the centre of gravity. Lattice type support structures make use of a simple cylindrical or conical transition piece that connects the top of the structure with the yaw bearing of the turbine [29]. The reference turbine considered in this thesis is the 5 MW NREL reference wind turbine for offshore applications with properties as presented in Table 3-2. In the following sections the idealization of the physical model of lattice structures with finite elements will be presented.

## 3-4 Finite Element Model

This section makes use of the theoretical basis that was provided in the beginning of this chapter and analyses the modelling of the different elements, such as the RNA and the foundation components, that are integrated in the model in order to represent the actual structure as realistic as possible.

**Table 3-2:** Gross properties for the reference wind turbine [25].

| | |
|---|---|
| Rating | 5 MW |
| Number of blades | 3 |
| Rotor diameter | 126 m |
| Cut-in, Rated, Cut-out wind speed | 3, 11.4, 25 m/s |
| Cut-in, Rated, Cut-out rotor speed | 6.9, 12.1 rpm |
| RNA mass | 350 tons |

### 3-4-1 Mesh Generation

For the creation of the finite element idealized model of the structure, the number of elements per member or else the mesh has to be defined. The mesh generation can be coarse or fine as presented in Fig. 3-9, with an expected difference between those two options in the calculation of the modal analysis. What this means is that a fine mesh will estimate the natural frequencies and the mode shapes with an accuracy closer to reality than the coarse mesh will do, with the cost being increased computational time.

In the end of this chapter a comparison between different mesh densities and the effect that they have on the calculation of the natural frequencies and mode shapes is provided.

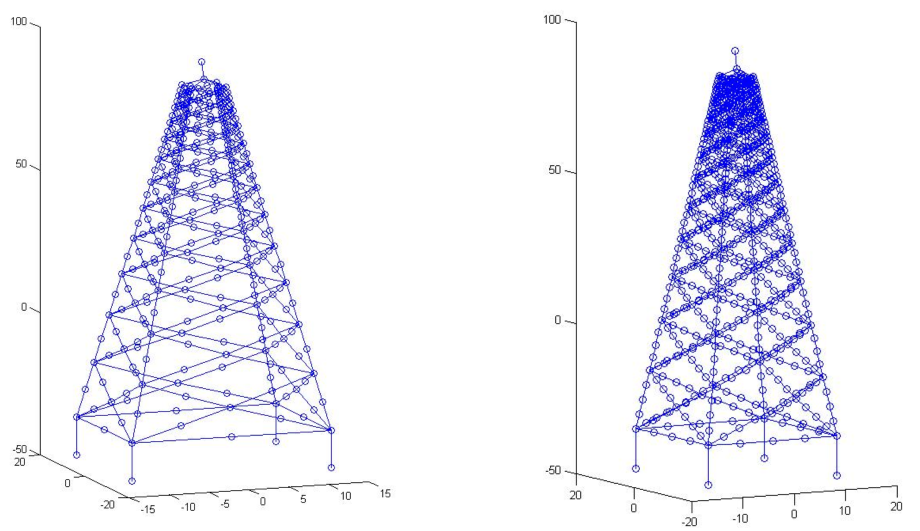

**(a)** FE model with 2 elements per member. **(b)** FE model with 4 elements per member.

**Figure 3-9:** FE model of the reference structure.

### 3-4-2 RNA and Transition Piece Modelling

Because the purpose of the model is to analyse the dynamic behaviour of the structure, it becomes evident that all of the components that highly influence its response need to be treated accordingly and be taken into consideration. Such components are the RNA and the transition piece as well as the model that will emulate the effect of the foundation on the whole system. Thus, those elements have to be integrated in the FE model as well.

As far as the RNA is concerned, a complete and detailed FE model of it would be a cumbersome task, since it is constituted by several complicated components. This assignment is outside the scope of the present thesis and as a result a more simplistic approach needs to be followed. The attributes of the RNA that are essential for the dynamic behaviour of the structure are the mass and inertia characteristics. Hence, the RNA can be modelled as simple as a single point-mass node (it can be visible at the top of the structure in Fig. 3-9) that has the same mass and inertia properties as the real turbine and is connected with the rest of the system through beams of very high stiffness, so that the movement of the turbine is following the movement of the structure and vice versa.

Similarly, the transition piece can also be modelled as a single point-mass node with the characteristics of the real component, connected in the same way as above with the structure. For the transition piece this approach is not an oversimplification of reality, since as it has also been mentioned in Sec. 3-3 the transition piece of such a structure is usually a simple conical or cylindrical component, which does not introduce any special mass or inertia characteristics in the system. In this way the properties of the RNA and the transition piece are taken into account and they have a realistic contribution to the response of the structure.

### 3-4-3 Foundation Modelling

The dynamic behaviour of offshore wind turbines is highly influenced by the conditions that exist at the seabed of a specific location. The soil's strength and stiffness properties, as well as the pore water pressure may affect the way that the structure is loaded and the soil - structure interaction. The flexibility of the soil makes this interaction system less stiff than a fixed base (as it would be the case for an onshore wind turbine) and as a result the natural frequency of the system is increased, which tends to decrease the dynamic response of the structure [5]. The foundations of fixed offshore structures are subjected to dynamic loading from a number of sources, such as pile driving forces, drilling and mainly environmental loads (waves, currents and earthquakes). Within the context of this thesis, only the environmental loads are treated apart from the earthquake loading, which is considered insignificant for the North Sea region [9].

For the foundation modelling there have been several models proposed and each one arrives at better results with respect to natural frequency calculation for different type of support structures. The foundation model employed in this thesis is the effective fixity length. In this model the clamping effect of the soil is replaced by rigid clamping of the pile at an effective depth below the seabed. The proposed fixity depth for lattice structures presented in [54] is 6D, where D is the pile diameter. As it is visible from Fig. 3-10 this model estimates the first natural frequency with an error of approximately 1-2 %. For a more in depth analysis and comparison of different models, it is suggested to the reader to refer to the literature [54], [10].

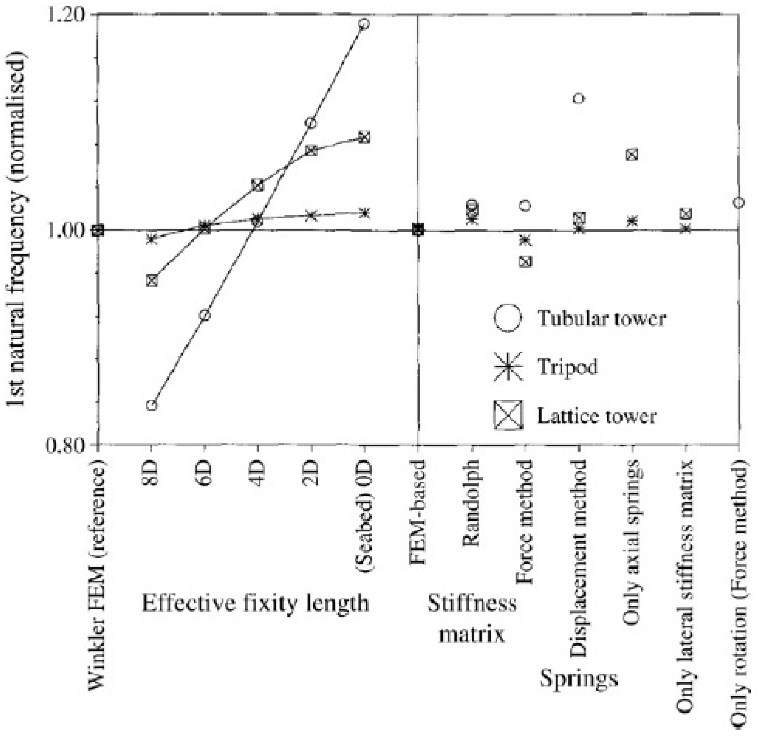


**Figure 3-10:** Predicted first natural frequency for several foundation models [54].

### 3-4-4 Structural, Aerodynamic & Other Sources of Damping

As mentioned in Sec. 3-1-1 damping is the process of energy dissipation that causes a free vibration to decay with time. Damping strongly affects the dynamic amplification in the vicinity of the resonance with the natural frequencies of the structure and especially with the low frequencies that contain more energy. The damping matrix C, as described in Sec. 3-1-1, represents the various damping mechanisms that are present in the structure, which are usually poorly known. In order to compensate for this lack of knowledge, it is common to make assumptions on its form, such as the simplification of the employment of viscous damping as the only present source of damping in the system.

Furthermore, damping is usually the most difficult part to assess of a dynamic analysis and it might also be one of the most important ones, when the structure is excited in regions close to natural frequencies [38]. For this reason and although the model of Rayleigh damping is considered to be in good agreement with experiments, when the damping is small (this is the case for steel structures), the uncertainty related with the real damping values should always be kept in mind when assessing calculated results for a dynamically sensitive structure [5].

The calculation of the coefficients of the Rayleigh damping as described in Sec. 3-1-1 makes use of the modal damping ratios (the damping ratio of each mode), whose values can be estimated for certain applications. In the following sections the two most important sources of damping (aerodynamic and structural) present in offshore wind turbine support structures will be analysed and some less significant damping origins will be mentioned.

**Structural Damping**
According to Madugula [33], structural damping represents the inherent damping properties of the structure due to thermal effects of repeated elastic straining, internal friction and friction of steel connections. More specifically, for welded lattice structures, damping is mainly caused due to some inter-facial friction effect present in the welded joints. In other words, it depends on the fabrication of the joints. Evidently, such a value can be very hard to determine and for this reason it is usually modelled as a viscous damper, which practically is a fraction of the critical damping or damping ratio $\xi$.

Recommended values for structural damping for welded steel structures are usually damping ratios of 1 - 2 % [5], [33], [29] and design standards propose damping ratios less than 3 % [48]. In the developed model the damping ratio of the first mode is required as an input value and here it was set to 1 % of the damping ratio.

**Aerodynamic Damping**
As far as the aerodynamic damping is concerned, it represents the interaction between the motion of the structure and the rotor aerodynamics. When the turbine moves forward (against the wind), the blades experience an increase in total wind speed. As a result of this increased wind speed, the instantaneous tower top load is increased through the basic aerodynamic action of the blades. This load is acting against the tower top motion. The situation is analogous for the backward motion, now resulting in a reduced tower top load, also reducing the tower top motion.

According to van der Tempel [47], Kühn [27] and Salzmann [41] and in contrast with the structural damping, modelling of the aerodynamic damping is a task that can be simulated with less uncertainty and approximate the real effect with sufficient accuracy. The most prominent developed methods that can calculate the aerodynamic damping are the following:

- Garrad method, a closed-form linearization.
- Numerical linearization, based on a state-space analysis.
- Non-linear simulation, a full time domain simulation analysis.

Moreover, one less detailed but still accepted method for modelling the aerodynamic damping is the so-called engineering estimate, which is practically a single value as a fraction of the damping ratio. Proposed value for the engineering estimate is a ratio of 4 %. However, this estimation mainly reflects the values recommended for monopile structures, whereas for more stiff structures as [26] also suggests a lower damping ratio can be regarded, since the higher the natural frequency of the structure, the lower the damping. Hence, for the developed model a value of 3 % was chosen as the engineering estimate for aerodynamic damping.

As a result of the above, the total value for the damping ratio was chosen to be 4 % accounting for the structural and aerodynamic damping. The significance of the damping and especially of the aerodynamic damping will be presented through graphs in the chapters that follow.

**Other Sources of Damping**
Finally, two other sources of damping are the hydrodynamic and the soil damping. The hydrodynamic damping can be understood as the variation of the hydrodynamic drag force

due to the moving structure. For bottom-mounted OWT support structures the structural velocities of the submerged part are very small compared to the water particle velocities and the hydrodynamic damping is much smaller that the structural damping. Thus, it can be neglected. The soil damping can be assumed that is included in the structural damping [29].

### 3-4-5 Derivation of global mass, stiffness and damping matrices

As shortly explained in the first section of this chapter, for the estimation of the natural frequencies and the mode shapes of a structure and therefore for the estimation of its dynamic behaviour, the stiffness, mass and damping characteristics of the structure are required. However, in order to determine those properties for the whole system, first the stiffness, mass and damping properties of the elements that compose it need to be calculated. The common practice in finite element modelling is to derive the above mentioned characteristics for each element and then with appropriate addition the global structure properties can be found.

As explained, in the developed model the 3-D Euler-Bernoulli beam is chosen for the idealization of the framed structure and so the stiffness and mass characteristics of a beam have to be employed. Each element constitutes of two nodes with 6 DOF each, as presented in Sec. 3-1 and as a consequence the stiffness matrix of an element is a 12 by 12 matrix that restricts the movement of each DOF. The stiffness and mass matrices for a beam can be derived with well known methods in the literature and here have been taken from [20] and [39], respectively and can be found in Appendix A.

Having calculated the properties of the individual elements, the assemble of the global mass and stiffness matrices can be found by summing appropriately the element matrices. This summation is performed by adding the nodal related components from the element stiffness (or mass) matrix into the global stiffness (mass) matrix. Thus the size of the global matrices will be 6N by 6N, where N is the number of nodes present in the mesh.

Important here is to mention, that an axis transformation has to be conducted. Due to the local and global axis system presented in Sec. 3-1, for the assembly of the global matrices, first an axis transformation needs to be done, so that the correct DOF in the system are restricted. This transformation can be implemented by using directions cosines between two different axis systems, as shown in the following example.

A vector **V** depicted in Fig. 3-11 can be expressed in terms of components uvw in global system xyz or in terms of components u′v′w′ in local system x′y′z′. Then the components of translation and rotation transform from global to local directions can be calculated as:

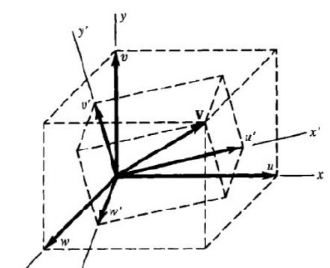

**Figure 3-11:** A vector **V** in local and global axes [16].

$$\begin{aligned} u_1 &= l_1 u_1^{'} + m_1 v_1^{'} + n_1 w_1^{'} \\ \theta_{x1} &= l_1 \theta_{x1}^{'} + m_1 \theta_{y1}^{'} + n_1 \theta_{z1}^{'} \end{aligned} \tag{3-8}$$

where $l_1$, $m_1$ and $n_1$ are the direction cosines.

**Table 3-3:** Direction cosines between two axes.

| | x | y | z |
|---|---|---|---|
| x′ | $l_1$ | $m_1$ | $n_1$ |
| y′ | $l_2$ | $m_2$ | $n_2$ |
| z′ | $l_3$ | $m_3$ | $n_3$ |

Thus, the transformation matrix with which each element should be multiplied is a 12 by 12 matrix given as:

$$\mathbf{T} = \begin{bmatrix} \mathbf{\Lambda} & 0 & 0 & 0 \\ 0 & \mathbf{\Lambda} & 0 & 0 \\ 0 & 0 & \mathbf{\Lambda} & 0 \\ 0 & 0 & 0 & \mathbf{\Lambda} \end{bmatrix} \quad where \quad \mathbf{\Lambda} = \begin{bmatrix} l_1 & m_1 & n_1 \\ l_2 & m_2 & n_2 \\ l_3 & m_3 & n_3 \end{bmatrix}$$

Finally, the global damping matrix is calculated only for the whole system according to Eq. 3-2 and the discussion of Sec. 3-1-1.

## 3-5 Natural Frequencies & Mode Shapes

After the computation of the global mass and stiffness properties of the assembly, the natural frequencies and the mode shapes of the structure can be calculated according to the methodology described in Sec. 3-1-3. It has been stressed already from the previous paragraphs that the modal analysis is a strong indicator of the dynamic behaviour of the structure and for this reason substantial effort will be paid here to understand some properties of the structure and benchmark the results of the developed model with commercial software. Here ANSYS has been selected for the modal analysis comparison and the outcome of this study will generate some important results and conclusions that should be kept in mind for the remaining steps to be implemented for the developed model.

Initially, the influence of the mesh density on the natural frequency and on the mode shape calculation will be assessed only for the developed model and next a comparison of the model with ANSYS will be presented.

### 3-5-1 Influence of the Mesh Density on the Modal Analysis

The mesh density can have an influence on the accuracy of the calculation of the natural frequencies and mode shapes. As mesh density here is meant the number of elements used per member of the structure. It is clear that the more fine the mesh is, the better the estimation of the deformed shape of the structure should be. However, there will also be a significant difference on the computational time required. This can be clearly understood from Table 3-4 and Figures 3-12 and 3-13 that show a great deviation between different mesh densities on the mode shape estimation and a lesser one for the natural frequencies calculation.

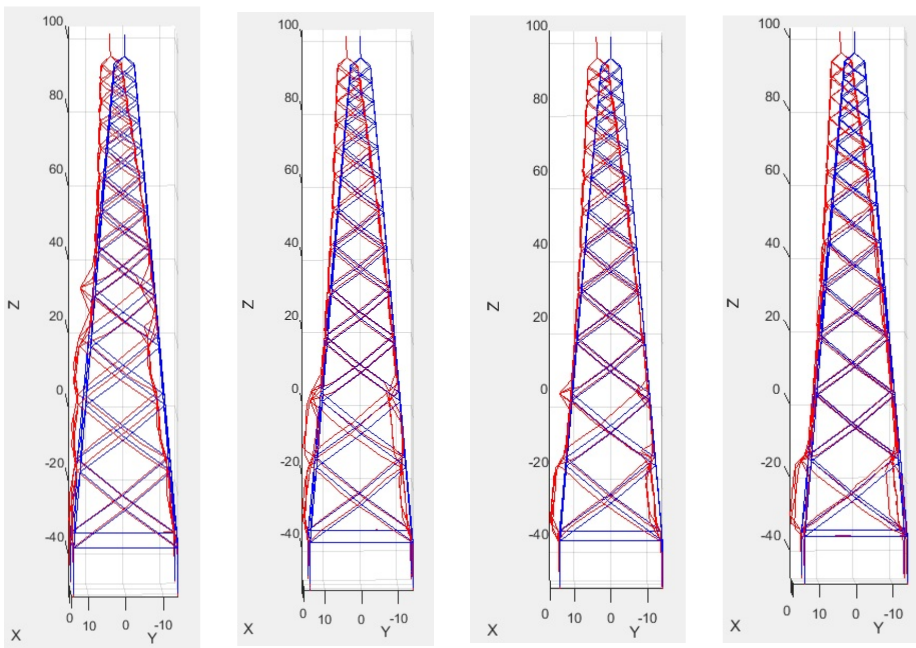


**(a)** 2 elements per member **(b)** 3 elements per member **(c)** 4 elements per member **(d)** 5 elements per member

**Figure 3-12:** Influence of different mesh densities on the mode shape for first bending mode about the x-axis.

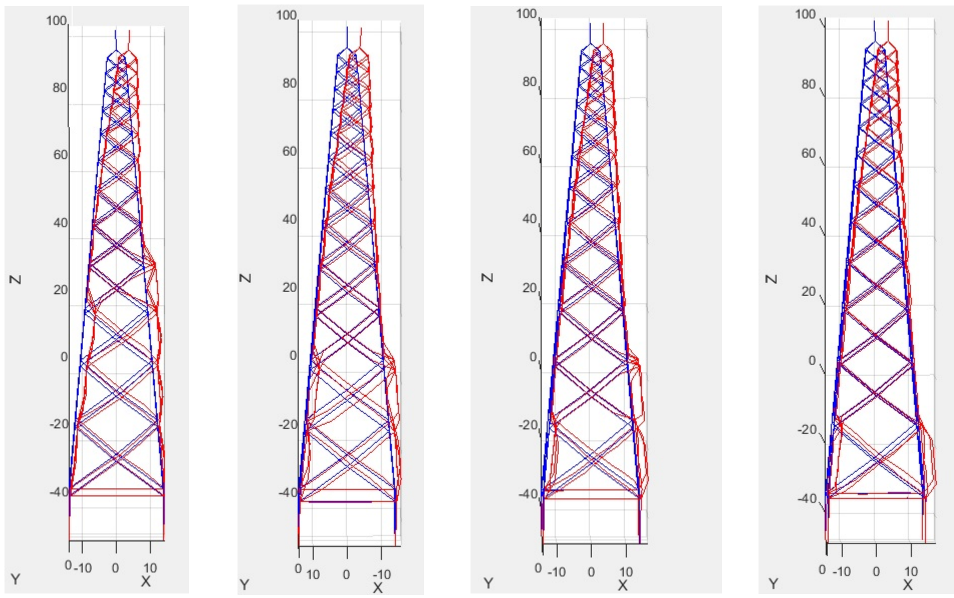

**(a)** 2 elements per member **(b)** 3 elements per member **(c)** 4 elements per member **(d)** 5 elements per member

**Figure 3-13:** Influence of different mesh densities on the mode shape for first bending mode about the y-axis.

**Table 3-4:** Influence of different mesh densities on the calculation of the natural frequencies of the structure and on the required computational time.

| 2 Elements per Member | | 3 Elements per Member | | 4 Elements per Member | | 5 Elements per Member | |
|---|---|---|---|---|---|---|---|
| **Time** | **Frequency [Hz]** | **Time** | **Frequency [Hz]** | **Time** | **Frequency [Hz]** | **Time** | **Frequency [Hz]** |
| **2.8 min.** | 0.7088 | **15.5 min.** | 0.7080 | **48.5 min.** | 0.7077 | **102 min.** | 0.7077 |
| | 0.7088 | | 0.7080 | | 0.7077 | | 0.7077 |
| | 0.7916 | | 0.7916 | | 0.7916 | | 0.7916 |
| | 2.3241 | | 2.3235 | | 2.3234 | | 2.3233 |
| | 2.3242 | | 2.3236 | | 2.3235 | | 2.3234 |
| | 2.9451 | | 2.9444 | | 2.9443 | | 2.9442 |
| | 2.9517 | | 2.9506 | | 2.9503 | | 2.9502 |
| | 2.9663 | | 2.9641 | | 2.9637 | | 2.9636 |
| | 3.2498 | | 3.2469 | | 3.2464 | | 3.2463 |
| | 3.2498 | | 3.2469 | | 3.2465 | | 3.2463 |

Evidently, the number of elements per member used has primarily a significant impact on the estimation of the mode shapes and much less on the calculation of the natural frequencies. An interesting remark on the above figures is how the local effects observed throughout the whole structure for the model with the coarse mesh, start appearing only at the bottom bays of the structure as the mesh gets finer and finally, they appear only as local effects on the legs and braces of the bay closer to the mudline. It is also very important to be noticed the great increment on the required computational time with increasing mesh density. However, for simpler topologies the increase of computational time is not so considerable as presented for the reference structure. As far as the natural frequencies is concerned, it is visible that the number of elements used per member affects to a lesser extent the natural frequency estimation and it has almost no impact on the higher modes.

### 3-5-2 Modal Analysis Verification

After examining the influence of the mesh density on the calculation of the natural frequencies and especially on the mode shapes, here is considered essential to investigate how precise are the above results produced by the developed model. This is achieved by creating the exact same reference model used so far in ANSYS and performing a modal analysis calculation.

With respect to the modeshape estimation, the ones produced by the DM, as presented in Sec. 3-5-1, seem to compare good with the modeshapes as computed by the ANSYS model. The complete comparison can be found in Appendix B and the comparison for the modeshape associated with the natural frequency of bending about the x-axis is also shown in Fig. 3-14. As mentioned, the local deformation effects identified at the braces close to mudline, could probably disappear with the use of a more fine mesh or they could be also caused due to an inconsistency of the model.

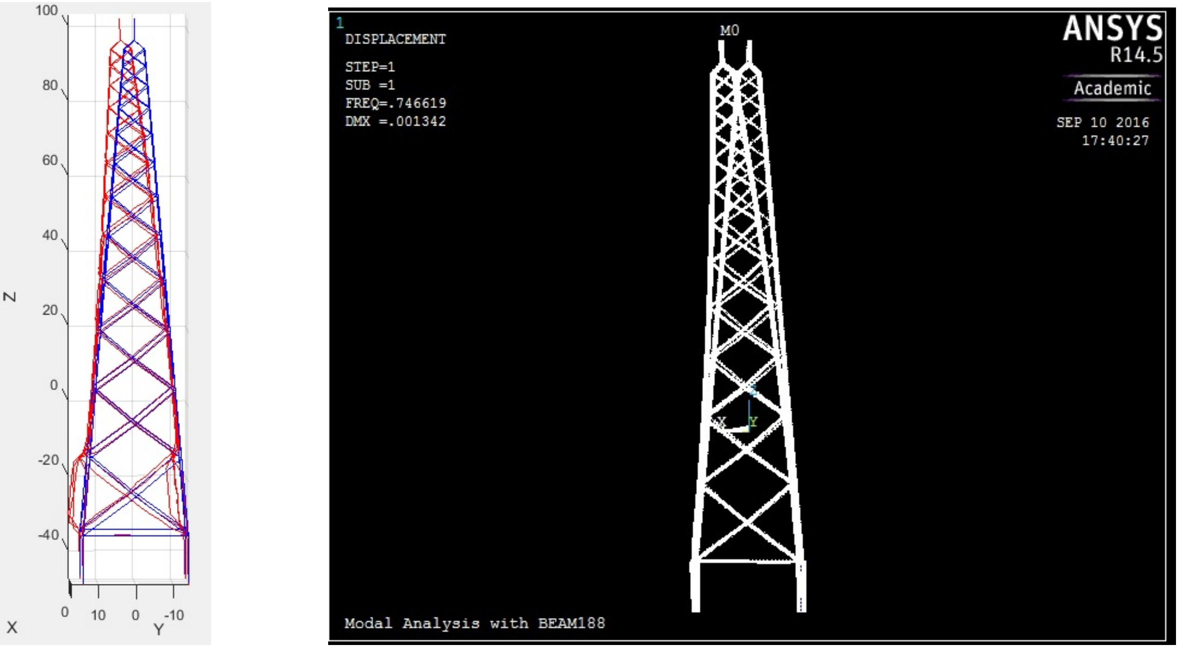


**Figure 3-14:** Comparison of the first modeshape (bending about the x-axis) as calculated by the DM (left) and ANSYS (right).

As far as the natural frequencies is concerned, in Table 3-5 the first ten natural frequencies from the model with the fine mesh (since it is considered more accurate) are presented and compared.

**Table 3-5:** Natural frequency comparison between the developed model and ANSYS.

| Mode | Ansys [Hz] | Developed Model [Hz] | Difference [%] |
|---|---|---|---|
| **1** | 0.7466 | 0.7077 | 5.21 |
| **2** | 0.7467 | 0.7077 | 5.21 |
| **3** | 2.2108 | 0.7916 | 64.19 |
| **4** | 2.3229 | 2.3233 | -0.01 |
| **5** | 2.3252 | 2.3234 | 0.07 |
| **6** | 2.9290 | 2.9442 | -0.52 |
| **7** | 2.9641 | 2.9502 | 0.47 |
| **8** | 3.2560 | 2.9636 | 8.98 |
| **9** | 3.2568 | 3.2463 | 0.32 |
| **10** | 3.3625 | 3.2463 | 3.46 |

From Table 3-5 the following important remarks can be extracted:

1. The first two natural frequencies, associated with the bending about the x and the y axis respectively, as calculated by the developed model show a sufficiently good correlation with ANSYS.
2. The third natural frequency, which is the torsional natural frequency shows a great deviation from the value extracted from ANSYS.
3. All the remaining higher frequencies appear to match perfectly good with error less than 1% apart from the $8^{th}$ and $10^{th}$ frequencies that have a small deviation from the values of ANSYS, but still can be considered sufficient.

Due to the great deviation of the torsional natural frequency from the value calculated by ANSYS, it is important to analyse in greater detail the source of this divergence. One possible explanation could be that the difference lies in the type of elements used by the two models. In the developed model, as stated in the previous paragraphs, the element used is Euler-Bernoulli beam, which neglects shear deformations, whereas ANSYS uses Timoshenko beams. This means that an investigation needs to be performed on the developed model, to examine the validity of the assumption that the torsional stiffness at an element level could have such a big impact on the torsional stiffness of the whole system and consequently affecting the calculation of the torsional natural frequency.

For this purpose, a sensitivity study is carried out. By changing the shear modulus and performing a modal analysis on the developed model, the difference of the resulting natural frequencies is presented and compared in Table 3-6.

From Table 3-6 becomes evident that the shear modulus has a significant influence on the calculation of the natural frequencies. What is interesting to be noticed, is that the influence on the frequencies associated with the bending and higher modes is not so extreme as it is for the coloured cells, which represent the torsional natural frequency of the structure, with respect to the normal shear modulus value ($G = 81e9Pa$). This can be understood by examining the pattern that the bending and higher order natural frequencies follow. The pattern

**Table 3-6:** Sensitivity analysis of shear modulus on the natural frequency calculation (The highlighted values represent the torsional frequency).

| Mode | G=81e8 Pa | Normal Value G=81e9 Pa | G=81e10 Pa | G=81e11 Pa |
|---|---|---|---|---|
| **1** | 0.2611 | 0.7088 | 0.7093 | 0.7113 |
| **2** | 0.7086 | 0.7088 | 0.7093 | 0.7113 |
| **3** | 0.7086 | 0.7916 | 1.8732 | 2.3942 |
| **4** | 2.2860 | 2.3241 | 2.3503 | 2.3943 |
| **5** | 2.2912 | 2.3241 | 2.3504 | 3.1080 |
| **6** | 2.2913 | 2.9451 | 3.3083 | 3.3781 |
| **7** | 2.8521 | 2.9517 | 3.3376 | 3.3782 |
| **8** | 2.8975 | 2.9663 | 3.3517 | 3.3828 |
| **9** | 3.0029 | 3.2498 | 3.3520 | 3.3837 |
| **10** | 3.0032 | 3.2498 | 3.3579 | 3.7980 |

is that they always go in pairs of two, which means that every two values the frequencies are equal or close to equal (and this is also the case for the results as calculated by ANSYS), whereas the torsional frequency is greatly affected by the shear modulus. The paired frequencies result due to the symmetry of the structure. It is understandable that the bending about the x-axis will be very similar to the bending about the y-axis and this holds also for the rest of the higher modes. Certainly, all the frequencies are affected by this sensitivity study, but not as significantly as the torsional frequency. Finally, the step change of the shear modulus is chosen to be quite extreme in order for its effect to be easily more visible.

Conclusively, this study assures the assumption made above, that the type of element selected, greatly affects the dynamic behaviour of the structure with respect to torsion. More importantly, it shows that the particular model will most probably not generate accurately enough results for structures where torsion plays a significant impact and for this reason further investigation needs to be performed on this topic.

# Chapter 4

# Modelling of Load Inputs (Wind & Waves)

Having analysed extensively in Chapter 3 the first stage of the algorithm presented in Fig. 2-1, it is now time to consider the second step of the methodology, which concerns the modelling of random environmental conditions and the loading that is experienced by an offshore wind turbine lattice structure. Since the primary goal of the developed model is a preliminary fatigue damage calculation, the only relevant environmental conditions that are examined here are the wind and the wave spectra, and the loading exerted due to currents can be safely neglected according to [4].

The analysis of structures subjected to environmental loading inevitably requires statistical calculations, if only to interpret the basic environmental data that will be presented in statistical form. Wind and wave loading analysis for a dynamic problem make use of essential statistical characteristics. Although both processes are random and non-stationary, since their mean value changes over time, they are modelled as such by choosing small record lengths, where the mean value effectively is constant. Throughout this and the next chapter there will be a broad reference on statistical terms and the reader is advised to make use of some related literature, if necessary. For the sake of simplicity and in order not to lose focus from the major aspects of this assignment there will be no explanation of this terminology in the context of this thesis.

In the subsequent sections an elaborated review of how the wind and the wave loading are simulated in the developed model will be presented and attention will be paid on the methodology followed for their application on the structure.

## 4-1 Wind Loading

This paragraph serves the purpose of providing relevant information about the common practices for the wind modelling followed by the methodology adopted in the developed model for the derivation of the wind load spectrum. For the representation of the wind characteristics there has to be initially a distinction between normal and extreme conditions. Since this thesis is concerned with fatigue calculations alone, only the normal wind characteristics will be explained in the following sections and for a more detailed content the reader can refer to textbooks [34], [48].

### 4-1-1 Wind Speed, Shear & Turbulence

The normal wind conditions are specified in terms of air density, a long-term distribution of the 10-minute mean wind speed, a wind shear and turbulence. The 10-minute wind speed $U_{10}$ is considered to be constant over a short period, i.e. 10 minutes [48]. Furthermore, wind speed data is height dependant with the mean wind speed at the hub height being used as reference. The wind speed at different heights can be calculated, while taking into account the mean wind speed at hub height and the wind speed profile above the still water level.

By wind speed profile is meant the vertical speed distribution that the wind experiences due to the earth's surface friction. This effect is known as wind shear; it takes place in the atmospheric boundary layer and a visual representation is shown in Fig. 4-1. To describe the wind shear effect on the mean wind speed at a certain elevation, two main models are commonly used, the logarithmic and the power law profile. In this thesis the power law profile is used, which calculates the wind speed at an elevation height above the still water level according to Eq. 4-1 [47]:

$$U_w(z) = U_{w,r} \left( \frac{z}{z_r} \right)^{\alpha} \tag{4-1}$$

Where $U_{w,r}$ is the wind speed at the reference height, $z_r$ is the reference height and $\alpha$ is the power law exponent.

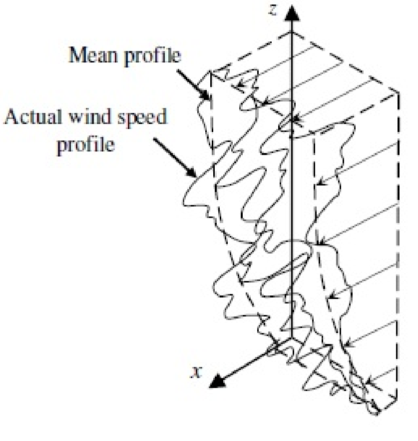


**Figure 4-1:** The effect of wind shear due to friction with the earth's surface [47].

Finally, the term "turbulence" denotes random variations in the wind velocity from 10 minute averages and it includes three vector components, namely the longitudinal, the lateral and the upward that define the wind speed profile along the direction of the mean wind velocity, horizontally to the longitudinal direction and normal to both the lateral and the longitudinal directions, respectively [15]. The mean wind speed and the standard deviation ($\sigma_u$) of a 10-minute turbulent wind profile can be regarded as constant.

One of the most important measures of turbulence is the turbulence intensity, that is dependent on the height and the roughness of the terrain and is given by Eq. 4-2:

$$TI = \frac{\sigma_u}{U} \tag{4-2}$$

### 4-1-2 Wind Spectrum Modelling

Turbulence can also be represented in the form of spectral density, which shows how the energy of the wind turbulence is distributed between different frequencies. The most commonly used spectra are the von Karman and Kaimal spectrum. In the context of this thesis and as it is also suggested from the standards [48], the Kaimal spectrum will be used as input, which is more suitable to model the atmospheric boundary layer and can be calculated from Eq. 4-3:

$$S_{Kaimal}(f) = \frac{\sigma_u^2 4L_v/U}{(1+6fL_v/U)^{(5/3)}} \tag{4-3}$$

where $f$ is the frequency in $[Hz]$ and $L_v$ is the integral length scale. An example of a Kaimal spectrum is also presented in Fig. 4-2.

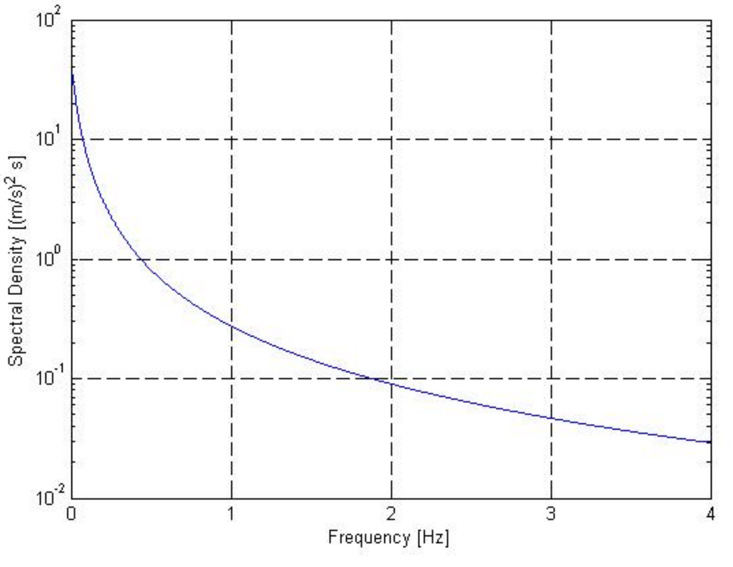


**Figure 4-2:** Kaimal spectrum at $U = 12m/s$ and $TI = 0.15$.

## 4-2 Wind Load Spectrum in the Developed Model

One common practise of deriving the wind load spectrum for a wind turbine in the FD is by translating the thrust force exerted on the rotor (through the well known equation shown in 4-4) into a Power Spectral Density (PSD) and multiplying it with the Kaimal spectrum. This method is fairly simple and does not take into account any of the non-linear behaviour of the wind turbine present in different wind conditions,

$$T = \frac{C_T \rho_a A}{2} U^2 \tag{4-4}$$

For a more detailed analysis and according to van der Tempel [47] some form of time domain simulation is required in order to solve the blade element momentum equations and calculate the tower top load. Here this methodology is also employed.

With the utilization of a time domain simulation software for wind turbines - in this thesis the commercial software GH Bladed was used - timeseries of tower top load for a turbine computer model can be calculated for specific wind conditions, described by a mean wind speed, turbulence intensity and wind shear. By applying the Fast Fourier Transformation (FFT) on those timeseries, the PSD of the thrust force for example can be derived. Van der Tempel argues that the calculation of the spectrum of only the thrust force exerted on the turbine yields sufficient results for the derivation of the tower top load. In contrast with this methodology and due to the different type of structure considered in the context of this thesis (instead of a monopile as in van der Tempel's work), there is the necessity for the PSD calculation of the torsional moment as well. This is in accordance with [5], [29] and [30], where they argue that lattice structures (and especially the 3-leg type) are sensitive to torsion driven loads and moments and must be assessed sufficiently.

Furthermore, the tower drag is excluded from this analysis, due to its small contribution when compared to the thrust and torsion exerted on the Rotor Nacelle Assembly (RNA). Conclusively, after performing time domain simulations the thrust force and the torsional moment timeseries exerted on the RNA need to be extracted and transformed into PSDs. These random excitation inputs are considered as stationary and discrete loadings. According to Clough and Penzien [14], apart from the power spectral densities of those inputs, also the Cross Spectral Densities (CSD) that contain information about the relationship between the amplitudes of the same frequencies in the two signals need to be considered. Thus, in the remaining of this report, wherever there is a reference to tower top load it will be meant the PSDs and CSDs of the thrust force and the torsional moment exerted on the RNA.

Finally and before analysing some technical aspects of the FFT procedure, is important to mention here that the above TD simulations are performed without incorporating any tower modes, which means that the support structure is modelled as rigid. This makes the PSDs calculated for a specific turbine model applicable to any kind of support structure of similar type to the one used for the simulations (for example jackets with similar structural configuration). The argument that the calculated PSDs are applicable only for similar structures with the one modelled in the simulations holds true, because although the tower modes are not included in the simulations, the tower and the turbine are not fully uncoupled. In this sense, the engineer has the possibility to run the TD simulations only once and use this input tower top load for several tower designs in order to examine different response characteristics.

However, following this modelling approach the aerodynamic damping is not considered in the output result, since the motion of the structure is restricted. For this reason, the effect of the aerodynamic damping has to be re-introduced in the overall total damping of the system and this will be analysed in Chapter 5.

### 4-2-1 FFT of Input Loading Signals

The PSDs are calculated with the use of the Fast Fourier Transform algorithm applied to the timeseries of thrust force and torsional moment and employing a Hanning window method of 50%, in order to arrive at a smoother PSD output. An example of the PSD of the torsional moment as calculated by time domain simulations (shown in Fig. 4-3), is presented in Fig. 4-4. It is noticeable that the output signal still contains a significant amount of noise, due to the small number of simulations used. Within the context of this thesis a number of 3 TD simulations with a length of 600 seconds each were used, similar to the one shown in Fig. 4-3 and their related spectra were averaged in order to create a smoother spectrum output. In contrast, van der Tempel argues that at least a minimum amount of 50 simulations (by applying also a 50% window technique) should be subjected to FFT, so that the results could be considered statistically reliable and in order for the output signal not to contain any noise.

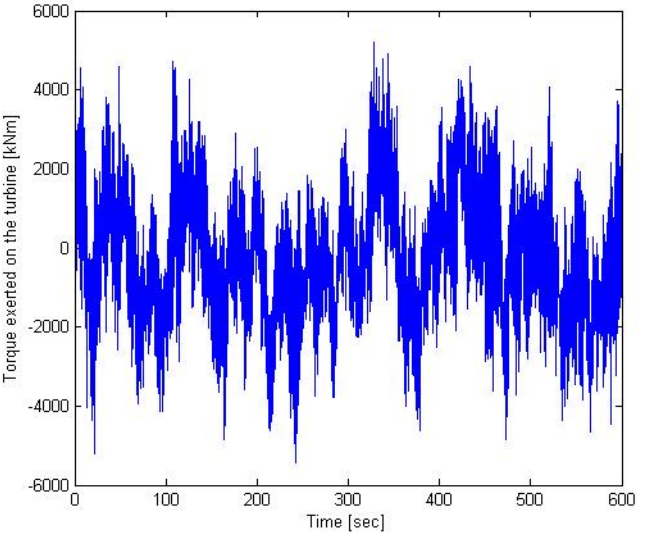


**Figure 4-3:** Torque exerted on the NREL turbine at 14 m/sec (extracted from GH Bladed).

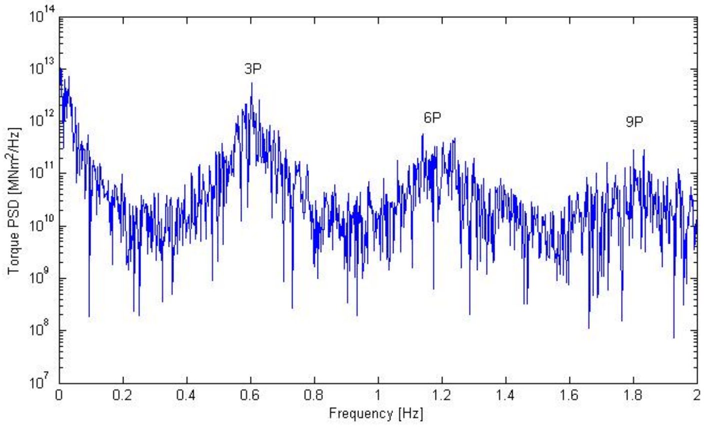


**Figure 4-4:** PSD of torque load on the NREL turbine at 14 m/sec.

From the two graphs in Fig. 4-3 and 4-4 it becomes evident that the FD representation has a superiority over the TD figure with respect to the relevant information that can be extracted for the turbine. This conclusion is supported, since one can clearly identify the three peaks present in Fig. 4-4, which represent the 3P, 6P and 9P rotational sampling frequencies of the 5MW NREL wind turbine. Interesting is also here that the 1P sampling frequency is not visible at the graph. This probably originates from the fact that the model used for the Bladed simulations might have been incomplete in terms of mass imbalances on the blades or aerodynamic imbalances that are the main source of 1P loading. In the next section, the methodology employed in this thesis for the modelling of the wave input loading will be presented.

## 4-3 Wave Loading

The second environmental parameter that has to be modelled and is also a design driver for offshore lattice structures is the sea state, which in this case is mostly defined by the waves. Similarly with the wind load modelling, here a proper methodology for implementing the wave loading has to be derived and integrated in the developed model. In the subsequent sections, a small theoretical introduction of the basic wave theories and kinematics will be presented followed by the wave spectrum modelling and the hydrodynamic loading and the incorporated method of the wave load spectrum derivation in the developed model.

### 4-3-1 Wave Theories & Kinematics

For the correct representation of a sea state, three parameters need to be defined and a wave model that describes the wave theory and kinematics has to be selected. The variables that define a wave climate according to the standards are the significant wave height ($H_s$), which is defined as the 1/3 of the maximum amplitude of the wave, the spectral peak period ($T_p$), which is associated with the mean zero crossing period ($T_z$), and the water depth. Those values are assumed to be constant for a stationary wave condition, which in a short term can be regarded as a 3-hour or 6-hour period.

There are numerous wave theories that have been developed, which are applicable to specific environmental conditions. The majority of those theories assume a flat bottom and have a constant uniform depth. Unlike the real random ocean waves, all the theories assume periodic and uniform waves [11].

Some of the most commonly used theories in the offshore industry are the linear wave theory or Airy theory, Stokes wave theories for high waves, stream function theories, based on numerical methods, Boussinesq higher-order theories, etc. and they should be selected for each site according to water depth, the wave height and the wave period as depicted in Fig. 4-6. The simplest and widely used wave theory is the Airy wave theory, which is also employed in this thesis, since intermediate and deep water depths are considered and not extreme wave heights, since fatigue loads are examined. However, one limitation connected with this theory is that the kinematics are calculated up to still water level and cannot be described in the wave top.

The horizontal water particle kinematics (velocity and acceleration) according to Airy theory can be calculated from Equations 4-5:

$$
\begin{aligned}
u(x,z,t) &= \frac{H_s}{2} 2\pi f \frac{cosh(k(z+d))}{sinh(kd)} cos(kx - 2\pi f t) \\
\dot{u}(x,z,t) &= \frac{H_s}{2} (2\pi f)^2 \frac{cosh(k(z+d))}{sinh(kd)} sin(kx - 2\pi f t)
\end{aligned}
\tag{4-5}
$$

where d is the water depth, z is the particle horizontal position ($-d < 0 < z$), f is the corresponding frequency and k is the wave number defined by the wavelength ($\lambda$) with equation $k = \frac{2\pi}{\lambda}$. The above mentioned characteristics for a regular wave are depicted in Fig. 4-5.

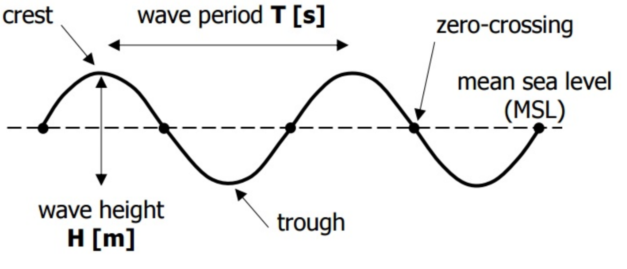


**Figure 4-5:** Definition sketch of a progressive regular wave.

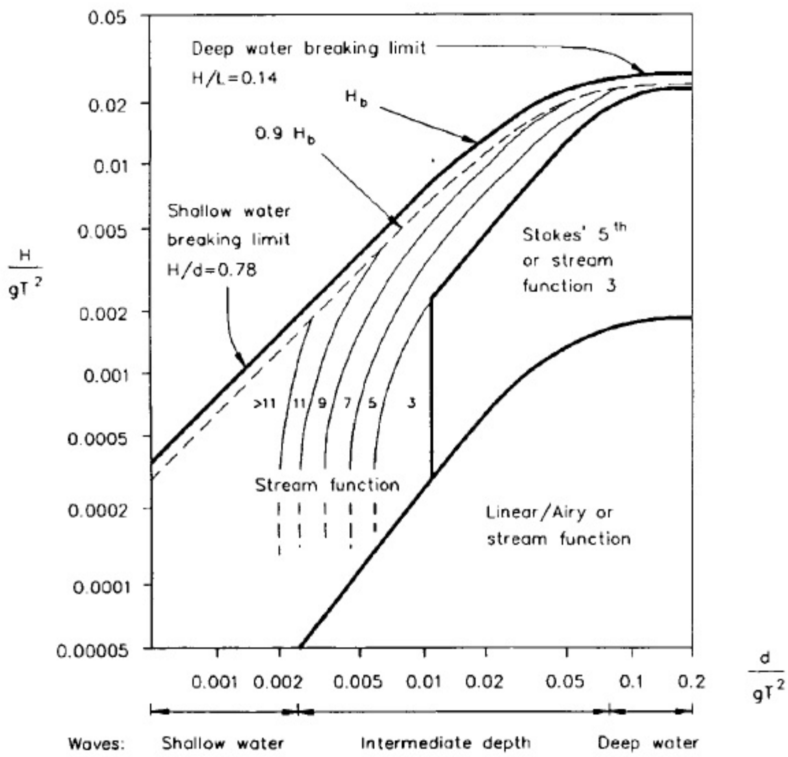


**Figure 4-6:** Regions of applicability of different wave theories [27].

## 4-3-2 Wave Surface Elevation Spectra

A very useful method of representing the water surface is by summing a large amount of regular sinusoidal waves with various amplitude phases and periods and superimpose each one on the other. This method has been found to be particularly useful for the analysis of the dynamic response of offshore structures [5]. The most general and frequently used spectra in the offshore sector is the Pierson-Moskowitz with a more specific and improved version of it being the JONSWAP spectra, which is based on measurements on the North Sea. Since, in the context of this thesis a site in the Dutch coastline is considered, the latter spectra is used in the developed model. The JONSWAP spectrum (an example of its form is depicted in Figure 4-7), can be calculated for a specific sea state from Equation 4-6:

$$S_J(f) = \frac{\alpha_J g^2}{(2\pi)^4} f^{-5} exp(-\frac{5}{4}(\frac{f}{f_p})^{-4}\gamma)^{\beta} \tag{4-6}$$

where $S_J(f)$ is the spectral density, $f_p$ is the peak frequency, $\gamma$ is the peak enhancement factor, which has a typical value of 3.3 for a fully developed sea according to van der Tempel and the values for the parameters, $\alpha_J$, $\beta$ and $\sigma$ can be calculated from Equations 4-7, 4-8 and 4-9 respectively:

$$\alpha_J = 5\frac{H_s^2 f_p^4}{g}(1 - 0.287 ln\gamma)\pi^4 \tag{4-7}$$

$$\beta = exp\left[-0.5\left(\frac{f-f_p}{\sigma f_p}\right)^2\right] \tag{4-8}$$

$$\sigma = \begin{cases} 0.07, & f \leq f_p \\ 0.09, & f > f_p \end{cases} \tag{4-9}$$

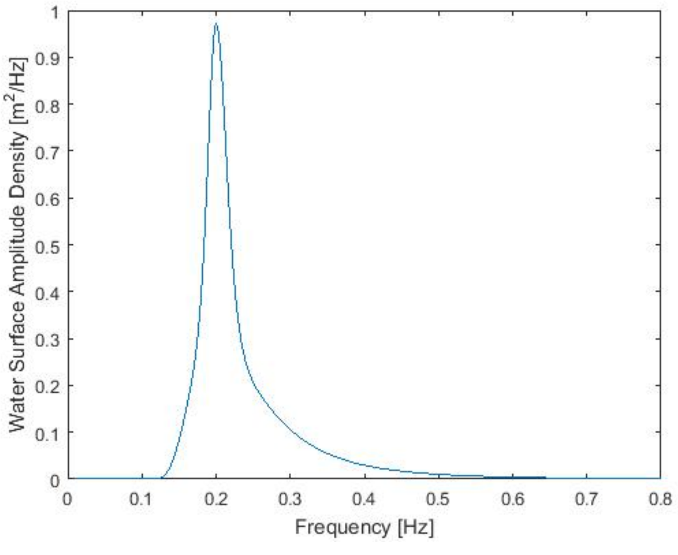


**Figure 4-7:** JONSWAP spectral density for $H_s = 1$ m and $T_p = 5$ s.

### 4-3-3 Hydrodynamic Loading

As most commonly used in the offshore industry and as it is also suggested by the standards [48] for the calculation of wave loading on slender structures, such as jackets or generally framed structures, Morison's equation should be applied. Morison's equation includes two terms, namely the drag and the inertia term and is given by Equation 4-10:

$$\begin{aligned} f_M(x,z,t) &= f_D(x,z,t) + f_I(x,z,t) \\ f_D(x,z,t) &= c_D\frac{1}{2}\rho_{water}D|u(x,z,t)|u(x,z,t) \\ f_I(x,z,t) &= c_M\frac{1}{4}\rho_{water}\pi D^2\dot{u}(x,z,t) \end{aligned} \tag{4-10}$$

Where $f_D(x,z,t)$ and $f_I(x,z,t)$ are the drag and the inertia force components of the total hydrodynamic force exerted on the submerged parts of the structure and $c_D$ and $c_M$ are the drag and the inertia coefficients respectively. The terms $u(x,z,t)$ and $\dot{u}(x,z,t)$ are the water particle velocity and acceleration, as calculated by Eq. 4-5.

A common practice for monopile structures for simplification purposes, is to neglect the drag term during the fatigue calculation of the hydrodynamic loading. This is an acceptable simplification, since the wave loading on structures with large diameters ($D > 4m$) is mainly inertia dominated [47], [42] and this can be also determined by examining the value of the Keulegan-Carpenter (KC) number defined by Equation 4-11. If the KC number has a value smaller than 5 then according to Henderson [24] the drag force component can be ignored. However, this is not the case for jacket or lattice structures, due to the smaller diameters in comparison with monopiles. Hence, both force terms need to be taken into account.

In the subsequent section a detailed analysis will be presented with the purpose of examining how the above described common practises can be implemented for the modelling of the hydrodynamic loading for the developed model.

$$KC = \frac{uT_p}{D} \tag{4-11}$$

## 4-4 Wave Load Spectrum in the Developed Model

The wave theories and hydrodynamic loading model described above, provide a basis for examining the selected practice applied in the developed model for calculating the wave force spectrum input on the lattice structure. According to the introduction of the previous paragraphs, it should be clear by now that the calculation of wave loads on structures consists of the following two steps, visualized also in Fig. 4-8:

1. Determining the water kinematics (velocity & acceleration).
2. Calculating the load on the structure.

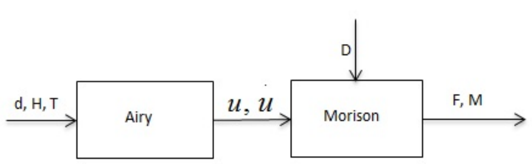


**Figure 4-8:** Steps for the determination of the hydrodynamic forces and moments (Symbol d is used for the water depth).

While for a monopile this procedure might be straightforward, this is not the case for jacket or lattice type structures. This is due to the fact that Morison's equation can be applied only on structures that lie perpendicular to the direction of the wave, so on horizontal structures. Thus, in the case of space frame type of structures in order to calculate the hydrodynamic forces, first the relative angle between each inclined member and the wave needs to be calculated. Nonetheless, in the scope of this thesis with the objective being the reduction of the model complexity, a different common practice was chosen to be followed. The employed procedure was proposed by Vugts [51] and is explained in greater detail in the subsequent paragraph.

Furthermore, another aspect to be considered for jackets, is the possibility of different members of the structure being affected by the same wave at different times (with a phase shift), so with different wave characteristics. This could be the case for jackets with wide base and should be taken into account. This topic will also be addressed in the subsequent sections.

### 4-4-1 Equivalent Diameter Model

The basic concept of the methodology of the equivalent diameter model is that all the submerged members (legs and braces) of a space frame structure can be represented by an assembly of vertically stacked tubes aligned with the centre of the structure, as depicted in Figure 4-9. In this way the submerged bays can be transformed into an equivalent diameter monopile. It is obvious that the assumption that all the members are placed at the centre of the structure neglects effects of spatial separation, but according to Vugts this approach results in a more conservative load estimation. Furthermore, the validity of this assumption in terms of wave phase shift change has to be investigated and this is perform in the end of the current paragraph.

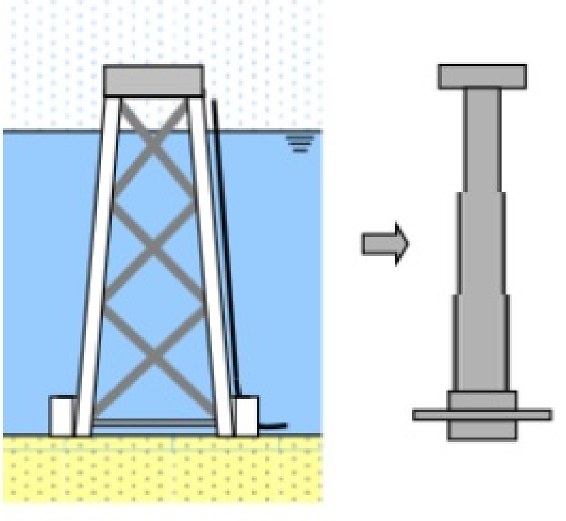

**Figure 4-9:** Equivalent diameter model [32].

Having determined the equivalent diameters of all the relevant individual members, with respect to Table 4-1, it is possible now to combine those into an equivalent "Drag stick" and an equivalent "Inertia stick", as it is shown in Equations 4-12 and 4-13 and perform the Morison load calculations.

**Table 4-1:** Equivalent diameters for any type of inclined member. $\theta_{br}$ is the angle between of inclined member with the horizontal plane.

| Member Orientation | Parallel to Wave Propagation Direction | | Normal to Wave Propagation Direction | |
|---|---|---|---|---|
| | **Drag** | **Inertia** | **Drag** | **Inertia** |
| **Vertical** | $D_{eq} = D$ | $D_{eq} = D$ | $D_{eq} = D$ | $D_{eq} = D$ |
| **Horizontal** | 0 | 0 | $D_{eq} = L$ | $D_{eq} = \sqrt{DL}$ |
| **Inclined** | $D_{eq} = D$ | $D_{eq} = D$ | $D_{eq} = \frac{D}{sin(\theta_{br})}$ | $D_{eq} = \frac{D}{\sqrt{sin(\theta_{br})}}$ |

$$D_{eq,D,tot} = \sum_{i=1}^{n} D_{D,eq,i} \tag{4-12}$$

$$D_{eq,I,tot} = \sqrt{\sum_{i=1}^{n} D_{I,eq,i}^2} \tag{4-13}$$

**Phase Shift Inquiry**

As mentioned, one necessary investigation that has to be performed for space frame structures while examining the wave loading is whether or not there is a phase shift as the wave propagates between the first leg and the second leg located perpendicularly to the wave. This is not a problem for monopiles, but for jacket structures the engineer has to compare the wavelength with the base width of the structure and adjust the load calculations, if necessary.

From Figure 4-10, becomes clear that for structures with a base width larger than $25m$ the assumption that the whole structure is experiencing a loading from the "same" wave is sufficient, since the maximum energy of a wave is located in the region of $0.2 - 0.25$ Hz, as it is also presented in the example of Fig. 4-7. Hence, the simplification of the equivalent diameter model is acceptable for the calculation of the hydrodynamic loading in the DM.

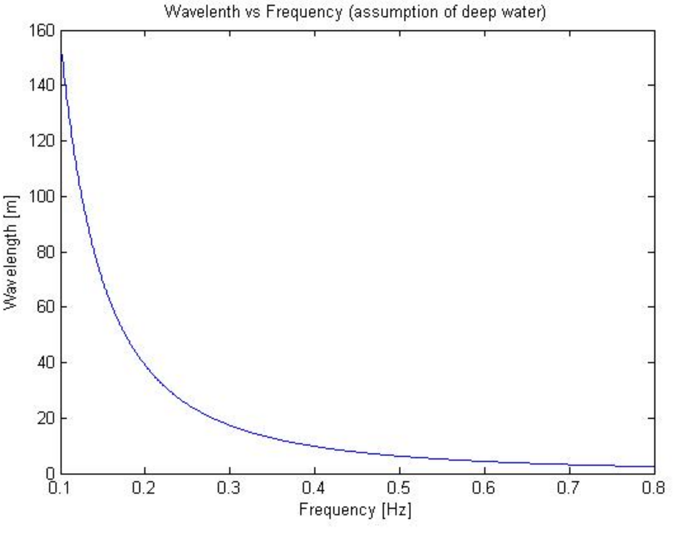


**Figure 4-10:** Wavelength versus frequency with the assumption of deep water.

### 4-4-2 Application of Hydrodynamic Load Spectrum

In this section the methodology of applying the computed load spectrum on the structure is described. Although the approach of relating the lattice structure to an equivalent diameter model has been explained, the application of the Morison equation deviates from the one followed in the monopile structures. The applied methodology for a monopile would be the integration of the total force (or preferably total moment) of the waves exerted on the structure and then the translation of it into a mudline bending moment or mudline spectrum, since the algorithm is developed in the FD.

However, the current type of examined structure requires the adaptation of a different approach. It is important to keep in mind, that the equivalent diameter model serves only as an assisting representation of the real structure in order to make the load computation easier. This means that the calculated load spectrum is applied on the model of the lattice structure and not on the equivalent diameter model. Thus, topic of this paragraph is the explanation of the load distribution on the space frame in order to determine the individual member loads.

In reality, a wave exerts its force on all the submerged members of the structure simultaneously. Here effort has been made to follow a methodology close to this scenario. The idea is that initially the wave load (force and induced moment) is integrated analytically per bay and the application point of the wave force is derived. Next, the total force per bay is partitioned into two force components with respect to the application point and they are applied at the top and bottom of the respective bay. For bays with common points - that is two bays that are on top of each other, they have a common point, the top of the one coincides with the bottom of the other - the force components are added. Finally and returning now to the original lattice structure model, the force components that have been calculated for each section are equally divided into the number of legs and applied at the nodes of the legs at the height of each bay. This methodology can be better understood in the flowchart of Fig. 4-11. Furthermore, it is also visible that after the calculation of the application point, the calculation proceeds in terms of force spectrum and this is implemented also in the DM.

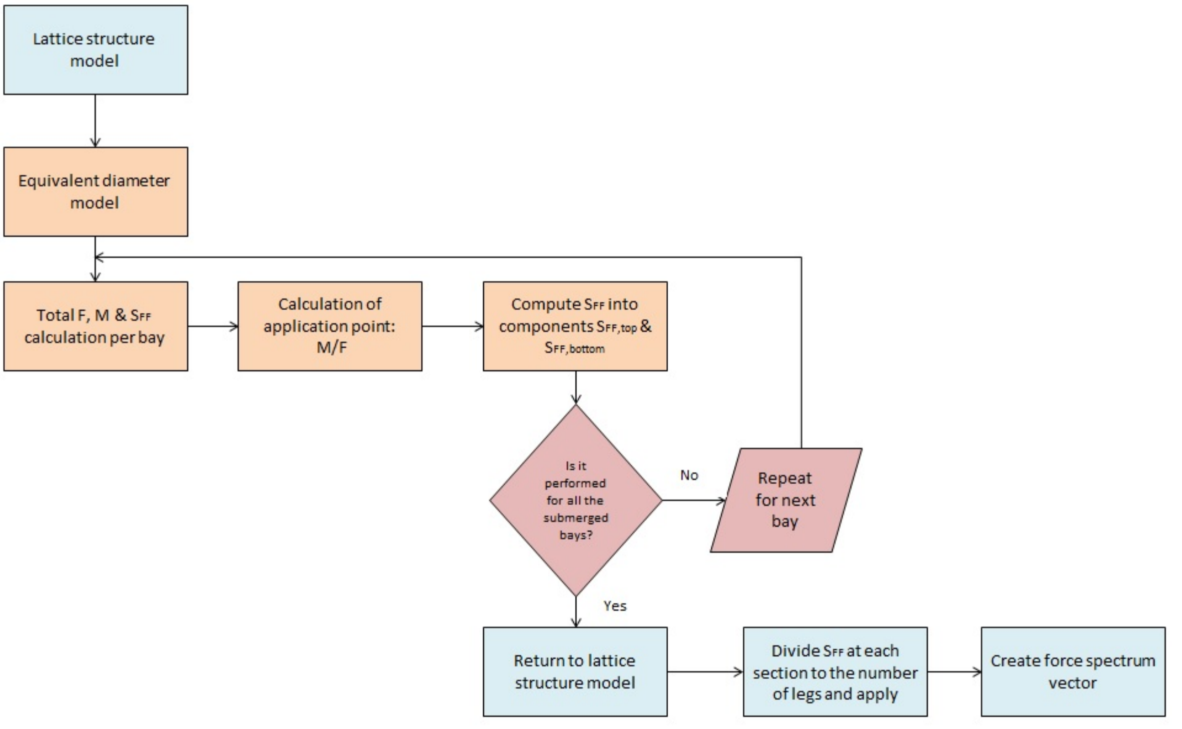


**Figure 4-11:** Procedure of wave load spectrum application on the lattice structure model.

The final result is a vector containing the force spectrum applied simultaneously at the nodes of the submerged legs. For example, a structure with two submerged bays and four legs will have a vector containing 12 components; 4 equal spectra applied at the nodes of the legs located at the bottom of the first bay (i.e. the mudline), 4 spectra applied at the nodes of the legs located at the top of the first bay (that coincides with the bottom of the second bay) and 4 wave spectra applied at the nodes of the legs located at the top of the second bay. This can also be visualized in Figure 4-12. In this figure only the decomposition of the total calculated wave spectrum acting on a bay into the subcomponents applied on the legs is shown.

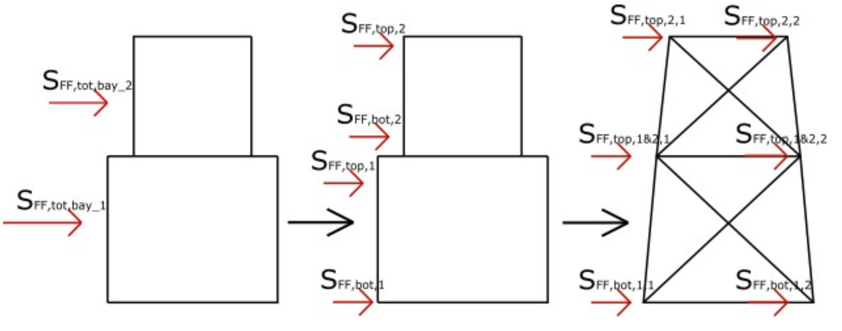


**Figure 4-12:** Decomposition of the calculated wave spectrum for a bay into its components applied on the legs.

### 4-4-3 Load Spectrum Calculation

After the explanation of the procedure followed in the DM for the wave spectrum application, in this section the computations taking place for the derivation of the load spectrum are presented. As already shortly mentioned above, the analytical solutions for the wave force and moment (in order to find the application point for each bay for the applied force) as well as the analytical solution for the wave force spectrum need to be computed.

All the calculations are based on Morison's equation, Eq. 4-10, and on the Airy linear wave theory, Eq. 4-5, and on the procedure described by Fig. 4-8. Regarding the calculation of the wave particle kinematics and since the calculations are performed in the FD, the information used are the magnitudes of the particle speed and acceleration and the phase difference between those two is neglected. This is very important, since from Morison's equations it becomes obvious that the total hydrodynamic loading is the addition of drag and inertia forces, which depend on the velocity and the acceleration component, respectively. In reality the maximum values of those two forces are out of phase and do not occur at the same time. However, by neglecting the phase difference between velocity and acceleration, the calculation of the total wave force becomes more conservative and this should be kept in mind for the final result.

Another key point that requires attention is the fact that the drag term in Morison's equation introduces a non-linearity in the system, which has to be resolved. As concluded in Section 4-3-3, both terms (drag and inertia) need to be taken into account for lattice structures. So, the issue of linearisation of the drag term is described below.

**Linearisation of the Drag Term in Morison's Equation**
Approximations for the linearisation of the square of the speed term in the drag component of Morison's equation have been proposed by several researchers [8], [46], [3], with each proposal more applicable in different conditions and structures. In this thesis Borgman's linearisation [8] was employed and its basic principal is that the square of the velocity can be approximated by Equations 4-14 and 4-15:

$$u|u| \simeq \sqrt{8/\pi}\sigma_u u \tag{4-14}$$

where,

$$\sigma_u = \sqrt{2\int_0^{2\pi} \frac{(2\pi f)^2 cosh^2 kz}{sinh^2 kz} S_J(f) df} \tag{4-15}$$

After the linearisation of the drag term, now the analytical solutions for force, moment and force spectrum moments for the waves per bay can be derived.

**Analytical Solutions for Wave Loading**
Having as starting point Equations 4-10 and making use of the linearisation technique as described above and integrating from the bottom of each bay until the top of the bay, the resulting analytical solutions for inertia and drag force components are given by Equations 4-16 and 4-17:

$$F_I = \frac{C_m g}{sinhkd}\left(sinh[k(z+d)]\right)\Big|_a^b \tag{4-16}$$

$$F_D = \frac{C_d\sqrt{gk}\sigma_u}{ksinhkd}\left(sinh[k(z+d)]\right)\Big|_a^b \tag{4-17}$$

where $a$ and $b$ are the integration points (top and bottom height of each bay), $d$ is the water depth, $k$ is the wave number given by the dispersion relation in Eq. 4-20 (with the assumption of deep water) and $C_m$, $C_d$ are given by Eq. 4-18 and 4-19, respectively.

$$C_m = \frac{c_m \rho \pi D^2 \zeta}{4} \tag{4-18}$$

$$C_d = \frac{c_d \rho D \zeta}{2} \tag{4-19}$$

where $\zeta$ is the wave amplitude, which equals $H_s/2$ and $c_m$ and $c_d$ are the inertia and drag coefficients, respectively.

$$2\pi f = \sqrt{gk} \tag{4-20}$$

In a similar way and making use of the relation $M = cF$, where $c$ is the point with respect to which the moment induced by the wave force is applied, the moments exerted per bay can be also analytically calculated and are given in Eq. 4-21 and 4-22:

$$M_I = -aF_I + \frac{C_m g}{sinhkd}\left(zsinh[k(z+d)] - \frac{1}{k}cosh[k(z+d)]\right)\Big|_a^b \tag{4-21}$$

$$M_D = -aF_D + \frac{C_d\sqrt{gk}\sigma_u}{ksinhkd}\left(zsinh[k(z+d)] - \frac{1}{k}cosh[k(z+d)]\right)\Big|_a^b \tag{4-22}$$

Having found now both the total force and total moment exerted on each bay, then the calculation of the application point is fairly straightforward. The calculation of the application point is required only for the partition of the total wave force spectrum of each bay into top and bottom force spectra as described in Sec. 4-4-2. The analytical calculation of the wave force spectrum is given by Equation 4-23 and the result comes in agreement with the one derived by [29]. These equations are calculated per bay and so according to the employed methodology, they still have to be divided over top and bottom sections of the bay, be added for connecting bays and finally be divided over the nodes of the bays that will be applied. An example of the resulting wave spectrum applied at the height of the first bay of the reference structure is provided in Fig. 4-13.

$$\begin{aligned} S_{FF,waves}(f) &= S_{FF,I,waves}(f) + S_{FF,D,waves}(f) \\ S_{FF,I,waves}(f) &= \{\frac{C_m^2 g^2}{sinh^2 kd}\left(sinh[k(b+d)] - sinh[k(a+d)]\right)^2\}S_J(f) \\ S_{FF,D,waves}(f) &= \{\frac{C_d^2 gk\sigma_u^2}{k^2 sinh^2 kd}\left(sinh[k(b+d)] - sinh[k(a+d)\right)^2\}S_J(f) \end{aligned} \tag{4-23}$$

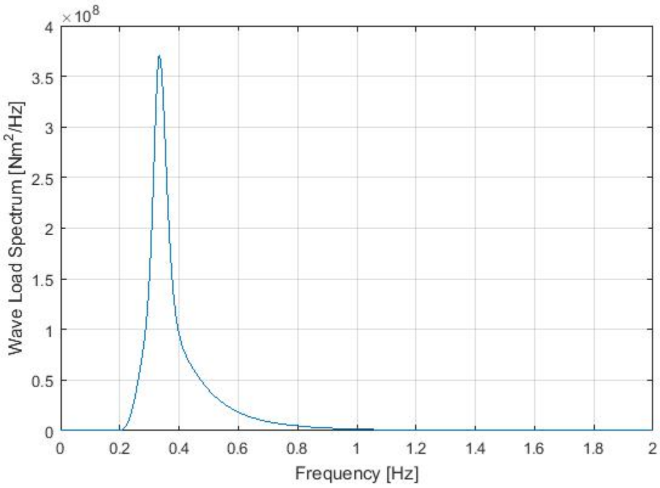


**Figure 4-13:** Resulting wave spectrum applied at the height of the first bay. Sea state characteristics: $H_s = 0.75m$ and $T_p = 5.78s$.

**Diffraction**

A final point addressed here is with respect to the basic assumption of Morison equation that the submerged members do not affect the waves. The effect that a structure has on the wave field, which is a probable small alteration on the wave flow, is called diffraction and the larger the diameter of the submerged structure the greater this effect is. Although lattice structures have relatively small member diameters, here the MacCumy-Fuchs correction is introduced. This correction factor is reducing the magnitude of the inertia coefficient according to Fig. 4-14 [47], where $\lambda$ is the wavelength given by Eq. 4-24. This factor applies to the $c_m$ coefficient and not the $C_m$ given by Eq. 4-18.

$$\lambda = \frac{2\pi}{k} \tag{4-24}$$

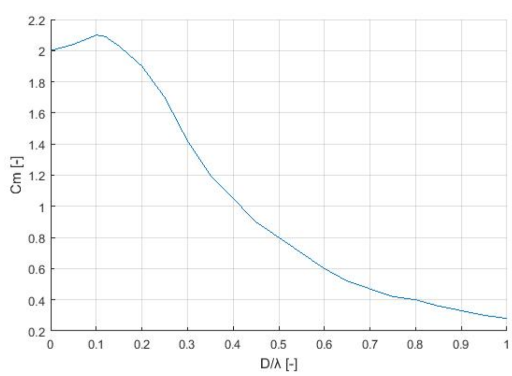


**Figure 4-14:** MacCumy-Fuchs correction factor introduce in the inertia coefficient to account for the diffraction effect.

In this chapter the methodologies and derivations employed in the developed model for the representation of random input loading from a certain wind and wave environmental state, have been described. Some assumptions were also introduced, when it was considered necessary for the simplification of the computational complexity. In the subsequent chapter, the description of the transfer function that will provide the stress spectrum calculation with respect to the random environmental input, will be in great detail explained.

Chapter 5

# Transfer Function for Wind & Waves

Having examined so far the methodologies applied in the developed model for the estimation of the dynamic response of a lattice structure through the derivation of the natural frequencies and the mode shapes as well as the modelling of the random environmental input data consisting of wind and wave characteristics, it is now time to analyse the procedure followed for the calculation of the desired output value, namely the stress spectrum and ultimately the estimation of the fatigue damage on certain members of the structure. This is accomplished through the derivation of a transfer function, which is widely used in the frequency domain, that connects the input value with an output value. As mentioned extensively in the literature, but as it was also experienced by the writer, the derivation of an appropriate transfer function between the induced environmental loads and the stress spectrum was the most challenging and demanding task of the developed model.

In the sections to follow, the methodology of the computation of the transfer function is presented along with the re-introduction of the aerodynamic damping in the model that its significance has already been indicated earlier in this report. Furthermore, the derivation of the fatigue damage calculation is also treated here. Although this process belongs to the last stage of the algorithm shown in Fig. 2-1, it is considered more convenient to analyse this topic in the current chapter.

## 5-1 Transfer Function Definition

The transfer function can be visualized as a "black box", which according to the input produces a certain output. What is important to understand is that the TRF is a characteristic property of the system and does not depend on the input, rather it relates the amplitude of the input with an output amplitude. The TRF is based on the requirement of the linearity of the system. Thus, if the input load is sinusoidal, then also the output produced by the TRF would be sinusoidal.

A common, simple example of a TRF when it comes to the calculation of the dynamic response of a structure can be derived by the equation of motion of the structure (described by Eq. 3-1). With the appropriate substitutions and derivations, one can get the vector of displacement amplitude per frequency, using:

$$X(\omega) = H(\omega) * F(\omega) \tag{5-1}$$

where, $F(\omega)$ is the vector of force amplitude, $X(\omega)$ is the vector of displacement amplitude and $H(\omega)$ is given by:

$$H(\omega) = \frac{1}{-[M]\omega^2 + [C]i\omega + [K]} \tag{5-2}$$

An example of the above equation of TRF for a member of the reference structure is presented in Fig. 5-1.

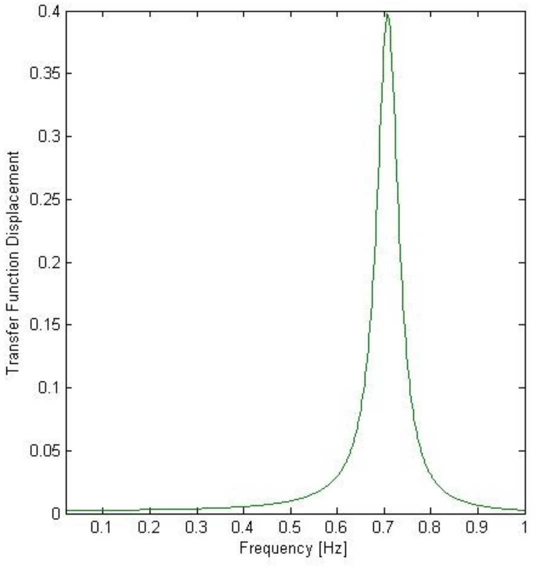


**Figure 5-1:** Linear transfer function for displacement of a member of the reference structure.

Example of a TRF that is also applied in this report, could relate the power spectra of the input force by multiplying it with the TRF squared to the output stress spectrum for each frequency, as shown in Fig. 5-2.

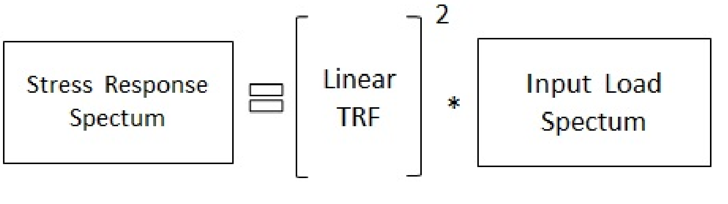


**Figure 5-2:** Example of how a transfer function acts as a "black box" in the frequency domain.

## 5-2 TRF Derivation in the Developed Model

The above short introduction provides a description of the functionality of the transfer function in the frequency domain and evidently its proper derivation is of high importance for the correct calculation of the final result. In Eq. 5-2 the linear transfer function that connects the force amplitude to the displacement amplitude for a member of the structure was presented. Instead of force and displacement amplitudes it is more common having a TRF that connects stress PSD with input load PSD as described in Fig. 5-2.

The procedure for deriving an appropriate TRF employed in this work is a common methodology widely used in the oil & gas industry as well as in the earthquake engineering for response analysis of structures, known as the mode superposition method [5], [14], [37], [12], [18] and [40]. This method is very efficient for MDOF systems, because the response analysis is obtained by decomposing the main scheme into a series of SDOF, which is easier to calculate. In order to accomplish this task, first the coupled equation of motion has to be decoupled in N equations (where N is the number of DOFs of the system) and then the response of the whole structure can be found by superimposing the N responses of the SDOF systems. A short introduction of the procedure for decoupling the equation of motion has already been shown in Sec. 3-1-3. However, in the subsequent section a more detailed analysis for uncoupling the modes will be presented as well as the derivations required for the calculation of the desired quantity (i.e. stress spectrum) will be described. The main steps of the methodology have been extracted from [14].

### 5-2-1 Uncoupling the modes

In order to assess the dynamic response of an N-DOF linear system, it is often advantageous to express the N independent displacement terms that constitute the mode shapes in the form of generalized coordinates that can serve as any set of displacements. This is due to their orthogonality characteristics, as it was shown in Section 3-1-3, and that they can usually describe all N displacements (or other quantity) of a system by making use of only a few mode shapes (this will be better understood in the upcoming derivations) [14].

By introducing the transformation for any modal component $x_n$ with normalized mode shape $\phi_n$ and modal amplitude $Y_n$:

$$\boldsymbol{x_n} = \boldsymbol{\phi_n Y_n} \tag{5-3}$$

the total displacement vector $\mathbf{x}$ of the structure can be obtained from Eq. 5-4:

$$\boldsymbol{x} = \boldsymbol{\phi_1 Y_1} + \boldsymbol{\phi_2 Y_2} + \ldots + \boldsymbol{\phi_n Y_n} = \sum_{n=1}^{N} \boldsymbol{\phi_n Y_n} \tag{5-4}$$

In Eq. 5-4 becomes evident that the $NxN$ mode shape matrix $\boldsymbol{\phi}$ serves to transform the generalized coordinates vector $\boldsymbol{Y}$ to the geometric coordinate vector $\boldsymbol{x}$ (Cartesian coordinates). The generalized components in $\boldsymbol{Y}$ are called the *normal coordinates* or *modal coordinates* of the structure.

Now using the normal coordinate transformation and its derivatives and pre-multiplying Eq. 3-1 with the transpose of the $n^{th}$ mode shape vector $\phi_n^T$ results in:

$$\phi_n^T m \boldsymbol{\phi} \ddot{\boldsymbol{Y}} + \phi_n^T c \boldsymbol{\phi} \dot{\boldsymbol{Y}} + \phi_n^T k \boldsymbol{\phi} \boldsymbol{Y} = \phi_n^T \boldsymbol{F} \tag{5-5}$$

However, by employing the orthogonality conditions as they were presented in Eq. 3-6 and Eq. 3-7, Eq. 5-6 becomes:

$$M_n \ddot{Y}_n + C_n \dot{Y}_n + K_n Y_n = F_n \tag{5-6}$$

where the definitions of modal coordinate mass, stiffness, viscous damping coefficient and load are given by:

$$\begin{aligned} M_n &= \phi_n^T m \phi_n = 1 \\ K_n &= \phi_n^T k \phi_n = \omega_n^2 \\ C_n &= \phi_n^T c \phi_n = \xi_n \\ F_n &= \phi_n^T F \end{aligned} \tag{5-7}$$

for $\xi_n$ (modal damping ratio) the following equation stands:

$$\xi_n = \frac{C_n}{2\omega_n M_n} \tag{5-8}$$

Finally, from the above derivations the desired result has been achieved, which transforms the coupled equation of motion of a MDOF system into a set of N uncoupled equations described by:

$$\begin{aligned} \ddot{Y}_n + 2\xi_n \omega_n \dot{Y}_n + \omega_n^2 Y_n &= F_n \\ n &= 1, 2, \ldots, N \end{aligned} \tag{5-9}$$

Before analysing the mode superposition method, is considered here important to present the significance of the damping to the response of the system, since the modal damping appears in the above computations and more specifically the importance of the re-introduction of the aerodynamic damping.

**Aerodynamic Damping**

As part of the methodology employed for the derivation of the wind force spectrum described in Sec. 4-2, the tower of the turbine is modelled as rigid, so that the top load exerted on the turbine could be applicable in almost all similar type of structures. However, since the tower is restricted in motion this results in neglecting the influence of the aerodynamic damping. Thus, the top load induced appears to be more severe than what it actually is with the reasoning explained in Sec. 4-2.

For this reason, a re-introduction of the aerodynamic damping as van der Tempel suggests is considered essential. The computation of the aerodynamic damping as a separate calculation has not been thoroughly investigated in the literature, since with the TD simulation softwares, the effect of it is taken into account already in the simulations. Nonetheless, some of the most discrete works have already been mentioned in Sec. 3-4-4 and in the DM a value of 2% or 3% for four or three leg structures has been employed, respectively. The difference between the aerodynamic damping value with respect to the number of legs, follows the argumentation that stiffer structures have a lower tower top movement. The significant influence of the aerodynamic damping can be clearly understood in Fig. 5-3.

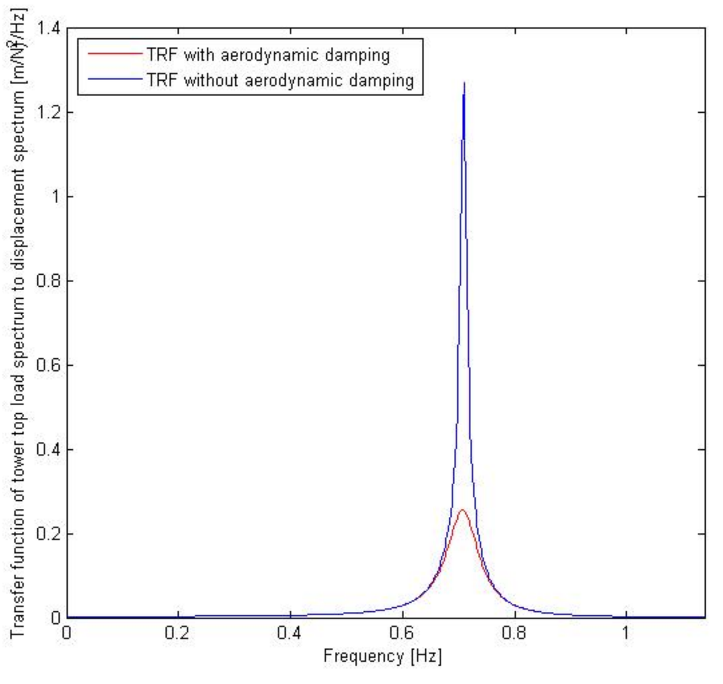


**Figure 5-3:** TRF of tower top load spectrum to displacement spectrum of the first mode of the reference structure. The effect of the aerodynamic damping introduced in the structural damping is significant.

### 5-2-2 Mode Superposition Method

As it was shown in the previous section the coupled equation of motion of the structure can be transformed into a set of uncoupled equations of SDOF systems. Each of these uncoupled equations can be utilized for the estimation of the total response of the structure by employing the mode superposition method.

The main principal of this methodology is that the total response of a MDOF system can be obtained by solving the N uncoupled modal equations and superposing their effect, as presented in Eq. 5-4. So, the estimation of the dynamic response of the structure can be calculated by assessing the response of each mode of the structure by multiplying a modal transfer function with the modal force input and then adding their influence. Nevertheless, when random excitations on the system are assumed (such as wind or wave excitations), each generalized forcing function should be considered as a stochastic process. If the excitations are stationary, then the response will also be stationary and in this case there is a higher interest in obtaining the power spectral density of the response [14]. This procedure can be better understood with the use of Figure 5-4. One can notice from this figure that the calculation of the transfer function has been separated into two steps, the first that connects each modal force input spectrum with a displacement spectrum and the second, where the modal displacement spectrum is converted to modal stress spectrum.

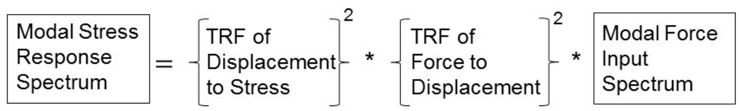


**Figure 5-4:** Procedure for calculating the modal stress spectrum.

The above figure with one alternation that will be explained in the following paragraph, can be translated into equations as follows:

$$S_{s_m s_n}(f) = B_m(f)B_n(f)H_m(f)H_n^*(f)S_{F_m F_n}(f) \tag{5-10}$$

where:

$$H_n(f) = \frac{1}{K_n(1 + 2i\xi_n \frac{f}{f_n} - (\frac{f}{f_n})^2)} \tag{5-11}$$

where $H(f)$ is the transfer function step between displacement spectrum and force spectrum, which is derived from the equation of motion for each mode and $B$ is the transfer function step between displacement spectrum and stress spectrum and it will be thoroughly explained in a subsequent section. The asterisk indicates the complex conjugate of the transfer function and $m$, $n$ represent different modes of the system and $i$ is the imaginary unit. Finally, the total response of the structure can be approximated by superimposing the response of each mode, according to equation:

$$S_{ss}(f) = \sum_m \sum_n S_{s_m s_n}(f) \tag{5-12}$$

At this point is important to analyse in greater detail the double summation of Eq. 5-12. As discussed above, $m$ and $n$ represent different modes of the structure and as suggested by [5] and [14] there is always present an existing interaction (coupling) between two or more closely spaced pairs of frequencies of a system, or as they are called the "interacting modes". Nevertheless, both authors claim that lightly damped systems, such as offshore structures, have well separated modes, which means that the interaction between them can be considered negligible. If this is the case, then Eq. 5-10 can be safely reduced to:

$$S_{ss}(f) = \sum_n^N S_{s_n s_n}(f) \tag{5-13}$$

where:

$$S_{s_n s_n}(f) = [B_n(f)]^2 [H_n(f)]^2 S_{F_n F_n}(f) \tag{5-14}$$

Evidently, the above equation is in accordance with the procedure as described by Fig. 5-4. Here is considered necessary to examine the effect of the interacting modes on the structure and determine if the proposed simplification is valid also for the lattice structures under investigation.

**Effect of Interacting Modes on the Structure**

The effect of the interacting modes on the system is examined only for the four first natural frequencies, since the lowest frequencies contain the highest energy levels. As mentioned, the influence of the coupled modes is greater for frequencies that are closely spaced, which means that a mode at a certain frequency will be more affected by two or three modes, whose frequencies are close to the one examined. This is also considered and presented in the figures that follow, which investigate the effect of the coupled frequencies on the transfer function between modal force spectrum and displacement spectrum, as given in Eq 5-15:

$$\begin{aligned} S_{ss}(f) &= \sum_{n}^{N} S_{s_n s_n}(f) \\ S_{s_m s_n}(f) &= H_m(f) H_n^*(f) S_{F_m F_n}(f) \end{aligned} \tag{5-15}$$

In Fig. 5-5 the influence of the second and third mode on the first one is shown (the first and second mode produce the same result, since their frequencies coincide), in Fig. 5-6a the influence of the second and fourth on the third mode is depicted and finally in Fig. 5-6b the impact of the third and fifth mode on the fourth mode is presented. The modal force spectrum applied here, as well as in the following graphs of this paragraph is a unit "white noise" spectrum. This means that the transfer functions presented below represent the dynamic behaviour of the structure with respect to the frequency.

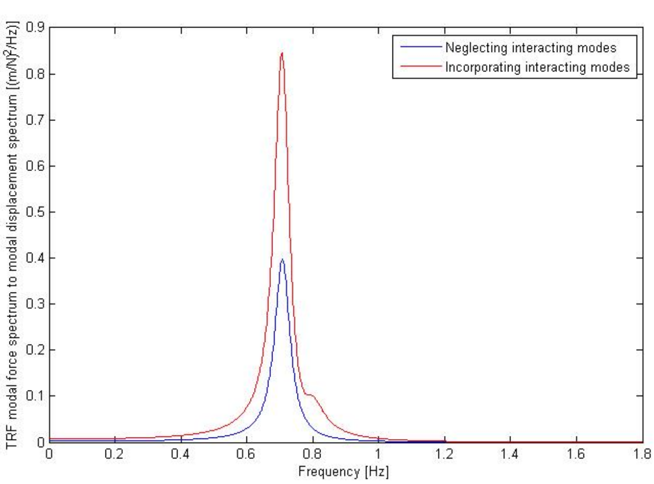


**Figure 5-5:** Influence of interacting modes on the first (and second) mode.

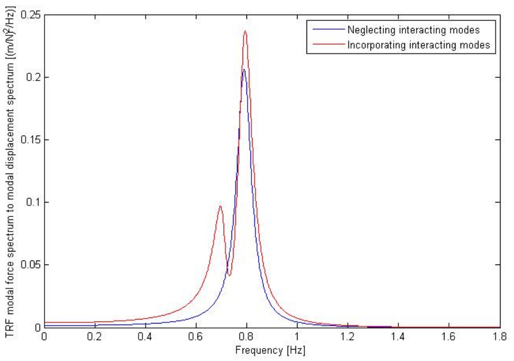


**(a)** Third mode interaction with $2^{nd}$ and $4^{th}$ mode.

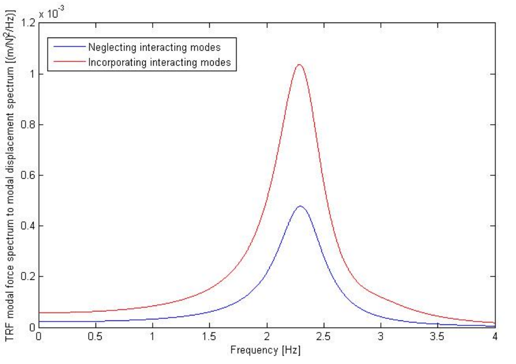


**(b)** Fourth mode interaction with $3^{rd}$ and $5^{th}$ mode.

**Figure 5-6:** Influence of interacting modes.

Clearly, the transfer functions in all the examined cases that take into consideration the interacting modes have a wider spectrum of frequencies in the region where their peak value appears. This is expected, since instead of the dynamic response of the structure being amplified only from one frequency, it now also receives the influence of closely spaced frequencies. However, it can be noticed that this effect can be neglected (as also suggested from the literature) to reduce the model complexity. Thus, Equations 5-13 and 5-14 are employed in the DM for the implementation of the modal superposition method.

**Modal Input Loading Spectrum**

One last term that has not yet been explained sufficiently in the above derivations is that of the modal force input spectrum, $S_{F_nF_n}$. As explained in Chapter 4, the input load spectrum induced by wind and waves is implemented in the developed model as discrete force spectra applied at certain DOFs. For example the thrust force spectrum component of the tower top load is applied in the x-direction of the node that represents the RNA.

Nevertheless, it has become clear from the above derivations that the required input for the modal superposition method is the modal force spectrum, which according to Clough, Barltrop and Halfpenny can be found by:

$$S_{F_nF_n}(f) = \sum_{a=1}^{k}\sum_{b=1}^{k} \phi_{an}\phi_{bn} S_{F_aF_b(f)} \tag{5-16}$$

where the subscripts $a$ and $b$ account for the different input loads and $k$ is the number of discrete input loadings present. $S_{F_aF_a}$ and $S_{F_bF_b}$ represent the PSD functions of two forces and $S_{F_aF_b}$ and $S_{F_bF_a}$ represent the CSD. However, it should be mentioned that the correlation between wind and wave forces has been neglected (according to Kühn) and also the correlation between the discrete wave forces has not been taken into account.

## 5-2-3 Order Reduction

The benefit of the modal superposition method will be clearly understood in this section. The displacement contribution for most types of loading is generally generated by the lower modes and tend to decrease for the higher ones. As a result it is usually not necessary to include all higher modes of vibration in the superposition process, which greatly decreases the computational time. Important here is also the fact that the reduced mode set must include all lower modes, without omission up to a mode with a chosen frequency [16].

However, the question that arises is what is the appropriate number of modes that can estimate the response of the system with accuracy. The answer can be simplistic, in the sense that the required mode number depends not only on the frequency content of the loading, but also on its spatial complexity, for example if further results apart from displacements are necessary and with which level of accuracy. On the other hand, it should be kept in mind that the mathematical idealization of any complex structural system tends to be less reliable in predicting the higher modes considered in a dynamic response analysis [14]. Some authors such as Ebert [18] suggest that for offshore application only the 2-3 first modes should be considered, where others such as Cook [16] imply that the required number of modes should be also relevant to the total number of DOF. It is evident that there is a level of uncertainty regarding this topic and the introduction of an error in the analysis is inevitable, since a large number of modes are disregarded.

Nevertheless, the higher modes that are not taken into consideration in the analysis have a small contribution on the dynamic response of the structure. This can be perceived from Fig. 5-7 that shows the influence of the modal transfer functions between modal force spectrum and modal displacement spectrum. In this graph is presented how the amplitude of the dynamic amplification (or else the energy level of those modes) decreases for the modes that are associated with the higher frequencies of the structure.

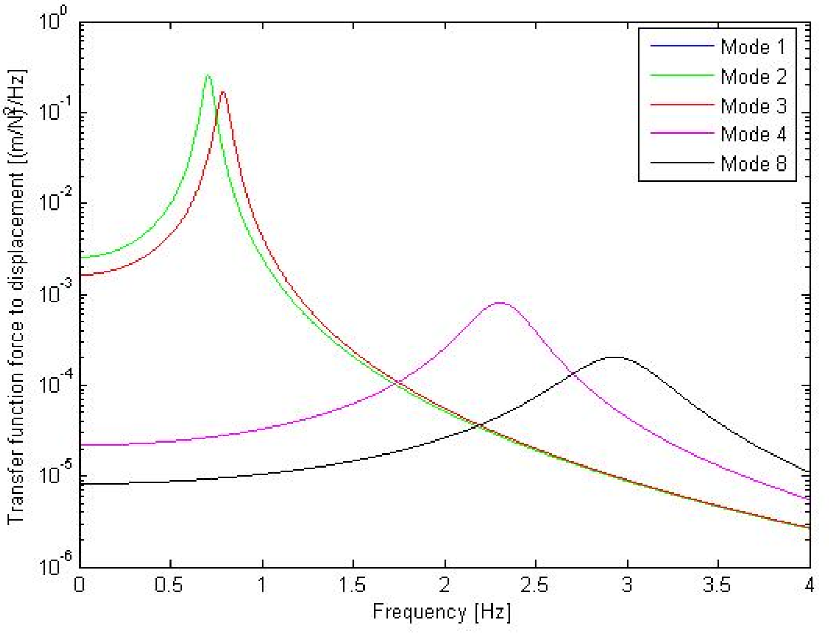


**Figure 5-7:** Influence of different modes of the structure on its dynamic amplification (Mode 1 & Mode 2 coincide).

### 5-2-4 Stress Spectrum Computation

Until now the first step of the transfer function of the input modal load spectrum to modal displacement spectrum has been analysed adequately and the current section treats the topic of the second step of the transfer function derivation, which is connected with the computation of the modal stress spectrum. The derivations that will follow are according to Cook [16] and Staerdahl [44].

One major theoretical part of the finite element analysis is the so called shape function of different type of elements (bars, beams, plates, etc.). The shape function is a function, which interpolates the solution between discrete values obtained at the mesh nodes [16]. In other words it defines the deformation of an element under a load or else it defines the element displacement field. Once the displacement field is obtained, then the moments and stresses can be calculated by differentiating it through the length of the element. For more details, the reader is advised to refer to the extensive literature on FEA.

The above described methodology will be explained in the form of equations in the derivations that will follow. The principal idea can be also described by making use of matrix multiplications, as shown in [53] and presented here:

$$[\sigma_{i,n}] = [D][N_{i,n}]\{q_{i,n}\} \tag{5-17}$$

where $[\sigma_{i,n}]$ is the modal stress matrix of the element $i$ and mode $n$, $[D]$ is the differential operator, $[N_{i,n}]$ is the shape function of the element $i$ and $\{q_{i,n}\}$ is the vector with the generalised coordinates of the element. Because this method makes use of the generalized coordinates of the elements and for clarification reasons, the local coordinates of a 3D beam along with the nodal DOF are once again presented in Fig. 5-8.

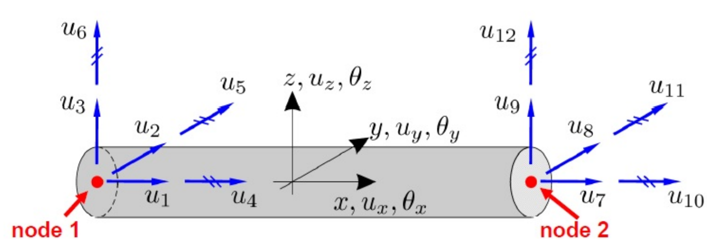


**Figure 5-8:** 3D beam with two nodes and 12 DOFs [44].

The displacement field at a certain section of a beam element can be computed by performing the matrix multiplications as shown:

**Table 5-1:** Displacement field to stress-strain field for 3D Euler Bernoulli beam.

| | | | | | | | | | | | | | | | |
|---|---|---|---|---|---|---|---|---|---|---|---|---|---|---|---|
| $u_x$ | | $N_1$ | 0 | 0 | 0 | 0 | 0 | $N_2$ | 0 | 0 | 0 | 0 | 0 | | $u_1$ |
| $u_y$ | = | 0 | $N_3$ | 0 | 0 | 0 | $-N_4$ | 0 | $N_5$ | 0 | 0 | 0 | $-N_6$ | * | $u_2$ |
| $u_z$ | | 0 | 0 | $N_3$ | 0 | $N_4$ | 0 | 0 | 0 | $N_5$ | 0 | $N_6$ | 0 | | $\vdots$ |
| $\theta_x$ | | 0 | 0 | 0 | $N_1$ | 0 | 0 | 0 | 0 | 0 | $N_2$ | 0 | 0 | | $u_{12}$ |

where $u_{1,2,...,12}$ are the element DOFs in local coordinates and $u_x$, $u_y$, $u_z$ and $\theta_x$ are the displacements in the x, y and z direction and the rotation in the x direction, respectively. The shape functions for a 3D beam element $N_i$ can be found in Appendix A. Furthermore, the rotations in the y and z direction can be calculated as:

$$\begin{aligned} \theta_y &= \frac{du_z}{dx} \\ \theta_z &= \frac{du_y}{dx} \end{aligned} \tag{5-18}$$

However, it is considered important at this point to remind that the Euler-Bernoulli beam does not take into account the shear effects. Moreover and in order to simplify the calculations, the assumption of excluding the local torsional effects from the stress calculations is made. This is a very important simplification that might lead to erroneous results for the fatigue damage calculation, since (as also shown in the previous chapters) the torsional effects are highly present in this type of structures. Hence, for the stress calculation only the displacements in the 3 axes are taken into consideration.

Following the methodology as explained above, since the element displacement field is now defined, the moments and stresses can be calculated. In the developed model the element under investigation is provided as an input parameter, but the points on the cross-section of the element for which the stresses are calculated are defined on the outer diameter of the beam as presented in Fig. 5-9. Those two points were selected, so that the effect of the in-plane (point A) and out-of-plane (point B) vibration would be presented.

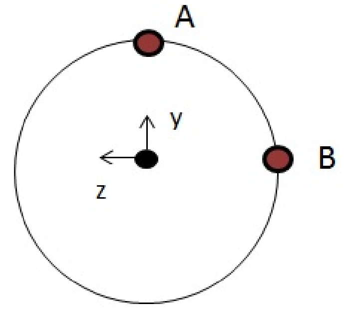


**Figure 5-9:** Points on the cross-section of an element, where the stresses are calculated in the DM.

Hence the stress calculation for points A and B is given by equations:

$$\sigma_A = SCF_1 E\epsilon_{xx} + SCF_2 \frac{M_y}{I} z \tag{5-19}$$

$$\sigma_B = SCF_3 E\epsilon_{xx} + SCF_4 \frac{M_z}{I} y \tag{5-20}$$

where SCF in Eq. 5-19 and 5-20 are the stress concentration factors required according to the standards for the locally increased nominal stresses due to the geometrical discontinuities. The moments at points A and B are given by:

$$M_y = EI\frac{d^2u_z}{dx^2}$$
$$M_z = EI\frac{d^2u_y}{dx^2} \tag{5-21}$$

After the above description of the necessary equations for the modal stress calculation for an element of the structure, now the above derivations can be imported in term $B_n$ of Eq. 5-14 and get the stress spectrum of an element. Finally, the total transfer function from input load spectrum to stress spectrum is presented for a point on the diagonal brace and on the leg (shown in Fig. 5-10 in Figures 5-11 and 5-12. The input spectrum is a white noise spectrum.

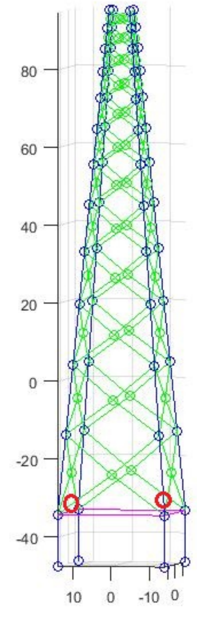

**Figure 5-10:** The diagonal brace and the leg where the TRF has been calculated are indicated in the red circles.

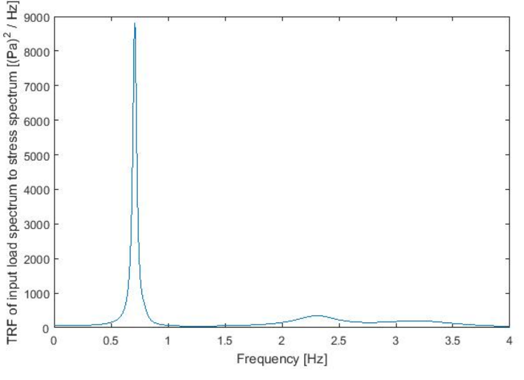

**(a)** Point A.

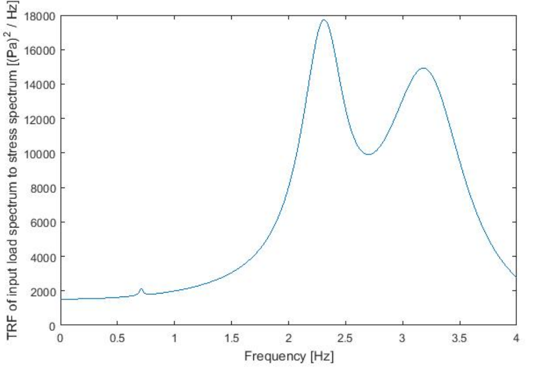

**(b)** Point B.

**Figure 5-11:** TRF of white noise input load spectrum to stress spectrum for diagonal brace.

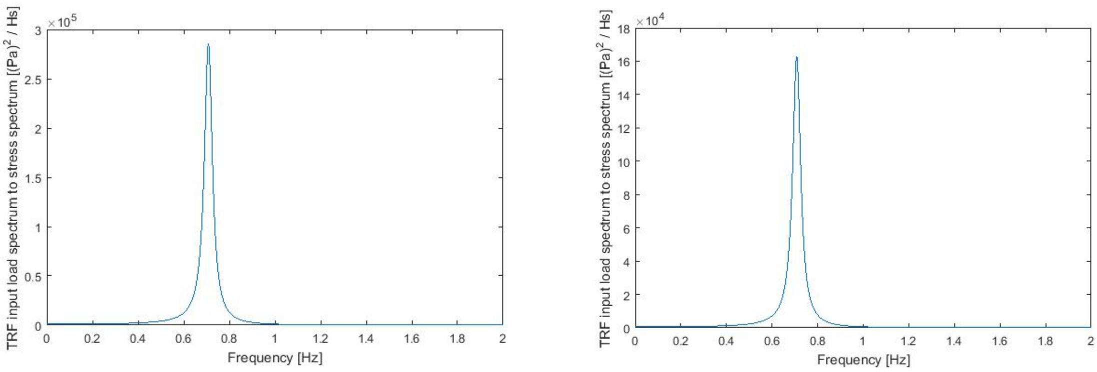


**(a)** Point A. **(b)** Point B.

**Figure 5-12:** TRF of white noise input load spectrum to stress spectrum for the leg at mudline.

Evidently, the complete TRFs for different members of the structure can deviate in magnitude and in shape, meaning that they can be influenced more by other frequencies. It is obvious that for the diagonal brace of the reference structure, the magnitude of the induced stress spectrum is smaller than the one of the point located at the leg. More interesting is the fact that point B of the diagonal brace seems to be influenced mainly from higher order modes and this could be generated by some local deformation effects present at the diagonal members close to mudline as it can be also identified from the modeshapes of the structure in Fig. 3-13 d. However, point A of the diagonal brace and points A & B of the leg are mainly influenced by the first two natural frequencies of the structure. Unfortunately, those results cannot be validated, since for the simulations performed in GH Bladed for the reference structure no tower modes were included. Nonetheless, the benchmark of the output produced by the DM will follow in Chapter 6.

## 5-2-5 Superposition of the Stress Spectrum

The transfer function described above can be utilized as a black box both for the wind and the wave loading, since it relates the input load spectrum to the output stress spectrum. In Chapter 4 the derivation of the load spectrum induced by wind and wave random excitations was described and presented in Figures 4-4 and 4-13. By making use of the methodology described above, the output stress spectra for a specific member can be now obtained and is presented in Figure 5-13, which results from the wind input characteristics, and in Figure 5-14, which results from the wave input load spectrum.

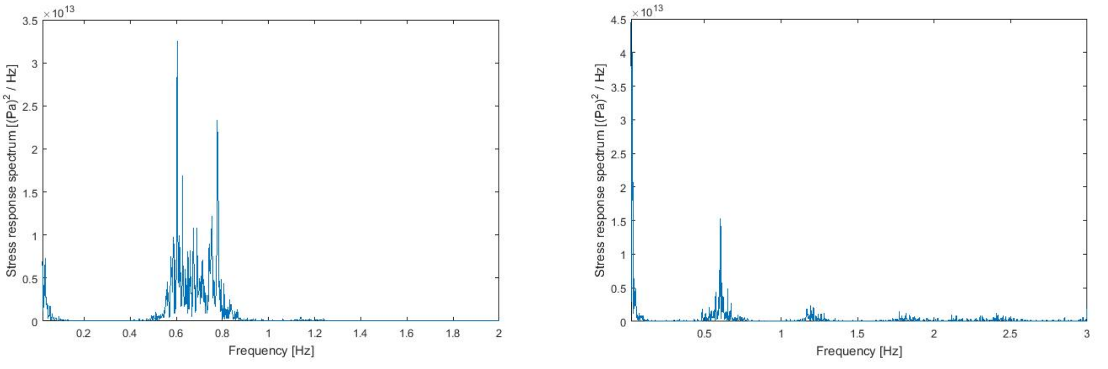

**(a)** Point A. **(b)** Point B.

**Figure 5-13:** Stress response spectrum for a diagonal brace at mudline due to wind input loading spectrum.

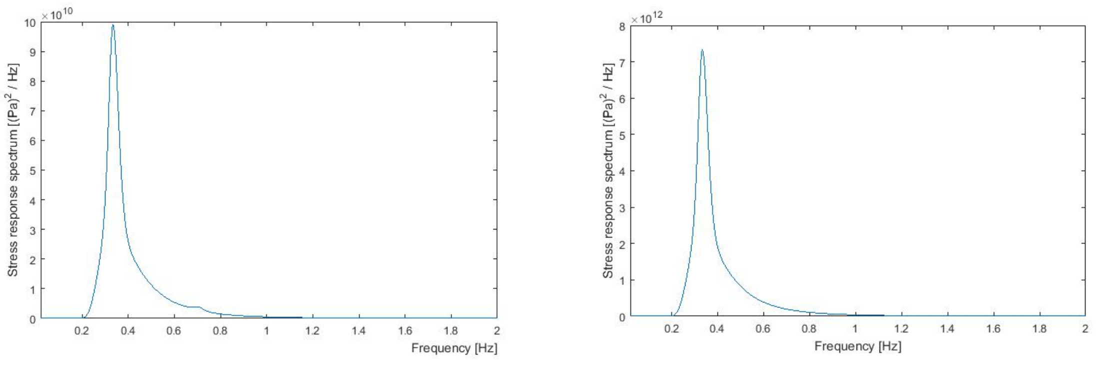

**(a)** Point A. **(b)** Point B.

**Figure 5-14:** Stress response spectrum for a diagonal brace at mudline due to wave input loading spectrum.

A comparison of the wind and wave induced stress spectrum on the same brace, shows the difference between the noisy signal output for the wind loading and the smooth graph resulting from the equations describing the wave load characteristics. This is the case, due to the few TD simulations used for creating the wind load spectrum and due to the smooth load spectrum that is calculated from the equations described in Sec. 4-4-3. Moreover, some important remarks that can be made here are listed below:

- The identified high peak at a frequency close to $0.6Hz$ can be distinguished as the 3P loading of the RNA.
- In accordance with Fig. 5-11a, Point A has another sharp peak in the vicinity of $0.7Hz$, which is the first and second natural frequency of the structure. On the other hand, for point B the peak at this frequency is greatly reduced, whereas the influence of the higher modes has clearly a stronger effect than on point A.
- For the stress spectrum induced by the wave loading, it is noticeable that point B,

representing the out-of-plane loading has a higher resulting magnitude than the in-plane loading (point A).

One of the principal assumptions made for the developed model, as described in Chapter 2 and as suggested by Kühn [27] and van der Tempel [47], is that the wind and wave input loading can be regarded as independent and stationary processes. Hence, the output stress spectrum produced by the DM can be safely superimposed and create a total stress spectrum for a specific member of the structure. This action is presented in Fig. 5-15 and the higher contribution of the wave loading on point B is identified.

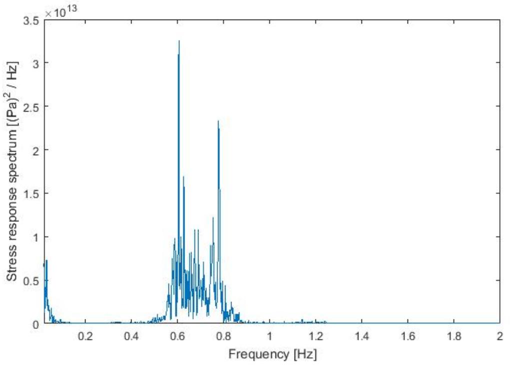


**(a)** Point A.

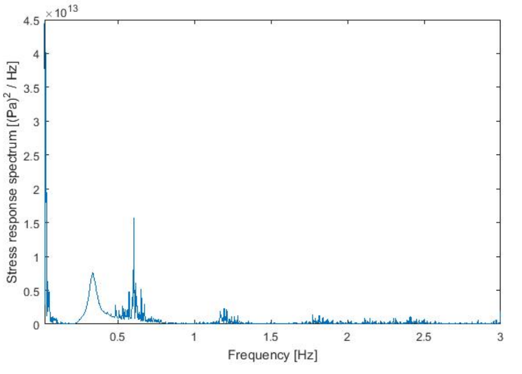


**(b)** Point B.

**Figure 5-15:** Stress response spectrum for a diagonal brace at mudline due to combined (wind & wave) loading spectrum.

In the following and last section of the chapter, the methodology followed to arrive at a fatigue damage result due a stress spectrum for a member will be described.

## 5-3 Fatigue Damage Estimation

As mentioned, although the fatigue damage estimation is considered as a separate step of the proposed algorithm provided in Fig. 2-1, it is described in the current chapter. This is selected in such a way, since the employed methodology is straight forward and commonly used for FD calculations.

Fatigue is the phenomenon that results to material failure caused by gradual growth of cracks due to continuously varying stresses. The mean stress seemingly is not of great influence to the number of cycles required for a material (e.g. steel) to fail. Nonetheless, what appears to be important is the stress range (S) rather than the stress level [47]. In order to assess fatigue damage for steel (or any similar material) numerous experiments need to be conducted. From those experiments the number of cycles to failure is counted for certain stress ranges, which leads to the formulation of an S-N curve.

**S-N Curve**

The S-N or Wöhler curve is provided in many design standards for different structure and environmental conditions and is described by:

$$log(N) = log(\alpha_{int}) - mlog(\Delta\sigma) \tag{5-22}$$

where $\Delta\sigma$ is the stress range, $N$ is the predicted number of cycles to failure for the stress range $\Delta\sigma$, $m$ is the negative slope of the S-N curve and $log(\alpha)$ is the intercept of $logN$ axis by the S-N curve. For steel usually the S-N curves have a negative inverse slope of 3 and for higher cycles a negative inverse slope of 4 or 5. A typical S-N curve will be presented in the following chapter.

After specifying the S-N curve, then the known stress variations (that can be calculated from a stress spectrum) can be binned in number of variations $n_i$ for each stress range class $S_i$. Next, the fatigue damage can be calculated according to the Palmgren-Miner (or simply the Miner) rule, as a summation of the damage caused by each stress range over the stress history by:

$$D_{fat} = \sum_i \frac{n_i}{N_i} \tag{5-23}$$

### 5-3-1 Counting Method

Several methodologies exist that can determine the stress variations (as discussed above) from the spectral properties of a stress spectrum, which can be referred to as counting methods. All of the existing methods in frequency domain have some common steps, which include the determination of a probability distribution of the stress peaks and the estimation of the total number of peaks occurring in the period under consideration [47].

Among the most prominent counting methods in the FD, Dirlik's method, which is an empirical methodology, appears to have the most accurate results when compared to rainflow counting, which is the commonly accepted methodology from the TD counting methods in the wind industry. For this reason, Dirlik's methodology is also employed in the developed model and the reader can refer to the literature for more details of this methodology. It is important to mention at this point that Dirlik's method makes use of the zeroth, the first, the second and the fourth spectral moments, which requires an integration over the stress spectrum. The integration method adopted in this thesis is the trapezoidal integration.

## 5-4 Concluding Remarks

By finalizing the current chapter, the complete overview of the methodology applied in the DM has been presented. Each stage of the employed algorithm has been explained at a sufficient level of detail with the utilization of the reference turbine and structure when it was considered necessary to benchmark results with commercial software, as it was shown in Section 3-5-1. In the following chapter a case study of the lattice structure of the Dutch company 2-B Energy will be presented. This case study will serve as a verification of the DM, since the resulting fatigue damage for power production load cases exerted on the structure will be compared with the results as computed by the software package GH Bladed.

# Chapter 6

# Case Study: 2-B Energy Structure

Having formulated the methodology for the fatigue damage estimation of offshore wind turbines full heigh lattice structures, a case study is performed in this chapter with the objective being the verification of the results produced by the developed model. Furthermore, another substantial goal of this case study is to indicate possible limitations of the model and identify key points of the methodology that can be improved in a future work. The results generated by the DM will be compared with the ones computed from the TD commercial software package GH Bladed.

In the subsequent sections a review of the restrictions and assumptions made throughout this report will be reintroduced and then the structure of 2-B Energy will be presented along with the investigation of the accuracy of the results produced by the DM.

## 6-1 Review of Restrictions and Assumptions of the DM

During the effort of establishing a simplified nature of the developed model, some inevitable assumptions were made and have been clearly underlined throughout this report. Nevertheless, the adopted simplifications were always considered with a critical reflection upon the accuracy of the model, but understandably they introduce a level of uncertainty to the results.

Since the purpose of the current chapter is to investigate the precision of the tool with respect to fatigue damage estimation, it is considered appropriate to summarize and present here once more the most important assumptions made, as well as some restrictions of the DM that might have not yet been plainly reported:

- The element employed for the idealization of the real structure is an Euler-Bernoulli beam instead of a Timoshenko beam. This means that the shear deformations in the DM are neglected.
- The developed model, as it has been presented is sensitive to the mesh density and the results can greatly vary.

- The wave loading is calculated while considering an equivalent diameter model and then applied only on the submerged parts of the legs of the lattice structure, as described in Sec. 4-4-1. This could result in more conservative estimations of the wave loading. Furthermore, another more conservative simplification made regarding the waves is that the phase difference of the speed and acceleration terms in the Airy equation is neglected.
- Local torsional effects are neglected from the stress computation. Hence, the equations derived for the stress calculation take into account only the displacements of the beam.
- Wind and wave misalignment is not incorporated in the DM, which means that the calculations will probably be again more conservative, since uni-directionality of wind and waves is regarded as more severe [32].
- Only power production cases can be examined from the DM and other non-operating conditions can not be included. However, for fatigue load calculations the occurrence of the remaining cases is small and their contribution on the lifetime damage can be neglected.

## 6-2 2-B Energy Structure and Turbine

In order to be able to assess and understand the results that will be presented in the subsequent sections, there is the necessity to present initially the characteristic attributes of the structure and the turbine model that are to be used for this case study.

The structure designed and developed by 2-B Energy is a three leg lattice structure that facilitates a two bladed downwind wind turbine also developed by the Dutch company. The structure used here is designed for a site with water depth of 30 m and the idealization of the support structure used in this chapter as produced by the DM is presented in Fig. 6-1. Some of the gross properties of the turbine are given in Table 6-1.

**Table 6-1:** Characteristic properties of $2B6$ turbine model

| **2B6 Turbine Model** | |
|---|---|
| Rating | 6 MW |
| Number of blades | 2 |
| Rotor Diameter | 140 m |
| Rotor Orientation | Downwind |
| Control | Variable Speed, Individual Pitch |
| $U_{cut-in}$, $U_R$, $U_{cut-out}$ | 4, 12.5, 25 $m/sec$ |
| $\Omega$ | 8.55 - 11.8 RPM |
| Mass (RNA) | ±500 tons |

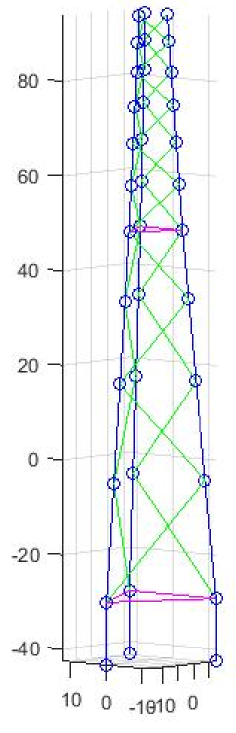


**Figure 6-1:** Idealization of the 2-B Energy support structure produced by the DM.

## 6-3 Case Study Input Parameters

The relevant data for the site and the fatigue assessment that will be given here are common input values for the calculations performed in the two frameworks, namely the DM and GH Bladed.

### 6-3-1 Site Characteristics

The site chosen to be investigated for this case study is located at the North Sea, west of Denmark with the closest port being Esjberg, which is 70 km away. The exact coordinates of the site are $55^o$ $27'$ N and $07^o$ $24'$ E and its location is presented on the map of Fig. 6-2. A representative depth of this site was taken equal to 30 m.

For a lifetime fatigue assessment of a turbine, there is the necessity for the establishment of concrete environmental states that include information about the probability of occurrence, the wind speed, the significant wave height and the wave period. For the formation of these environmental states a 3D scatter diagram for the site under consideration needs to exist. The 3D scatter diagram resulted from 2D diagrams that included measurements for the specific site and it can be found in Appendix C. The resulted, lumped environmental states are summarized in Table 6-2.


**Figure 6-2:** The location on the map of the site used for the case study.

**Table 6-2:** Lumped environmental states used for the case study.

| State | $V_{avg.}$[m/sec] | TI[%] | $H_s$[m] | $T_p$[s] | Occ.[%] |
|---|---|---|---|---|---|
| **1** | 3 | 34.31 | 0.75 | 5.79 | 7.68 |
| **2** | 4 | 25.87 | 1.25 | 6.84 | 7.41 |
| **3** | 5 | 21.66 | 1.75 | 6.32 | 5.31 |
| **4** | 7 | 19.12 | 0.25 | 8.42 | 10.14 |
| **5** | 7 | 19.12 | 0.75 | 7.37 | 9.58 |
| **6** | 9 | 16.23 | 1.25 | 5.79 | 7.19 |
| **7** | 11 | 15.33 | 3.5 | 7.37 | 4.20 |
| **8** | 13 | 14.06 | 0.75 | 5.79 | 10.33 |
| **9** | 15 | 13.60 | 2.25 | 5.79 | 8.64 |
| **10** | 16 | 13.22 | 2.75 | 6.32 | 8.64 |
| **11** | 17 | 12.89 | 0.75 | 5.26 | 7.99 |
| **12** | 17 | 12.89 | 1.75 | 5.79 | 10.33 |
| **13** | 25 | 11.53 | 6.5 | 8.42 | 1.66 |
| | | | | | **99.1** |

## 6-3-2 Load Factors and S-N curve

A common practice when evaluating loads exerted on wind turbines or structures is to include into the calculations factors that compensate for the uncertainty introduced for the loads consideration. The load factor is one of those factors, provided as an input parameter. For the specific case study it was set equal to 1, since the purpose of this chapter is to examine the level of accuracy of the DM when compared to GH Bladed. Understandably, this load factor has no influence on this comparison. Similarly, the SCFs as introduced in Sec. 5-2-4 were set equal to 1 in both frameworks.

The S-N curve used was defined in accordance with the standards [4] and the characteristic properties that need to be defined are the intercept, the slope of the curve and the environment (air, water, etc.) as well as the position of slope change. The S-N curve employed for this case study is presented in Fig. 6-3. Finally, the lifetime considered is 20 years and an availability of 95 % was also included in the calculations.

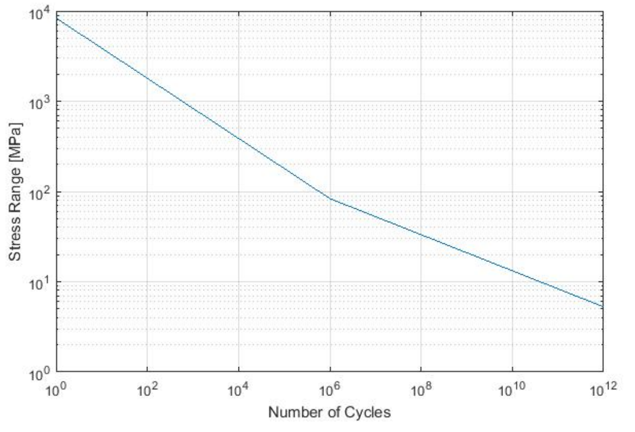


**Figure 6-3:** The S-N curve used.

## 6-4 Modal Analysis Comparison

In order to properly assess and compare the resulting fatigue damage values, it is also essential to compare the natural frequencies and modeshapes of the structure that are the main indicators of its dynamic behaviour. Furthermore, as it has been seen in the previous chapters, they have also a significant influence on the complete methodology of deriving the fatigue damage. Hence, this intermediate step of the model is also examined here.

As presented in Table 6-3, the natural frequencies as calculated by the DM compare at a sufficient level with those extracted from ANSYS. In fact, the percentage error between the two values is smaller than the one computed for the reference structure, as shown in Sec. 3-5-1. Moreover, the error for the torsional natural frequency is in this case significantly smaller than the one presented in Sec. 3-5-1, where it was identified that the developed model lacks in accuracy due to reasons explained in the aforementioned section.

As far as the modeshape estimation is concerned, the results produced by the DM are provided in Fig. 6-4 and 6-5. It can be noticed that the local effects identified on the lower members of the structure, close to mudline, are also present here, as it was the case for the reference structure as well. The reason behind this effect could be the relatively low mesh density (5 elements per member were used) or a limitation of the model on the accurate calculation of the deflections on the lower parts of the structure that are more heavily loaded.

**Table 6-3:** Natural frequency comparison for the first 10 modes between ANSYS and the DM.

| Mode | Ansys [Hz] | DM [Hz] | Percentage Error[%] |
|---|---|---|---|
| **1** | 0.4875 | 0.4702 | 3.54 |
| **2** | 0.4875 | 0.4703 | 3.54 |
| **3** | 1.6465 | 1.4359 | 12.79 |
| **4** | 1.8349 | 1.8417 | 0.37 |
| **5** | 1.8361 | 1.8418 | 0.31 |
| **6** | 2.4768 | 2.1499 | 13.20 |
| **7** | 2.6942 | 2.6929 | 0.05 |
| **8** | 2.6968 | 2.6930 | 0.14 |
| **9** | 3.3238 | 2.9776 | 10.41 |
| **10** | 3.4397 | 3.4529 | 0.38 |

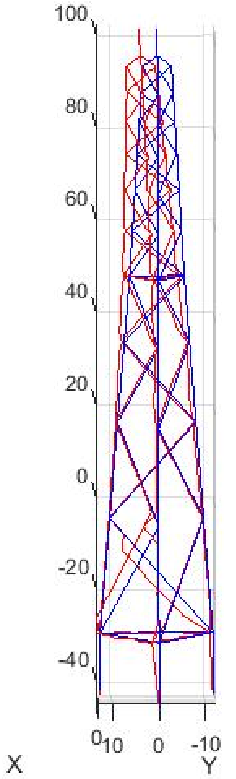


**Figure 6-4:** First modeshape of the structure as calculated from the DM. Bending about the x-axis.

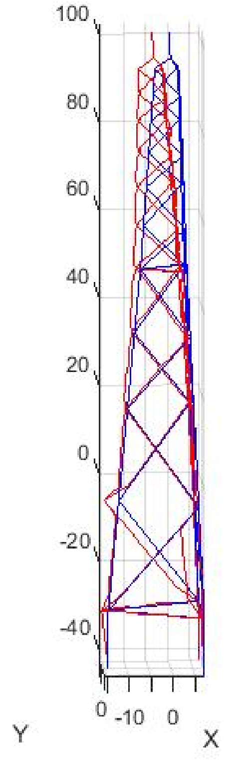


**Figure 6-5:** Second modeshape of the structure as calculated from the DM. Bending about the y-axis.

## 6-5 Results and Discussion

Since lattice structures are multi-member structures, it is considered appropriate to compare the calculated results of the model for different type of members with GH Bladed in order to properly assess its performance. Although the most accurate comparison would be the selection of several members along the structure and at different elevations, due to the amount of time required to post-process all of the simulations run (mainly in GH Bladed), it was decided to examine three different members of the structure, located close to mudline that are subjected to the highest loading.

Thus, in the following sections the results extracted from the DM for a diagonal brace, a leg and a horizontal brace are compared with the equivalent ones as calculated by GH Bladed. The examined members of the structure are presented in Fig. 6-6 as well as the direction of the wind and wave loading.

Apart from the comparison of the resulting fatigue damage values between the developed model and GH Bladed, it is certainly advantageous to also compare the stress spectra as computed by both frameworks. This can help the interpretation of the functionality and the accuracy of the DM. For this purpose, the stress spectra of six different environmental states for both points and the three examined members were chosen to be presented. The environmental states were selected in such a way so that they reflect the response of the structure (and in extension of the model itself) in low, medium and high environmental loading. Hence, the states chosen are 1, 3, 6, 8, 11 and 13.

All of the stress spectrum comparison figures can be found in Appendix D and the discussion regarding those graphs will take place in the last section of this chapter. However, the stress spectrum comparison for environmental state 6 will also accompany the fatigue damage results provided in the subsequent sections for the investigation of each member.

**Figure 6-6:** Location of the examined members on the structure. The red circles represent the points where the fatigue damage values were calculated and the black arrow shows the directionality of the loading. The RNA is wrongly displayed here, since it is a downwind model.

### 6-5-1 Diagonal

By looking at Figure 6-7 (the fatigue damage results are also provided in Table D-1 of App. D), it can be noticed that for the diagonal member the DM produces quite satisfying results in comparison with Bladed. This is especially the case for the environmental states 4, 5, 6, 7, 8, 9 and 10. For the cases where high wind and wave loading is exerted on the structure (states 11, 12 & 13), the DM has the tendency to overestimate the resulting damage, which makes it more conservative. This was expected to some extent, due to some of the simplifications adopted and analysed on Chapter 5, such as the adaptation of the equivalent diameter model for the calculation of the hydrodynamic loading, the wind and wave uni-directionality, etc. These simplifications tend to make the DM more conservative on the calculation of the fatigue damage. It should also be reminded that the overestimation of the damage, as well as of the stress spectrum (presented in Fig. 6-8), could originate from the local deformation effects produced on the braces close to mudline. This has been noted also in Sec. 6-4 and can be seen on the modeshapes presented in Figures 6-4 and 6-5.

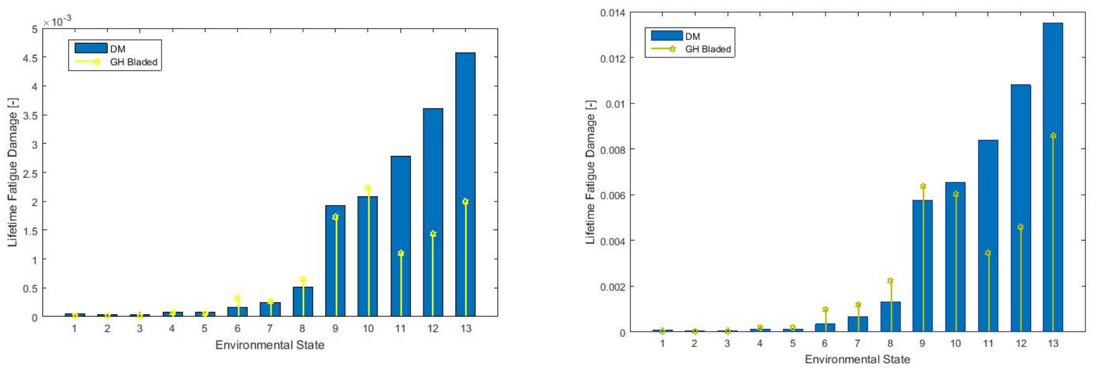


**(a)** Point A.

**(b)** Point B.

**Figure 6-7:** Comparison of the resulting contribution to lifetime fatigue damage for each examined environmental state as calculated by GH Bladed and the developed model for a diagonal member close to mudline. Point A is shown in (a) and Point B in (b).

As mentioned in the beginning of this section it is important to compare intermediate results between the two frameworks. For this reason, the comparison of the computed stress spectrum between GH Bladed and the DM for the two points under investigation is presented in Fig. 6-8 (similar conclusions that will be extracted for the examined state here, also apply for the rest of the environmental states as given in App. D).

Those graphs provide very interesting results, since the frequencies where the peak of the stress happens represent valuable information of the system. In more detail, the peaks around the frequencies of $0.2Hz$, $0.4Hz$, $0.8Hz$ represent the 2P, 4P and 8P rotational sampling frequencies of the (two bladed) turbine, respectively and the first and second natural frequencies of the structure can also be identified at $0.47Hz$ and the third natural frequency around $1.4Hz$ as calculated by the DM. The margin between the 4P of the turbine and the first two natural frequencies as calculated by ANSYS (and effectively by GH Bladed) is around 20%, which is a safe margin for avoiding the loading amplification as introduced by the turbine. However, in the case of the DM this margin is smaller, resulting in probably an increment of the damage, due to the coincidence of the natural frequency of the structure and the 4P rotational sampling frequency of the turbine, which for a two bladed machine, accommodates high energy content.

Furthermore, the difference on the calculation of the torsional natural frequency between the DM and Bladed (as well as ANSYS) is clearly visible, since GH Bladed appears to have a peaked frequency at the region of $1.65Hz$, which is the torsional natural frequency as calculated by ANSYS (Table 6-3). Evidently, the DM appears to calculate sharper and less wide peaks than Bladed. Finally, one important remark is that the peak that appears at the region around $0.1Hz$ for the Bladed simulations, is most likely the 1P rotational sampling frequency of the turbine that is not peaked from the developed model or the excitation frequency of the wave spectrum that is calculated with a lower magnitude on the DM and does not appear in the graph. The origin of this peak will be investigated more in Section 6-5-4.

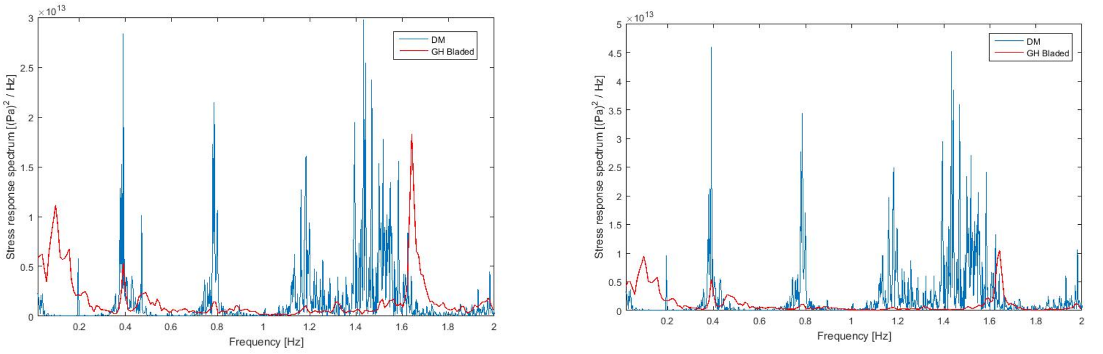


**(a)** Point A.

**(b)** Point B.

**Figure 6-8:** Comparison of the stress spectrum calculation between the Developed Model and GH Bladed for the diagonal brace. Point A is shown in (a) and Point B in (b).

## 6-5-2 Leg

By observing the results presented in Fig. 6-9, it becomes clear that the DM lacks in accuracy for the fatigue estimation on the leg, especially for environmental states with high loading input, since it highly underestimates the damage. This result is consistent with the figure of the stress spectrum comparison provided in Fig. 6-10 and with the rest of the environmental states as provided in Appendix D-2. It can be noticed from those graphs that the DM correctly estimates the resulting stress spectrum at the examined point of the leg both in magnitude and in frequencies where it has its peak value. Nonetheless, the peaks are very sharp and narrow, which results in the wrong calculation of the spectral moments and consequently in false fatigue damage estimation.

Moreover, it is evident from Fig. 6-10 and from the respective figures presented in App. D that the leg stress spectrum is for both points mainly influenced by only the first and second natural frequency of the structure. This comes in agreement with the transfer function presented in Fig. 5-12 for the reference structure, where it was presented that also in that case the only significant effect on the dynamic behaviour of the leg is caused by the first two natural frequencies.

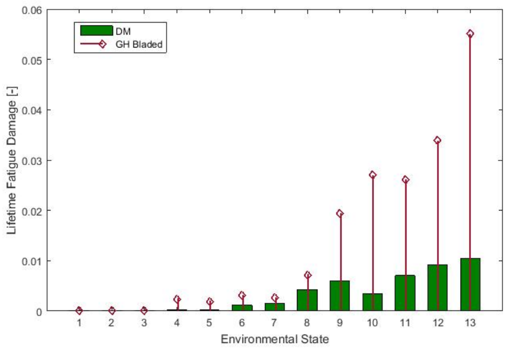


**(a)** Point A.

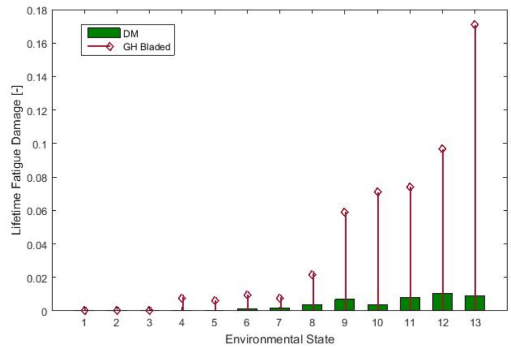


**(b)** Point B.

**Figure 6-9:** Comparison of the resulting contribution to lifetime fatigue damage for each examined environmental state as calculated by GH Bladed and the developed model for a leg close to mudline. Point A is shown in (a) and Point B in (b).

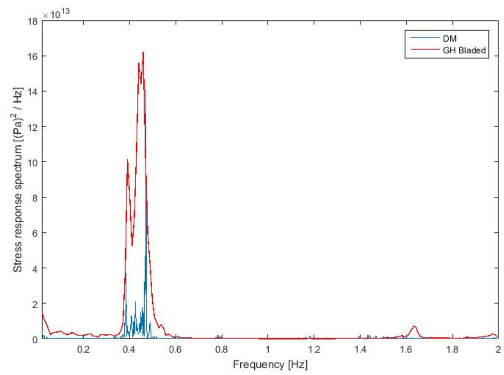


**(a)** Point A.

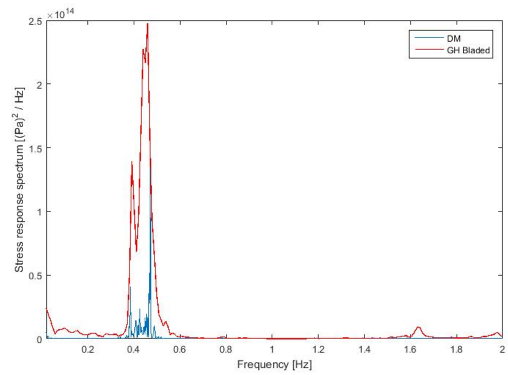


**(b)** Point B.

**Figure 6-10:** Comparison of the stress spectrum calculation between the Developed Model and GH Bladed for the leg. Point A is shown in (a) and Point B in (b).

### 6-5-3 Horizontal

For the horizontal brace the developed model, as presented in Figure 6-11, overestimates the resulting fatigue damage for point A, which is affected by in-plane vibrations and underestimates the damage for the out-of-plane loading in point B. Furthermore, for the stress spectrum calculation shown in Fig. 6-12 as well as in App. D, similar conclusions can be derived with the ones extracted for the case of the leg investigation.

The incorrect stress and damage estimation might be also caused by the local deformation effect on the braces close to mudline, similar to the diagonal brace.

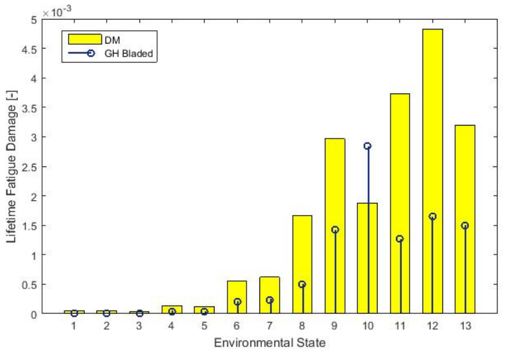


**(a)** Point A.

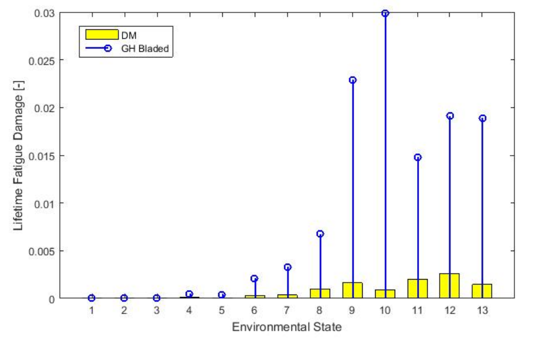


**(b)** Point B.

**Figure 6-11:** Comparison of the resulting contribution to lifetime fatigue damage for each examined environmental state as calculated by GH Bladed and the developed model for the horizontal brace at the mudline. Point A is shown in (a) and Point B in (b).

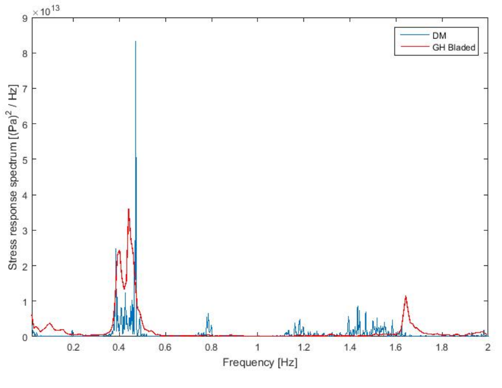


**(a)** Point A.

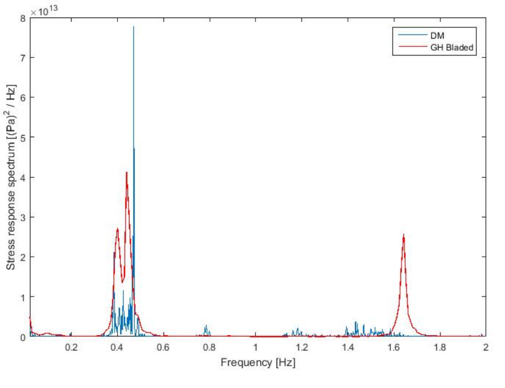


**(b)** Point B.

**Figure 6-12:** Comparison of the stress spectrum calculation between the Developed Model and GH Bladed for the horizontal brace. Point A is shown in (a) and Point B in (b).

## 6-5-4 Discussion

The level of inaccuracy of the results produced by the DM with respect to GH Bladed can be also understood from Table 6-4, which shows a comparison of the total lifetime fatigue damage values for the examined members. It is clear that the DM highly overestimates the resulting damage on the diagonal member and on the in-plane point of the horizontal brace, but it underestimates the damage for the leg and the out-of-plane point of the horizontal member. One possible explanation with respect to the former case, already stressed in the previous sections, is that the local deformation effects present in the modeshapes as computed by the DM probably result in higher stresses in those members. However, for the latter case more effort is required in order to understand the origin of the deviations on the calculations as presented above and identify possible errors regarding the stress spectrum computation from the DM.

**Table 6-4:** Comparison of the total lifetime fatigue damage values for all examined members of the DM with respect to GH Bladed.

| | **Horizontal** | | **Leg** | | **Diagonal** | |
|---|---|---|---|---|---|---|
| | **Point A** | **Point B** | **Point A** | **Point B** | **Point A** | **Point B** |
| **GH Bladed** | 0.0096 | 0.1184 | 0.1789 | 0.5254 | 0.0098 | 0.0338 |
| **DM** | 0.0198 | 0.0106 | 0.0435 | 0.0457 | 0.0162 | 0.0478 |
| **Error [%]** | -104.5 | 91.1 | 75.7 | 91.3 | -64.2 | -41.4 |

The main inaccuracies of the DM that have to be addressed are the origin of the response at the region of 0.1 Hz that is peaked for the diagonal member only in Bladed simulations, but not in the DM and the reason of the computation of narrow peaks by the DM in comparison with GH Bladed that ultimately results in the false estimation of the fatigue damage calculation.

As discussed with respect to the former case, the region of the frequencies where the peak occurs, suggests that it could originate from either the 1P frequency due to aerodynamic imbalance and/or mass imbalances present on the rotor or from the excitation of the wave spectrum loading for this environmental state, although the frequency of 0.1 Hz seems to be quite small for a wave spectrum. By examining the wave load spectrum that corresponds to state 6 and presented in Fig. 6-13 it is understandable, that indeed the wave loading spectrum has its peak value at a frequency of around 0.2 Hz. Furthermore, the frequency that appears to be peaked at 0.1 Hz in almost all of the environmental states as presented in App. D does not also correspond to the 1P loading, since with a closer observation of Fig. 6-8 and by referring also to Table 6-1, it can be noticed that for the specific wind speed the 1P should be a frequency of around $0.19Hz$.

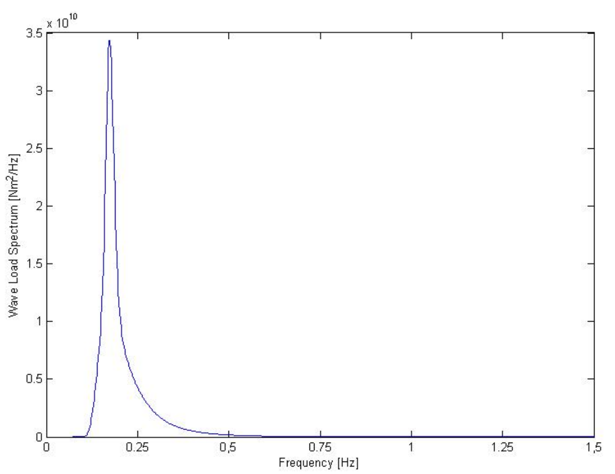


**Figure 6-13:** Wave load spectrum for environmental state 6 with its peak value appearing around 0.2 Hz.

In an effort to further investigate the origin of this peaked frequency, one more comparison with respect to the input loadings between the two models is made. In Figure 6-14 the power spectral densities of the wind loading as calculated and used for the lifetime fatigue assessment by GH Bladed and the input loading spectra used from the DM for the environmental state 6 are examined. The latter spectra have resulted through an FFT application on the timeseries of the thrust force and torque exerted on the turbine without including the tower modes as described in Sec. 4-2. Effectively, both inputs have been calculated with GH Bladed with the only difference being the negligence of the support structure modes.

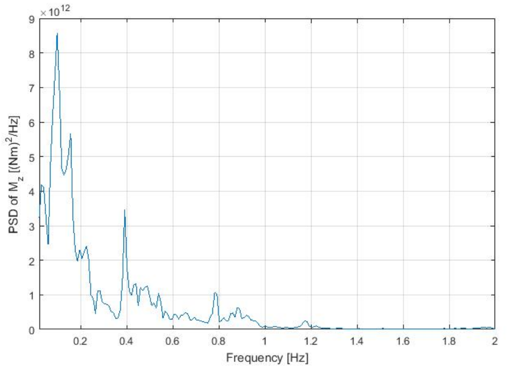


**(a)** PSD of Mz (GH Bladed)

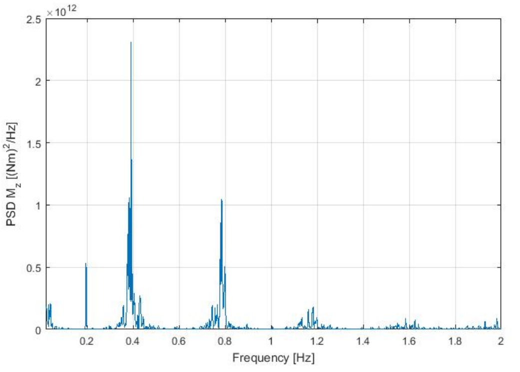


**(b)** PSD of Mz (DM)

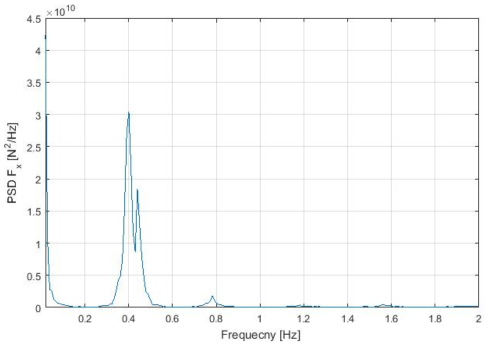


**(c)** PSD of Fx (GH Bladed)

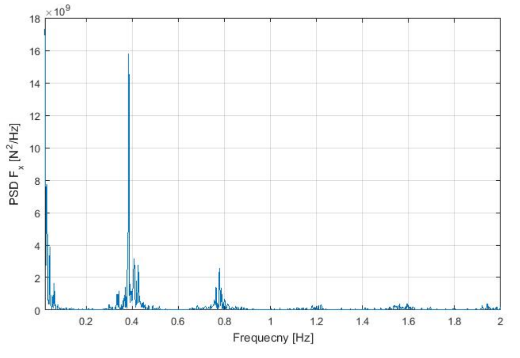


**(d)** PSD of Fx (DM)

**Figure 6-14:** Comparison of wind load spectra as calculated by GH Bladed for the lifetime fatigue assessment (figures placed on the left) and the input load spectra as used by the DM (figures placed on the right) for environmental state 6.

It can be noticed from Figure 6-14 that the spectra for the thrust force used by the two models compare good and the same peaks are identified as expected at the same frequencies with the same magnitude. The only difference is that the GH Bladed spectra have a wider peak and this is caused probably by the fact that they have not been averaged with other seeds. However, for the torque it is visible that at the region of $0.1Hz$ for the GH Bladed case (Fig. 6-14a), there exists a peak that resembles the peak identified at the output spectrum in Figure 6-8 and is not recognisable for the case of the spectrum used for the DM. A probable explanation of this difference could be the presence of a mass imbalance that leads to side-to-side vibrations on the tower, which is not possible to exist for the case where the tower modes are not incorporated, since there is no movement coming from the support structure. Another probable justification could be that the controller of the turbine might have created this behaviour, since the turbine model has a dynamic yaw control system regulated through individual pitch of the blades. This means that in the case of the flexible tower, the structure might have introduced some movement on the turbine and the controller acted in an effort of minimizing the yaw error. Understandably, this cannot be the case for the stiff structure model. Hence, this realization could lead to the conclusion that the methodology followed for the wind load spectrum calculation might not be so accurate for this type of structure or when the torque is also taken into consideration.

As far as the second identified false estimation of the DM is concerned, which refers to the very narrow peaks appearing at the leg causing the erroneous estimation of the fatigue damage values, there are two things that need to be examined; the input load spectrum and the TRF for the leg as calculated by the DM. As observed from Figures 6-15a and 6-15b both graphs appear to have sharp peaks on the region of the frequency of 0.4 Hz. However, the TRF as calculated for point A of the leg seems to have a very narrow peak at around 0.50 Hz (close to the first and second natural frequencies of the structure), which is where the narrow peak of the output stress spectrum appears in Fig. 6-10a. Hence, it is suggested that more attention should be paid on the TRF estimation form the DM for the legs of the structure.

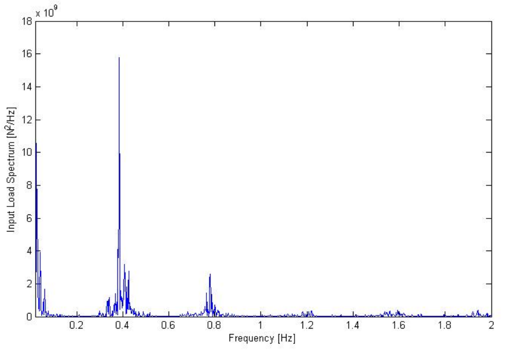


**(a)** Input wind load spectrum for environmental state 6.

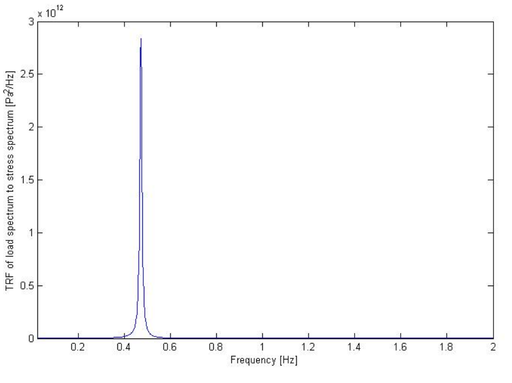


**(b)** TRF of input load spectrum (white noise) to stress spectrum for point A of the leg under investigation.

**Figure 6-15:** Input wind load spectrum for state 6 and TRF of input spectrum to stress spectrum for the leg.

Furthermore, one can not falsely observe that the resulting output stress spectrum of Fig. 6-10 should have a higher order of magnitude with respect to the presented wind load input spectrum and the transfer function. However, it should not be forgotten that the adopted methodology utilizes the modal spectra, which effectively means that the presented graphs are the summation of all the modal wind input load spectra and the summation of all the modal transfer functions. Nevertheless, while calculating the modal output stress spectrum, each modal input load is multiplied with the square of the respective modal TRF that when added together they result in Figure 6-10.

An important reminder here is that the correlation of the wave forces applied at the nodes of the legs have been neglected. If this correlation had also been taken into account, then probably the fatigue damage values as calculated by the DM could have been greater and the wave loading impact might have been more significant as well.

Finally, and now examining from the point of view of Bladed simulations, there is another reason identified that could have led into the augmentation of the error presented between the two frameworks. That is the fact that only one seed for wind and wave loading was used per environmental state, where in contrast the standards suggest at least a number of six seeds per examined state. By using only one seed there was no averaging of the input loading in the time domain simulations, which might have led to the over/under-estimation of the damage caused.

# Chapter 7

# Conclusions

Following the detailed analysis of the different stages of the developed model as well as the evaluation of its performance through the case study, it is of significance here to extract and present some important conclusions that can be helpful for the reader and the potential user of the tool. In addition, some recommendations for future improvement of the DM will be suggested.

## 7-1 Conclusions

The primary aim of this study has been the development of a simplified tool with the ability of dynamic analysis of offshore wind turbine full height lattice structures and the fatigue damage assessment of its members under wind and wave loading. Furthermore, another principal target is time efficiency, which has been achieved by deploying the model in the frequency domain. In the concept of a simplified tool development, several assumptions have been made and have been plainly reported throughout this thesis. In addition, methodologies adopted from the oil & gas industry as well as algorithms initially targeted for fatigue assessment of monopiles have been integrated in the DM with the necessary adaptations.

Regarding the structural model and the representation of it from the tool, it has been presented that the DM has the ability of assessing different structural topologies of lattice structures, giving in this way the opportunity to the user for the investigation of optimal designs for specific applications. The employment of the Euler-Bernoulli beam for the inquiry of the natural frequencies and the modeshapes is successful, since the resulting error between the DM and ANSYS is around 5% for the reference structure and less than 4% for the case study structure for the two first natural frequencies and even lower for the higher modes. However, the calculation of the torsional natural frequency has a big variation with respect to the type of structure used and produces a greater error. Through a sensitivity analysis it has been also identified that the model is quite susceptible to the calculation of the torsional natural frequency. Hence, it can be concluded that although the Euler-Bernoulli beam has been found to be more appropriate due to its simplicity, the adoption of the Timoshenko beam would have been more accurate, since it does not neglect the shear deformations as the former one does. With respect to the modeshape estimation, the DM seems to produce similar results with ANSYS, apart from some local deformations present at the lower members of the structure. It has been identified that these deformations are sensitive to the mesh density and can potentially not be present in the modeshapes with the utilization of a very fine mesh.

Regarding the environmental loading representation and the power spectral densities calculation, established methodologies have been followed. However, it has been shown that the methodology proposed by van der Tempel for the calculation of the TRF for wind load spectrum to stress spectrum might not be applicable in the case where a full height lattice structure is examined or when the torque is also included in the tower top load. This conclusion is derived after the inability of the procedure to facilitate in the input spectrum, loading that might originate from the movement of the structure.

Following the argumentation of the above two paragraphs, it can be concluded that the methodologies initially developed for the oil & gas industry or for monopile structures can be adopted for the estimation of the dynamic behaviour of full height lattice structures for wind turbine applications with satisfactory accuracy. Nonetheless, for the calculation of the wind input load the approach followed might be helpful to be reconsidered.

With respect to the computation of the stress spectrum and ultimately of the fatigue damage, an appropriate transfer function between load spectrum to stress spectrum has been established and it has been proven to be a very demanding task. The level of preciseness of the DM is considered sufficient for cases where there is low to medium environmental loading and limited for the cases of high loading, as it has been shown from the comparison performed between GH Bladed and the DM for the case study. In the provided discussion of Chapter 6, it has been shown that the main origin of the inaccuracies between the two models, is the TRF computation from the DM, which seems to calculate correctly the resonant frequencies of the members of the structure but the peaks are very narrow, resulting to false damage values estimation. Nevertheless, the DM points in the right direction, but there is still a lot of room for improvement.

Ultimately it can be concluded that the DM is certainly advantageous in comparison with a time domain simulation software, since the total required time for a lifetime fatigue assessment ranges from half an hour to maximum three hours, depending on the structure and the mesh density used. In contrast, the equivalent required time for a TD software could range from one to several days. Undoubtedly, the TD framework should be the principal option for concrete and accurate studies, but as it has been presented a FD model can highly assist on the preliminary design phase of a structure.

## 7-2 Recommendations for Future Work

After the presentation of the conclusions, in this section some recommendations for future work on the developed model are proposed. The implementation of the suggestions provided below would be advantageous for increasing the reliability of the model and making it a powerful tool that could assist a future user. Hence, the proposed improvements are:

- An implementation of the Timoshenko beam instead of the Euler-Bernoulli beam, would be beneficial for the accuracy of the model with respect to natural frequency as well as to stress spectrum calculation, since the former takes into account the shear deformation effects and in this is sense it will be more realistic.
- Integration in the model of the effect of interacting modes. Although it was presented that their influence is not so great on the computation of the transfer function, their impact might be a solution of the narrow peaks for the stress spectrum derivation as it was discussed in Sec. 6-5-4.
- The adaptation of a more precise model for the aerodynamic damping calculation (e.g. Garrad method) would improve the accuracy of the tool and it would make it more universal to different wind turbine designs. This improvement is considered significant, since the effect of the aerodynamic damping has been clearly understood in Sec. 5-2-1.
- The calculation of the correlation of the wave forces applied at discrete points. This will enhance the accuracy of the model with respect to wave load calculation.
- The ability of the model to assess all (or some of the most critical) members of the structure, instead of one within a single run of the model, would be an improvement that could offer a better review of the analysis of the structure to the engineer.
- The integration of an optimization procedure would fulfil the ultimate goal of this model. However, it is suggested that this process should be included after the incorporation of the above mentioned improvements of the model, so that the accuracy of it will be increased.

Finally, some improvements of the modelling procedures followed within the context of this report, such as the implementation of a more accurate and site specific foundation model and the wind and wave misalignment along with the above proposed suggestions, could have the possibility to make the developed tool useful and trustworthy for designing purposes of full height lattice structures. Conclusively, it is considered that the developed model has achieved sufficient results with a strong indication that by adapting the above necessary proposals for increasing accuracy could be indeed an alternative scheme for preliminary design of lattice structures.

# Appendix A

# 3-D Euler-Bernoulli Beam Properties

## A-1 Stiffness and Mass Matrices

**Table A-1:** Stiffness matrix of a 3D Euler-Bernoulli beam in local coordinates

$$
k_{el} = \begin{bmatrix}
\frac{EA}{L} & 0 & 0 & 0 & 0 & 0 & -\frac{EA}{L} & 0 & 0 & 0 & 0 & 0 \\
 & \frac{12EI_z}{L^3} & 0 & 0 & 0 & \frac{6EI_z}{L^2} & 0 & -\frac{12EI_z}{L^3} & 0 & 0 & 0 & \frac{6EI_z}{L^2} \\
 & & \frac{12EI_y}{L^3} & 0 & -\frac{6EI_y}{L^2} & 0 & 0 & 0 & -12\frac{EI_y}{L^3} & 0 & -\frac{6EI_y}{L^2} & 0 \\
 & & & \frac{GJ}{L} & 0 & 0 & 0 & 0 & 0 & -\frac{GJ}{L} & 0 & 0 \\
 & & & & \frac{4EI_y}{L} & 0 & 0 & 0 & \frac{6EI_y}{L^2} & 0 & \frac{2EI_y}{L} & 0 \\
 & & & & & \frac{4EI_z}{L} & 0 & -\frac{6EI_z}{L^2} & 0 & 0 & 0 & \frac{2EI_z}{L} \\
 & & & & & & \frac{EA}{L} & 0 & 0 & 0 & 0 & 0 \\
 & & & & & & & \frac{12EI_z}{L^3} & 0 & 0 & 0 & -\frac{6EI_z}{L^2} \\
 & & & & & & & & \frac{12EI_y}{L^3} & 0 & \frac{6EI_y}{L^2} & 0 \\
 & & & & & & & & & \frac{GJ}{L} & 0 & 0 \\
 & & & & & & & & & & \frac{4EI_y}{L} & 0 \\
\text{Sym.} & & & & & & & & & & & \frac{4EI_z}{L}
\end{bmatrix}
$$

**Table A-2:** Mass matrix for a 3D Euler-Bernoulli beam in local coordinates.

$$
m_{el} = \rho AL \begin{bmatrix}
\frac{1}{3} & & & & & & & & & & & \text{Sym.} \\
0 & \frac{13}{35}+\frac{6I}{5AL^2} & & & & & & & & & & \\
0 & 0 & \frac{13}{35}+\frac{6I}{5AL^2} & & & & & & & & & \\
0 & 0 & 0 & \frac{J}{3A} & & & & & & & & \\
0 & 0 & -\frac{11L}{210}-\frac{I}{10AL} & 0 & \frac{L^2}{105}+\frac{2I}{15A} & & & & & & & \\
0 & \frac{11L}{210}+\frac{I}{10AL} & 0 & 0 & 0 & \frac{L^2}{105}+\frac{2I}{15A} & & & & & & \\
\frac{1}{6} & 0 & 0 & 0 & 0 & 0 & \frac{1}{3} & & & & & \\
0 & \frac{9}{70}-\frac{6I}{5AL^2} & 0 & 0 & 0 & \frac{13L}{420}-\frac{I}{10AL} & 0 & \frac{13}{35}+\frac{6I}{5AL^2} & & & & \\
0 & 0 & \frac{9}{70}-\frac{6I}{5AL^2} & 0 & -\frac{13L}{420}+\frac{I}{10AL} & 0 & 0 & 0 & \frac{13}{35}+\frac{6I}{5AL^2} & & & \\
0 & 0 & \frac{J}{6A} & 0 & 0 & 0 & 0 & 0 & 0 & \frac{J}{3A} & & \\
0 & 0 & \frac{13L}{420}-\frac{I}{10AL} & 0 & -\frac{L^2}{140}-\frac{I}{30A} & 0 & 0 & 0 & \frac{11L}{210}+\frac{I}{10AL} & 0 & \frac{L^2}{105}+\frac{2I}{15A} & \\
0 & -\frac{13L}{420}+\frac{I}{10AL} & 0 & 0 & 0 & -\frac{L^2}{140}-\frac{I}{30A} & 0 & -\frac{11L}{210}-\frac{I}{10AL} & 0 & 0 & 0 & \frac{L^2}{105}+\frac{2I}{15A}
\end{bmatrix}
$$

## A-2 Shape Function Equations

The shape functions for a 3D beam element can be found by the following equations:

$$
\begin{aligned}
N_1 &= -\frac{1}{L}(x - x_j) \\
N_2 &= -\frac{1}{L}(x - x_i) \\
N_3 &= 1 - \frac{3x^2}{L^2} + \frac{2x^3}{L^3} \\
N_4 &= x(-1 + \frac{2x}{L} - \frac{x^2}{L^2}) \\
N_5 &= \frac{x^2}{L^2}(3 - 2\frac{x}{L}) \\
N_6 &= \frac{x^2}{L}(1 - \frac{x}{L})
\end{aligned}
\tag{A-1}
$$

# Appendix B

# Mode Shape Comparison Between ANSYS and the DM

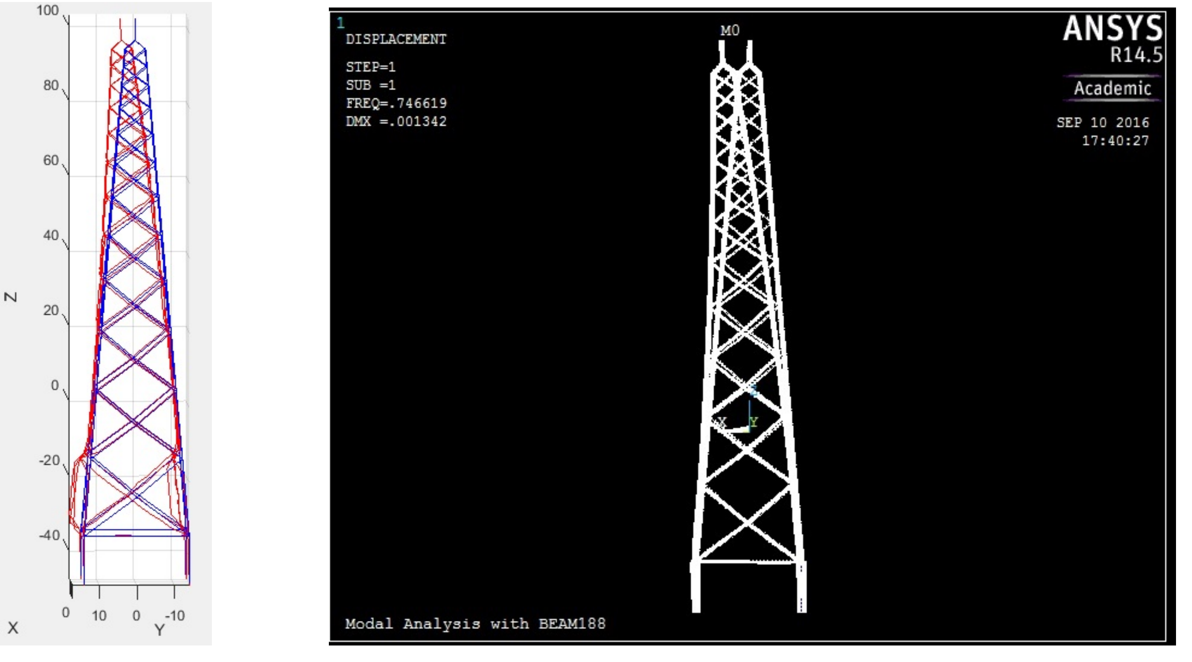


**Figure B-1:** Comparison of the first modeshape (bending about the x-axis) as calculated by the DM (left) and ANSYS (right).

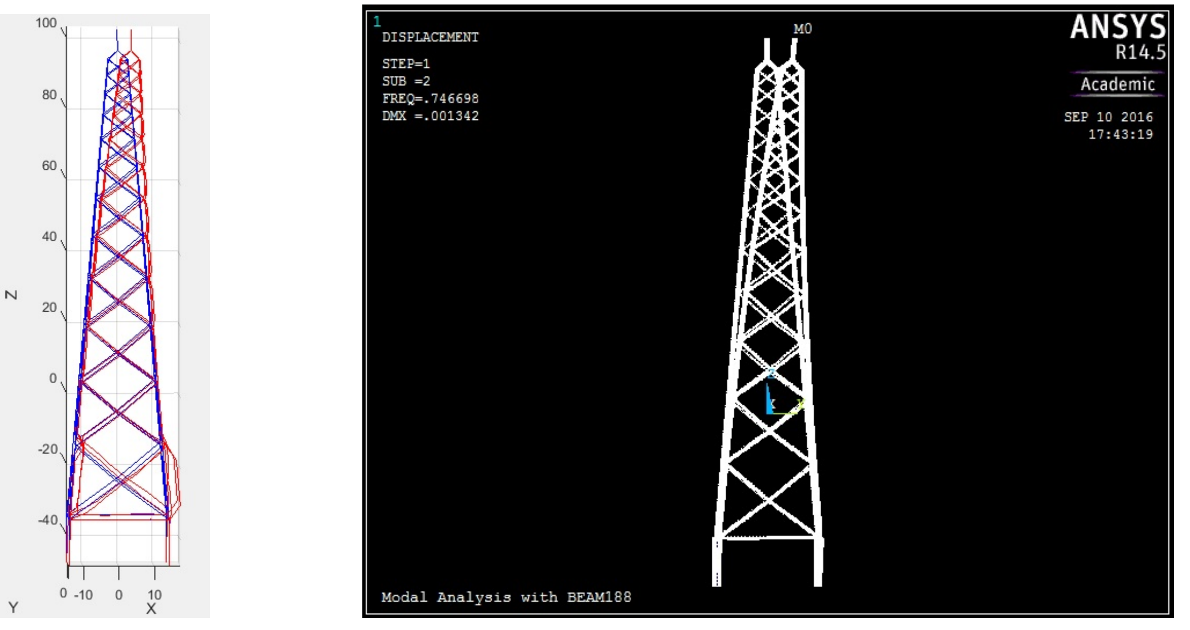


**Figure B-2:** Comparison of the second modeshape (bending about the y-axis) as calculated by the DM (left) and ANSYS (right).

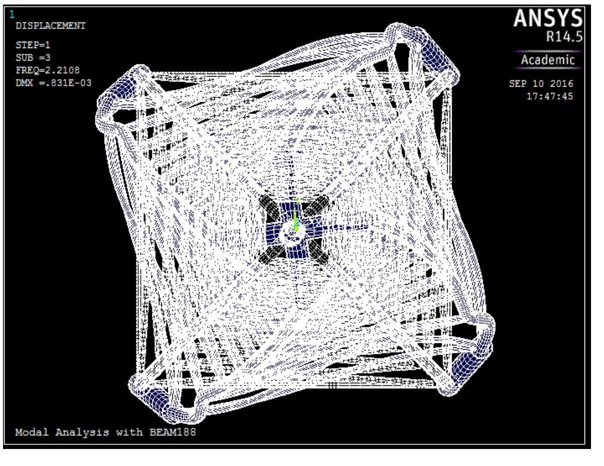


**Figure B-3:** Modeshape of the structure due to torsional natural frequency (Top view). The great influence of the torsional effect is visible.

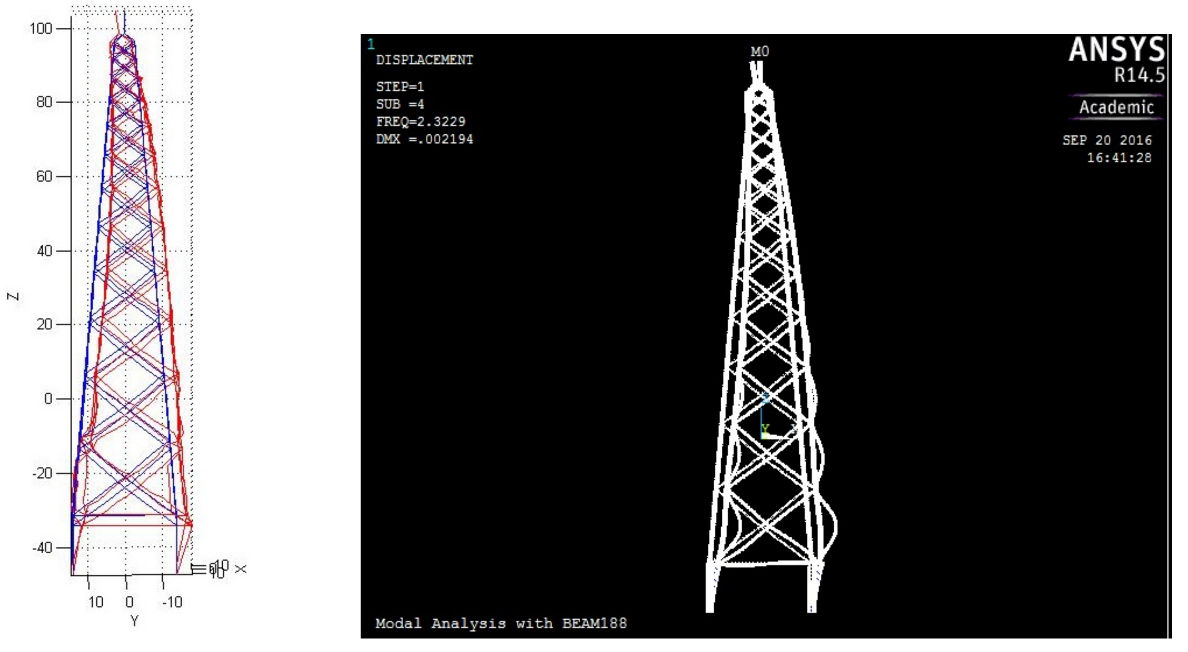


**Figure B-4:** Comparison of the fourth modeshape (bending about the x-axis with local out-of-plane deflection) as calculated by the DM (left) and ANSYS (right).

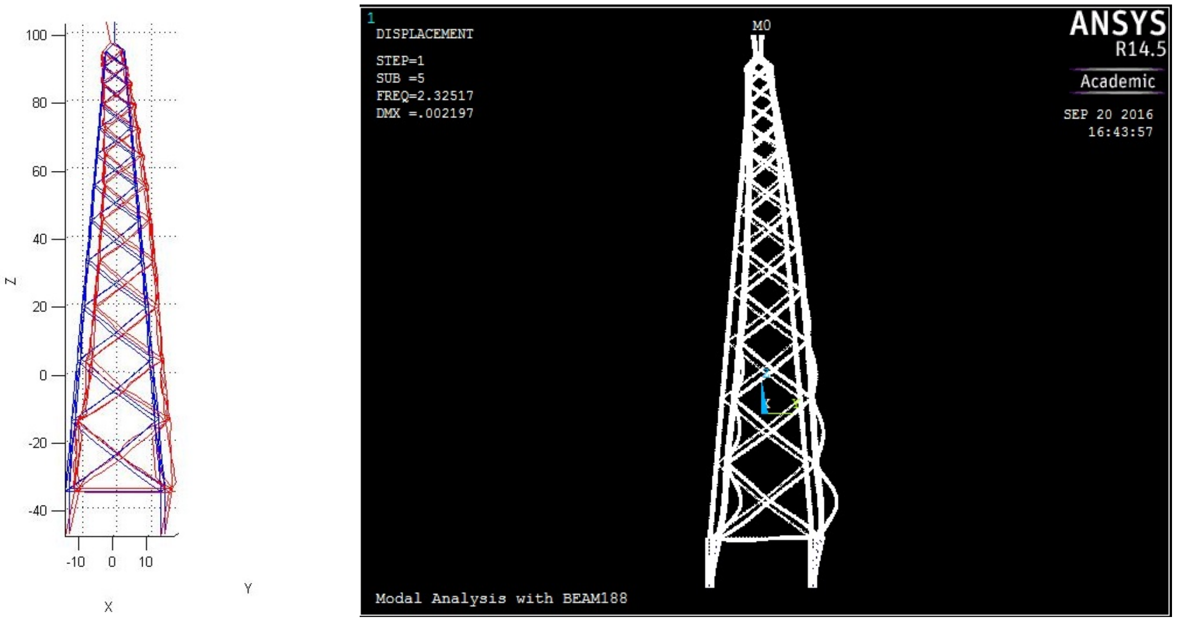


**Figure B-5:** Comparison of the second modeshape (bending about the y-axis with local out-of-plane deflection) as calculated by the DM (left) and ANSYS (right).

# Appendix C

# 3D Scatter Diagram

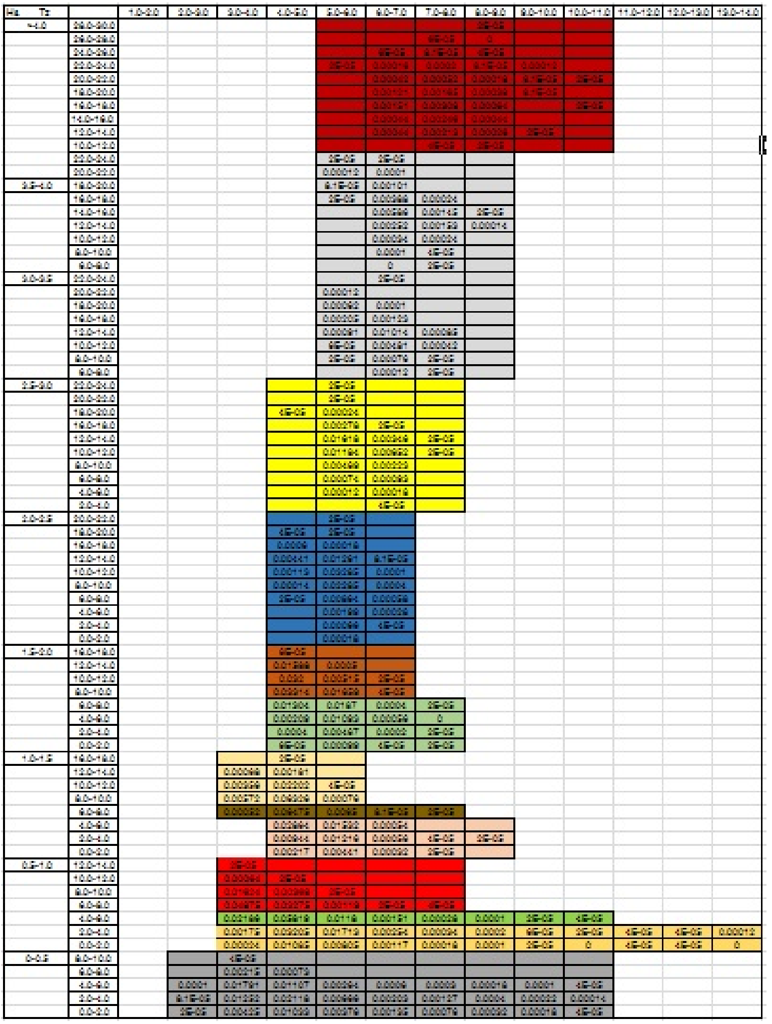

**Figure C-1:** The 3D scatter diagram used for the location of Fi. 6-2 (wind speed, significant wave height and zero crossing period with their respective probabilities).

# Appendix D

# Stress Spectrum and Fatigue Damage Comparison

## D-1 Diagonal

**Table D-1:** Comparison of the resulting contribution to lifetime fatigue damage per state for a diagonal member close to mudline between GH Bladed and the Developed Model.

| | **GH Bladed** | | **DM** | |
|---|---|---|---|---|
| **State** | **A** | **B** | **A** | **B** |
| **1** | 7.85E-06 | 1.37E-05 | 4.44E-05 | 7.74E-05 |
| **2** | 5.63E-06 | 8.45E-06 | 4.19E-05 | 6.78E-05 |
| **3** | 7.16E-06 | 1.66E-05 | 3.10E-05 | 5.16E-05 |
| **4** | 6.35E-05 | 1.96E-04 | 7.51E-05 | 1.35E-04 |
| **5** | 5.27E-05 | 1.71E-04 | 7.09E-05 | 1.27E-04 |
| **6** | 3.11E-04 | 9.61E-04 | 1.56E-04 | 3.50E-04 |
| **7** | 2.64E-04 | 1.18E-03 | 2.44E-04 | 6.58E-04 |
| **8** | 6.35E-04 | 2.25E-03 | 5.15E-04 | 1.31E-03 |
| **9** | 1.73E-03 | 6.37E-03 | 1.92E-03 | 5.76E-03 |
| **10** | 2.24E-03 | 6.02E-03 | 2.08E-03 | 6.53E-03 |
| **11** | 1.10E-03 | 3.46E-03 | 2.78E-03 | 8.38E-03 |
| **12** | 1.43E-03 | 4.58E-03 | 3.60E-03 | 1.08E-02 |
| **13** | 1.99E-03 | 8.60E-03 | 4.57E-03 | 1.35E-02 |

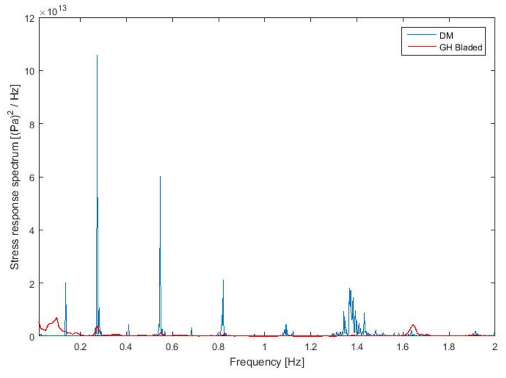


**(a)** Point A.

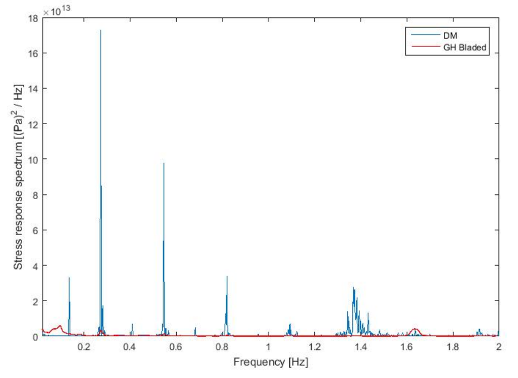


**(b)** Point B.

**Figure D-1:** Environmental State 1.

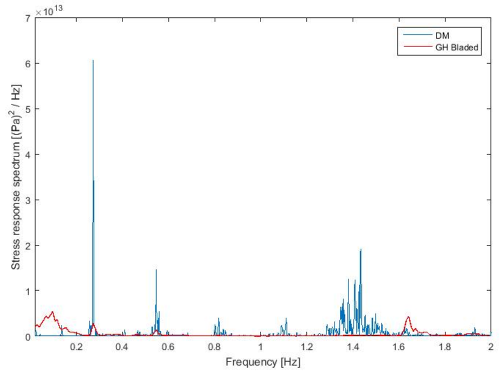


**(a)** Point A.

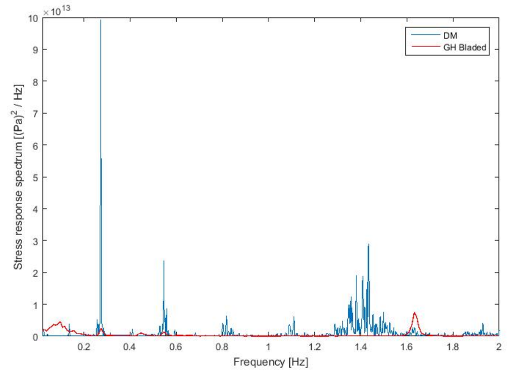


**(b)** Point B.

**Figure D-2:** Environmental State 3.

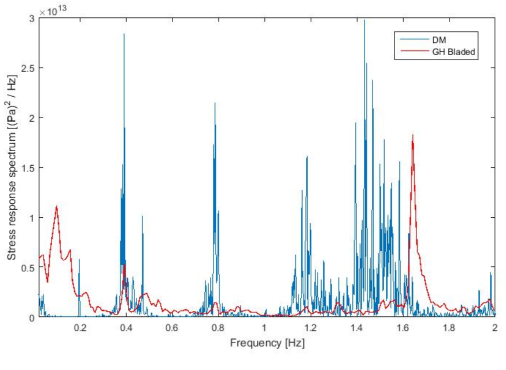


**(a)** Point A.

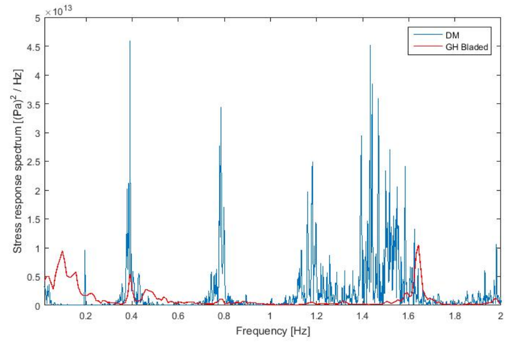


**(b)** Point B.

**Figure D-3:** Environmental State 6.

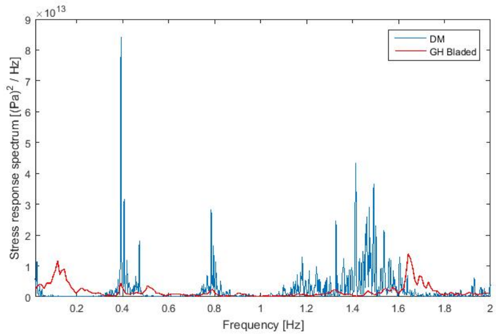


**(a)** Point A.

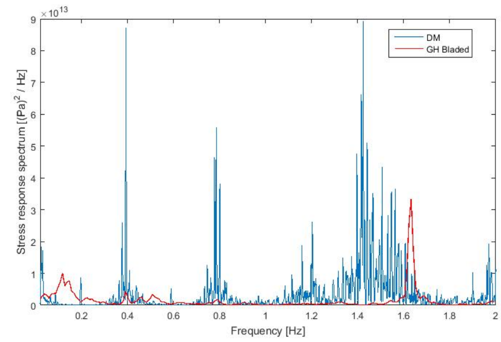


**(b)** Point B.

**Figure D-4:** Environmental State 8.

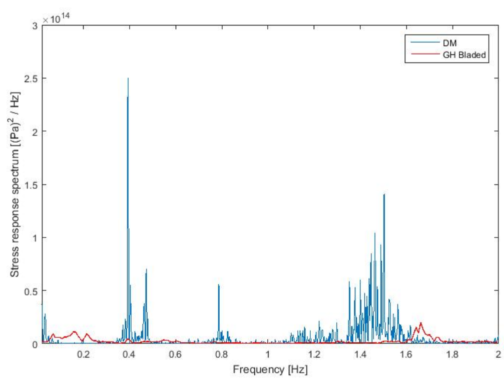


**(a)** Point A.

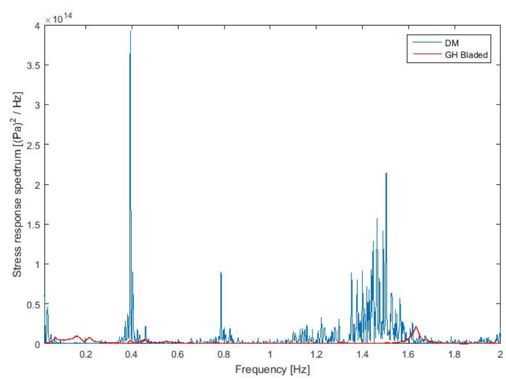


**(b)** Point B.

**Figure D-5:** Environmental State 11.

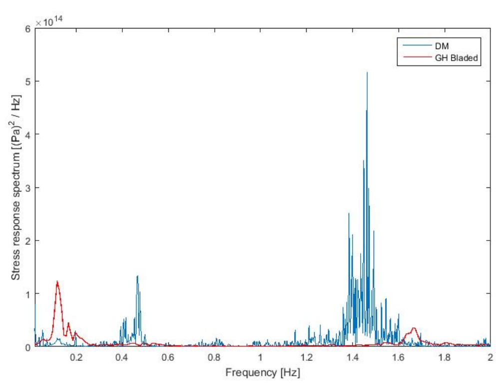


**(a)** Point A.

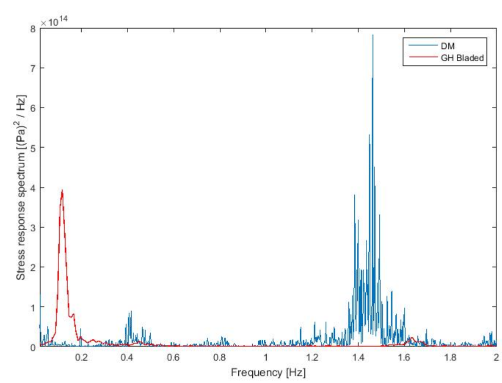


**(b)** Point B.

**Figure D-6:** Environmental State 13.

## D-2 Leg

**Table D-2:** Comparison of the resulting contribution to lifetime fatigue damage per state for the leg close to mudline between GH Bladed and the Developed Model.

| | GH Bladed | | DM | |
|---|---|---|---|---|
| **State** | **A** | **B** | **A** | **B** |
| **1** | 1.28E-04 | 4.21E-04 | 4.03E-05 | 2.88E-05 |
| **2** | 5.40E-05 | 1.94E-04 | 4.15E-05 | 3.34E-05 |
| **3** | 1.10E-04 | 3.98E-04 | 3.38E-05 | 2.86E-05 |
| **4** | 2.34E-03 | 7.57E-03 | 1.74E-04 | 1.80E-04 |
| **5** | 1.87E-03 | 6.04E-03 | 1.64E-04 | 1.70E-04 |
| **6** | 3.05E-03 | 9.46E-03 | 1.18E-03 | 1.38E-03 |
| **7** | 2.59E-03 | 7.76E-03 | 1.58E-03 | 1.71E-03 |
| **8** | 7.13E-03 | 2.18E-02 | 4.29E-03 | 3.64E-03 |
| **9** | 1.94E-02 | 5.91E-02 | 5.98E-03 | 6.85E-03 |
| **10** | 2.70E-02 | 7.10E-02 | 3.38E-03 | 3.71E-03 |
| **11** | 2.61E-02 | 7.41E-02 | 7.04E-03 | 8.18E-03 |
| **12** | 3.39E-02 | 9.66E-02 | 9.20E-03 | 1.06E-02 |
| **13** | 5.51E-02 | 1.71E-01 | 1.04E-02 | 9.20E-03 |

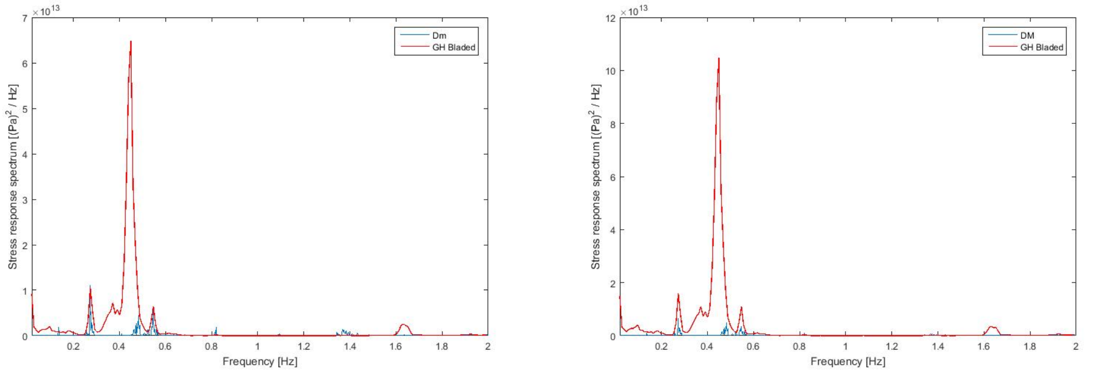


**(a)** Point A. **(b)** Point B.

**Figure D-7:** Environmental State 1.

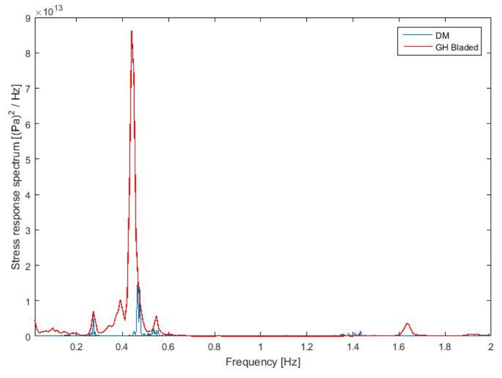


**(a)** Point A.

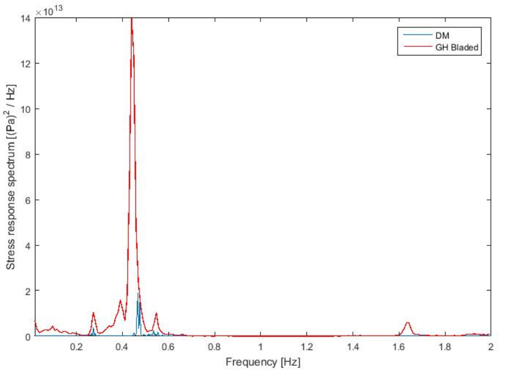


**(b)** Point B.

**Figure D-8:** Environmental State 3.

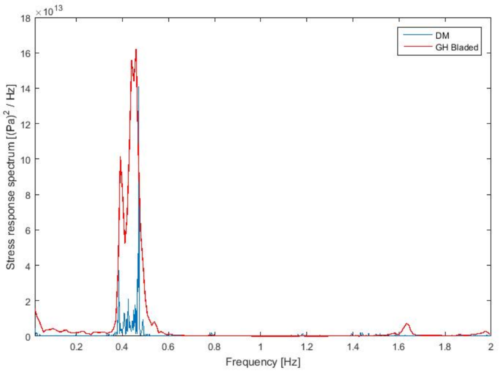


**(a)** Point A.

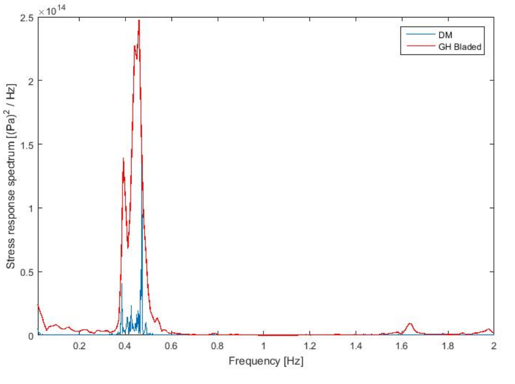


**(b)** Point B.

**Figure D-9:** Environmental State 6.

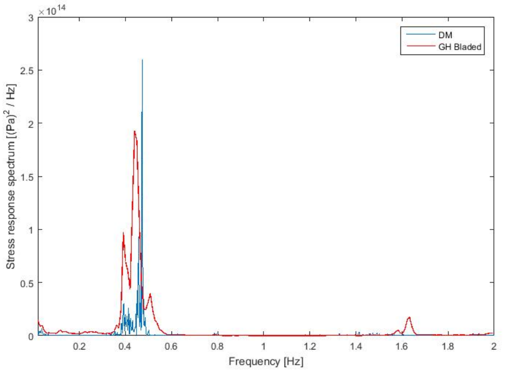


**(a)** Point A.

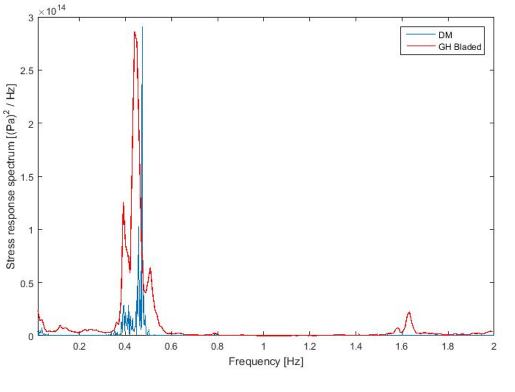


**(b)** Point B.

**Figure D-10:** Environmental State 8.

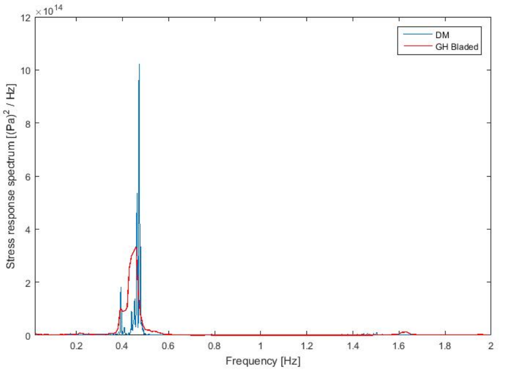


**(a)** Point A.

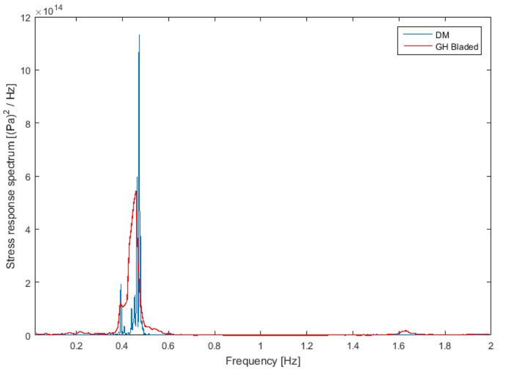


**(b)** Point B.

**Figure D-11:** Environmental State 11.

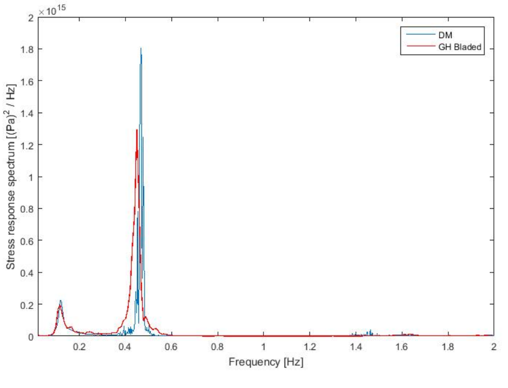


**(a)** Point A.

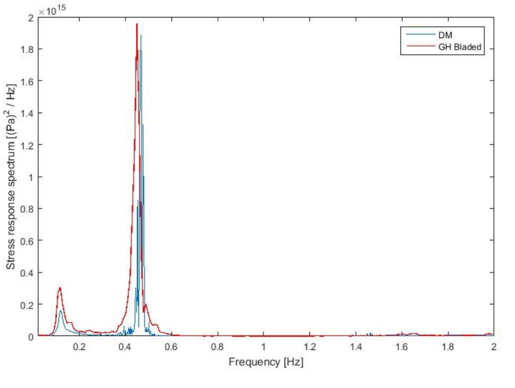


**(b)** Point B.

**Figure D-12:** Environmental State 13.

## D-3 Horizontal

**Table D-3:** Comparison of the resulting contribution to lifetime fatigue damage per state for the horizontal member at mudline between GH Bladed and the Developed Model.

| | GH Bladed | | DM | |
|---|---|---|---|---|
| **State** | **A** | **B** | **A** | **B** |
| **1** | 2.19E-06 | 9.77E-06 | 4.97E-05 | 4.12E-05 |
| **2** | 1.40E-06 | 7.51E-06 | 4.92E-05 | 3.90E-05 |
| **3** | 1.91E-06 | 1.82E-05 | 3.67E-05 | 3.00E-05 |
| **4** | 4.05E-05 | 4.52E-04 | 1.34E-04 | 8.81E-05 |
| **5** | 3.13E-05 | 3.42E-04 | 1.26E-04 | 8.32E-05 |
| **6** | 2.01E-04 | 2.07E-03 | 5.55E-04 | 3.38E-04 |
| **7** | 2.33E-04 | 3.24E-03 | 6.20E-04 | 3.52E-04 |
| **8** | 4.96E-04 | 6.76E-03 | 1.66E-03 | 1.00E-03 |
| **9** | 1.42E-03 | 2.29E-02 | 2.97E-03 | 1.63E-03 |
| **10** | 2.84E-03 | 2.99E-02 | 1.87E-03 | 9.35E-04 |
| **11** | 1.27E-03 | 1.48E-02 | 3.73E-03 | 2.02E-03 |
| **12** | 1.65E-03 | 1.91E-02 | 4.82E-03 | 2.62E-03 |
| **13** | 1.50E-03 | 1.89E-02 | 3.20E-03 | 1.47E-03 |

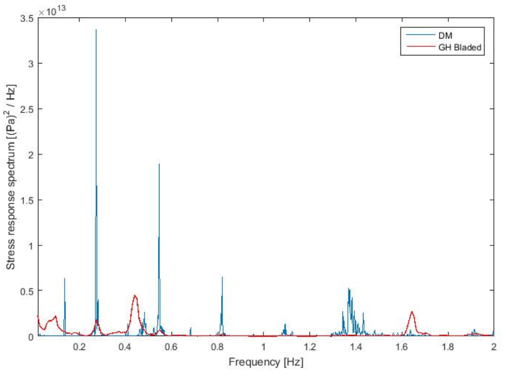


**(a)** Point A.

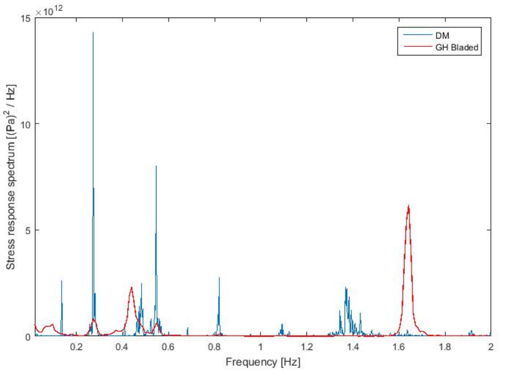


**(b)** Point B.

**Figure D-13:** Environmental State 1.

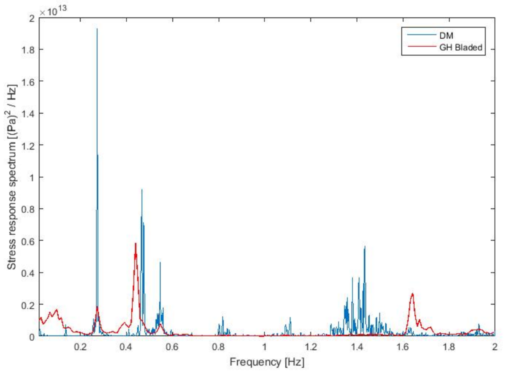


**(a)** Point A.

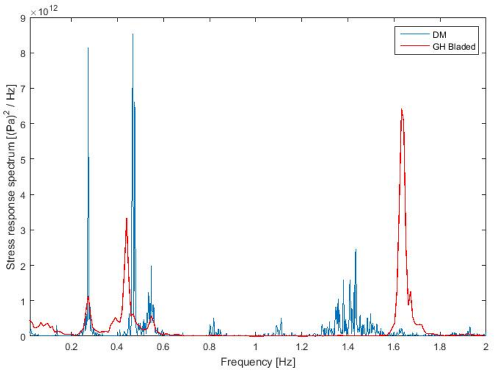


**(b)** Point B.

**Figure D-14:** Environmental State 3.

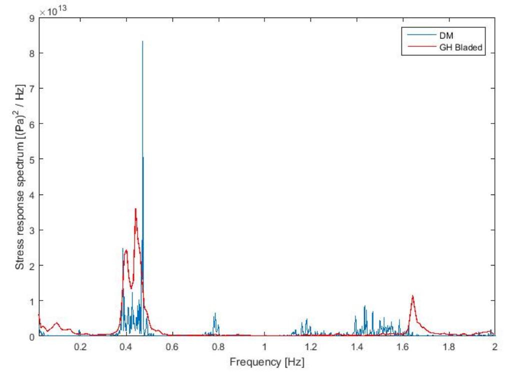


**(a)** Point A.

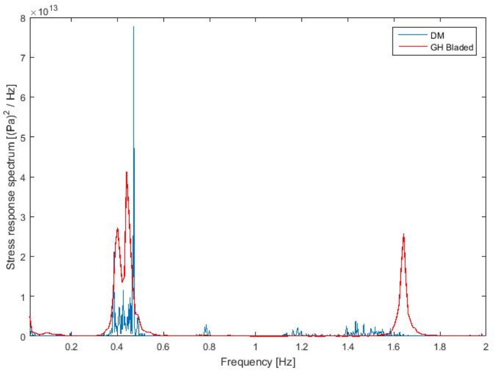


**(b)** Point B.

**Figure D-15:** Environmental State 6.

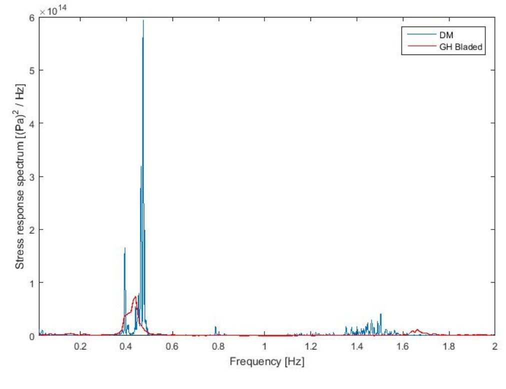


**(a)** Point A.

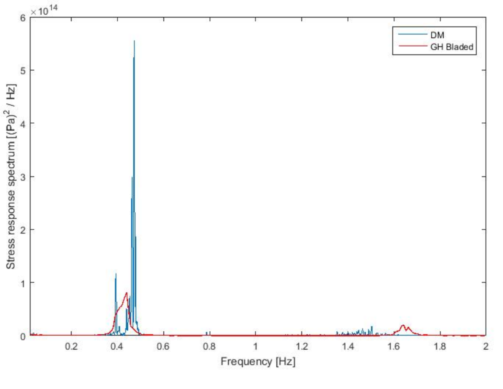


**(b)** Point B.

**Figure D-16:** Environmental State 11.

# Bibliography


[1] 2-B Energy, 2016 (accessed June 3, 2016). [Online]. Available: http://2benergy.com/

[2] N. Alati, V. Nava, and G. Failla, "On the fatigue behavior of support structures for offshore wind turbines," *Wind and Structures*, vol. 18, no. 2, pp. 117–134, 2014.

[3] F. Arena and V. Nava, "On linearization of morison force given by high three-dimensional sea wave groups," *Probabilistic Engineering Mechanics*, vol. 23, no. 2, pp. 104–113, 2008.

[4] D. N. V. AS, "Fatigue design of offshore steel structures," 2012.

[5] N. D. Barltrop and A. J. Adams, *Dynamics of fixed marine structures.* Butterworth-Heinemann, 1977, vol. 91.

[6] N. Bishop, "The use of frequency domain parameters to predict structural fatigue," Ph.D. dissertation, University of Warwick, 1988.

[7] D. I. P. BOERAEVE, "Introduction to the finite element method (fem)," *Institutgramme Liege*, pp. 2–68, 2010.

[8] L. E. Borgman, "The spectral density for ocean wave forces." ASCE, 1965.

[9] H. Bungum, P. Swearingen, and G. Woo, "Earthquake hazard assessment in the north sea," *Physics of the earth and planetary interiors*, vol. 44, no. 3, pp. 201–210, 1986.

[10] T. Camp, M. Morris, R. Van Rooij, J. Van Der Tempel, M. Zaaijer, A. Henderson, K. Argyriadis, S. Schwartz, H. Just, W. Grainger *et al.*, "Design methods for offshore wind turbines at exposed sites," *Final Report of the OWTES Project, Garrad Hassan and Partners Ltd., Bristol, UK*, 2003.

[11] S. K. Chakrabarti, *Hydrodynamics of offshore structures.* WIT press, 1987.

[12] A. K. Chopra *et al.*, *Dynamics of structures.* Prentice Hall New Jersey, 1995, vol. 3.

[13] I. Chowdhury and S. P. Dasgupta, "Computation of rayleigh damping coefficients for large systems," *The Electronic Journal of Geotechnical Engineering*, vol. 8, no. 0, 2003.

[14] R. W. Clough and J. Penzien, "Dynamics of structures," Tech. Rep., 1975.

[15] I. E. Commission *et al.*, "Iec 61400-1: Wind turbines part 1: Design requirements," *International Electrotechnical Commission*, 2005.

[16] R. D. Cook *et al.*, *Concepts and applications of finite element analysis.* John Wiley & Sons, 2007.

[17] W. De Vries, N. K. Vemula, P. Passon, T. Fischer, D. Kaufer, D. Matha, B. Schmidt, and F. Vorpahl, "Final report wp 4.2: Support structure concepts for deep water sites: Deliverable d4. 2.8 (wp4: offshore foundations and support structures)," Upwind, Tech. Rep., 2011.

[18] M. Ebert, "Some aspects of the analysis of offshore structures," Ph.D. dissertation, University of Southampton, 1977.

[19] European Wind Energy Association (EWEA), "Deep water - the next step for offshore wind energy," Tech. Rep., July 2013.

[20] A. J. Ferreira, *MATLAB codes for finite element analysis: solids and structures.* Springer Science & Business Media, 2008, vol. 157.

[21] Gencturk, B., Attar, A., Tort, C., "Optimal design of lattice wind turbine towers," $15^{th}$ *World Conference on Earthquake Engineering (WCEE), Lisboa, Portugal*, 2012.

[22] A. Halfpenny, "A frequency domain approach for fatigue life estimation from finite element analysis," in *Key Engineering Materials*, vol. 167. Trans Tech Publ, 1999, pp. 401–410.

[23] O. E. Hansteen and K. Bell, "On the accuracy of mode superposition analysis in structural dynamics," *Earthquake Engineering & Structural Dynamics*, vol. 7, no. 5, pp. 405–411, 1979.

[24] A. R. Henderson, C. Morgan, B. Smith, H. C. Sørensen, R. J. Barthelmie, and B. Boesmans, "Offshore wind energy in europe-a review of the state-of-the-art," *Wind energy*, vol. 6, no. 1, pp. 35–52, 2003.

[25] J. M. Jonkman, S. Butterfield, W. Musial, and G. Scott, "Definition of a 5-mw reference wind turbine for offshore system development," 2009.

[26] M. Kühn, T. Cockerill, L. Harland, R. Harrison, C. Schöntag, G. van Bussel, and J. Vugts, "Opti-owecs final report vol. 2: Methods assisting the design of offshore wind energy conversion systems," *Delft University of Technology: Delft*, 1998.

[27] M. J. Kühn, *Dynamics and design optimisation of offshore wind energy conversion systems.* TU Delft, Delft University of Technology, 2001.

[28] D. Logan, *A first course in the finite element method.* Cengage Learning, 2011.

[29] H. Long and G. Moe, "Preliminary design of bottom-fixed lattice offshore wind turbine towers in the fatigue limit state by the frequency domain method," *Journal of Offshore Mechanics and Arctic Engineering*, vol. 134, no. 3, p. 031902, 2012.

[30] H. Long, G. Moe, and T. Fischer, "Lattice towers for bottom-fixed offshore wind turbines in the ultimate limit state: variation of some geometric parameters," *Journal of Offshore Mechanics and Arctic Engineering*, vol. 134, no. 2, p. 021202, 2012.

[31] M. López Aenlle, R. Brincker, and A. C. Fernández Canteli, "Some methods to determine scaled mode shapes in natural input modal analysis," 2005.

[32] E.-M. Lourens, "Mutli-member structures," 2015, tU Delft, University lecture.

[33] M. K. Madugula, *Dynamic response of lattice towers and guyed masts.* ASCE Publications, 2001.

[34] J. Manwell, J. G. McGowan, and A. L. Rogers, *Wind energy explained: theory, design and application.* John Wiley & Sons, 2010.

[35] M. Muskulus, "The full-height lattice tower concept," *Energy Procedia*, vol. 24, pp. 371–377, 2012.

[36] Norwegian University of Science and Technology, 2016 (accessed June 3, 2016). [Online]. Available: https://www.ntnu.edu/

[37] A. Preumont, *Random Vibration and Spectral Analysis/Vibrations aléatoires et analyse spectral.* Springer Science & Business Media, 2013, vol. 33.

[38] Preumont A., *Twelve lectures on structural dynamics.* Springer, 2013.

[39] J. S. Przemieniecki, "Matrix structural analysis of substructures," *AIAA Journal*, vol. 1, no. 1, pp. 138–147, 1963.

[40] D. Reddy and A. Swamidas, *Essentials of offshore structures: framed and gravity platforms.* CRC press, 2013.

[41] D. Salzmann and J. Van der Tempel, "Aerodynamic damping in the design of support structures for offshore wind turbines," in *Paper of the Copenhagen offshore conference.* Citeseer, 2005.

[42] M. Seidel, "Wave induced fatigue loads," *Stahlbau*, vol. 83, no. 8, pp. 535–541, 2014.

[43] P. Sørensen, *Frequency domain modelling of wind turbine structures*, 1994.

[44] J. W. Staerdahl, "Beam elements in 3d," 2014, aalborg university, university lecture.

[45] X. Sun, D. Huang, and G. Wu, "The current state of offshore wind energy technology development," *Energy*, vol. 41, no. 1, pp. 298–312, 2012.

[46] B. Teng and Y.-C. Li, "The linearization of drag force and the error estimation of linear force spectrum," *Coastal Engineering*, vol. 14, no. 2, pp. 173–183, 1990.

[47] J. Van der Tempel, *Design of support structures for offshore wind turbines.* TU Delft, Delft University of Technology, 2006.

[48] D.-D. N. Veritas, "Dnv-os-j101 offshore standard," *Design of Offshore Wind Turbine Structures*, 2014.

[49] F. Vorpahl, W. Popko, and D. Kaufer, "Description of a basic model of the "upwind reference jacket" for code comparison in the oc4 project under iea wind annex 30," 2011.

[50] J. Vughts, R. Kinra *et al.*, "Probabilistic fatigue analysis of fixed offshore structures," in *Offshore Technology Conference*. Offshore Technology Conference, 1976.

[51] J. H. Vugts, *Handbook of bottom founded offshore structures*. Eburon, 2013.

[52] P. H. Wirsching, "Fatigue reliability for offshore structures," *Journal of Structural Engineering*, 1984.

[53] Y. Xu, Q. Li, D. Wu, and Z. Chen, "Stress and acceleration analysis of coupled vehicle and long-span bridge systems using the mode superposition method," *Engineering Structures*, vol. 32, no. 5, pp. 1356–1368, 2010.

[54] M. Zaaijer, "Foundation modelling to assess dynamic behaviour of offshore wind turbines," *Applied Ocean Research*, vol. 28, no. 1, pp. 45–57, 2006.

[55] D. Zwick, M. Muskulus, and G. Moe, "Iterative optimization approach for the design of full-height lattice towers for offshore wind turbines," *Energy Procedia*, vol. 24, pp. 297–304, 2012.